Alleima

DEFORMATION BEHAVIOURS IN ALLOY 718 AND MEDIUM-HIGH ENTROPY ALLOYS

Master Of Science Thesis Department of Industrial and Materials Science

JOHN JOY

Chalmers university of technology

2023

DEFORMATION BEHAVIOURS IN ALLOY 718 AND MEDIUM-HIGH ENTROPY ALLOYS

JOHN JOY

Sandviken June 2023

Master Of Science Thesis

Department Of Industrial and Materials Science

Chalmers University of Technology

Deformation Behaviours in Alloy 718 And Medium-high Entropy Alloys

Supervisor:

Professor Dr. Guocai Chai Group expert Alleima Stragetic research Sandviken, Sweden

Adjunct Professor in Engineering Materials Department of Management and Engineering,

Div. of Engineering Materials Linköping University

Examiner:

Professor Dr. Fang Liu Associate Professor

Department of Industrial and Materials Science Chalmers University of Technology

SE-412 96 Gothenburg, Sweden

Master's Thesis 2023

Department Of Industrial and Materials Science
Chalmers University of Technology SE-412 96 Gothenburg, Sweden

Acknowledgements

First and foremost, I extend my heartfelt thanks to Alleima AB for providing me with an exceptional platform that has been instrumental in the development and execution of this project. The support and resources offered by Alleima AB have been invaluable, and I am truly grateful for their contributions.

I am deeply indebted to Professor Dr. Guocai Chai for his exceptional guidance, training, and the opportunity to work on this project. His expertise, encouragement, and mentorship have played a pivotal role in shaping the outcome of this Endeavor. I am honoured to have had the privilege of working under his supervision. A special thanks to Prof. Fang Liu at Chalmers university of technology for kind support and encouragement.

I would like to extend my appreciation to Dr. Raveendra Siriki, Jerry Lindkvist, and Conny Sand for their dedicated efforts in training and providing invaluable support for the microstructure analysis aspect of this project. Their expertise and guidance have been crucial in understanding and interpreting the intricate details of the materials studied.

Furthermore, I am grateful to Emil Cederberg, Adelin Nzomwita, and Mikael Wijk for their assistance in conducting mechanical testing and heat treatment experiments. Their expertise and collaboration have significantly contributed to the experimental aspects of this project.

I would also like to acknowledge the contributions of Dr. David Molnar and Dr. Patrick Conway, who provided valuable assistance with thermodynamic calculations and modelling. Their expertise and insights have been instrumental in ensuring the accuracy and reliability of our theoretical predictions.

Part -I

Deformation Behaviours in Alloy 718

Abstract

The present study focuses on investigating the intermediate temperature embrittlement (ITE) behaviour of the nickel-based superalloy 718 under various strain rates and heat treatment conditions. Tensile tests were performed at room temperature, 650°C, and 750°C with strain rates ranging from 10^{-1}, 10^{-2}, 10^{-3} & $10^{-4}s^{-1}$. The tensile strength and elongation were compared across different test conditions. Loss of ductility or intermediate temperature embrittlement phenomena were observed at 650°C and 750°C under low strain rates of 10^{-3} & $10^{-4}s^{-1}$ and elongation is improved upon high strain rate. To investigate the underlying mechanisms, advanced microstructural analysis was conducted to identify influence of temperature and strain rate dependent mechanism at grain boundary and matrix. Advanced techniques such as Field Emission Gun Scanning Electron Microscopy with Energy Dispersive Spectroscopy, Electron Backscatter Diffraction, and Electron Channelling Contrast Imaging were employed for detailed microstructure characterization. The results show that the presence of Laves phase, DSA and oxidation assisted intergranular cracks may promote ITE. On the other hand, ITE in Alloy 718 can be avoided with a higher strain rate.

Keywords: Intermediate temperature embrittlement, Nickel based super alloys, IN718, Tensile test, Deformation, precipitation, SEM, EBSD, ECCI, Thermo-calc

Contents

Abbreviation

ST	Solution Treatment
CCT	Cooling curve transformation
TTT	Time Temperature Transformation
γ'	Gamma prime
γ''	Gamma double prime
ITE	Intermediate temperature embrittlement
EBSD	Electron Backscatter Diffraction
ECCI	Electron Channelling Contrast Imaging
SEM	Scanning electron microscopy
RT	Room Temperature
TTT	Time-Temperature-Transformation
LAGB	Low angle grain boundary
HAGB	High angle grain boundary
DSA	Dynamic strain aging

1 INTRODUCTION

1.1 ALLEIMA

Alleima is one of the leading global manufacturers for developing and manufacturing high quality advanced stainless steels, special alloys, and solution for industrial heating products. With over 160 years of experience in material technology field, Alleima has formed close long-term collaboration with customers from various fields energy, chemical, aerospace industry, strip steel for air conditioner, compressor, and knife application across different countries. Alleima believes innovation is to be driving force behind the success for inventing more than 900 alloy recipes, of which 850 recipes are protected by patents. The company has wealth of experience in material technology, metallurgy and industrial processes and fully integrated value chain R&D to end-product by following quality, sustainability, and circularity in aspect of its operations.

1.2 Background

Nickel-based superalloys are now trending in many high-temperature applications. They provide outstanding properties like excellent fatigue resistance, tensile strength, superior corrosion resistance and oxidation resistance at elevated temperatures [1]. Inconel 718 is a workhorse precipitation-strengthened alloy that is widely used in aerospace and oil and gas industries. It can offer extraordinary mechanical properties after a standard careful heat treatment of solution annealing and further double aging. The alloy 718 consists of substantial amounts of niobium and molybdenum along with aluminum and titanium. However, there have been several experiments that have proved that this superalloy IN 718 always loses their ductility and embrittlement at intermediate temperature, which has restricted their further development [2].

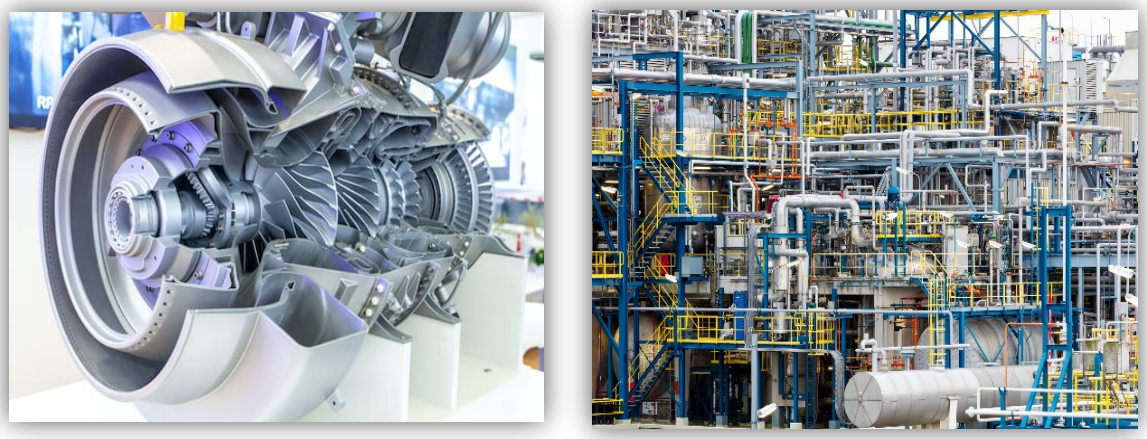

Figure 1.1 Pictures representing the IN718 materials used in real applications Aerospace industry and oil and gas industry.

1.3 Objective

The objective of the project is to find the underlying mechanisms responsible for the embrittlement and loss of mechanical properties such as strength and elongation at intermediate temperatures of the nickel-based superalloy alloy 718.The project is aimed to investigate of material deformation under different strain rate and temperature condition. To accomplish this, hot rolled and heat-treated Inconel 718 samples are undergone tensile test with different strain rate for understanding the material behaviour at intermediate temperature. Finally, the results from mechanical testing and microstructure analysis compared to determine the potential mechanism behind the embrittlement behaviour of alloy 718 at intermediate temperatures.

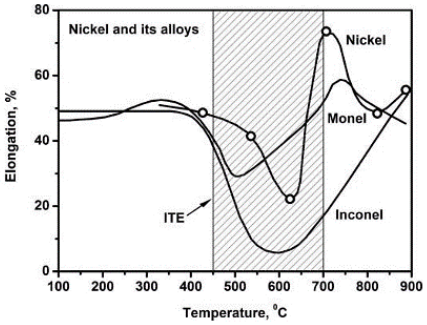

Figure 1.2 shows the loss ductility upon tensile deformation for nickel based super alloys [1]

1) Identify the possible deformation mechanism related to loss in ductility or embrittling behaviour within the temperature range of 500-700°C, based on literature studies.
2) Design and perform the heat treatment for the samples for activating precipitation hardening mechanism.
3) Perform tensile test at different temperature and different strain rate for understanding the variation in ductility of material.
4) Analyse the deformation behaviour based on microstructure investigation.

1.4 Thesis Plan

1) Objective and problem statement
2) Literature study
3) Test proposal
4) Heat treatment
5) Tensile test
6) Sample preparation
7) SEM-EDS+EBSD+ECCI analysis
8) Obtain results plotting graphs and microstructure images.
9) Results analysis and evaluation
10) Thesis writing

Stage -1
Stage -2
Stage -3

2 THEORETICAL BACKGROUNDS

The purpose of this chapter is to present the essential information studied from various literature studies which are necessary to understand the project. There is a general overview of super-alloy Inconel 718 regarding thermomechanical deformation behavior and basic embrittlement mechanisms at intermediate temperatures throughout the chapter.

2.1 Material -Inconel 718

Nickel-based superalloy Inconel 718, first introduced in the late 1950s. The material finds widespread use in high-temperature applications such as manufacturing critical parts in aeronautical, astronautical, oil and chemical industries [1]. High temperatures and harsh environments are not a problem for hot rolled Inconel 718, and it exhibits excellent mechanical properties and corrosion resistance. The Inconel 718 material consists of a γ matrix, which is reinforced by a blend of precipitates including Ni_3(Ti, Al)-γ' and Ni_3Nb-γ''. Additionally, it contains carbides and the δ phase enriched with Nb.

Gamma matrix - γ

The matrix phase of IN-718 with FCC structure can exist until melting temperature (no phase transformation up to Tm). This solid solution consists of Fe, Cr, Mb, W, V, and Al, which have more considerable atomic size differences than Nickel. It is the prime reason for the hardening effect called solid solution strengthening.

Gamma prime (γ')

The primary strengthening precipitate in Inconel 718 is the Gamma prime γ' with FCC LI_2 phase Ni_3(Ti, Al) with spherical morphology. This precipitate undergoes initial nucleation and grain growth at the grain boundaries within a temperature range of approximately 650-850°C. It is uniformly distributed throughout the Gamma matrix, and the crystallographic structure of Ni_3(Ti, Al) is identical to that of the Gamma matrix. As a result, the precipitate and the matrix share coherent boundaries, meaning they have a close match in their lattice parameters. The near-identical lattice parameters of both the Gamma matrix and the Ni_3(Ti, Al) precipitate play a crucial role in the precipitation kinetics and strengthening characteristics of the alloy. This similarity enables efficient diffusion and atomic mobility between the matrix and the precipitate, promoting the nucleation and growth of the precipitate. The controlled composition of gamma prime in alloy by heat treatment process to provide strengthening effect.

Gamma double prime (γ'')

The IN-718 material is strengthened not only by γ'instead there is another precipitate called Gamma double prime γ'' at peak aged condition. It has Ni_3Nb composition with BCT DO_{22}. It has disc shaped intermetallic precipitates under microscopy. Normally forms coherent with γ' and semi coherent with Gamma matrix γ distributed uniformly in gamma matrix

around 600-850℃ [1]. Material has good hardenability as well as weldability is due to sluggish precipitation kinetics.

Delta phase (δ)

The δ phase is characterized by an ordered orthorhombic DO_a structure and elongated needle-like shapes on grain boundaries, twin boundaries and within grains A minor proportion of this phase inhibits the growth of grains during solution and aging processes while it can also be intentionally precipitated via a heat treatment known as “delta dump”. Presence of delta phase has adverse effects that compromise fracture toughness, strength, and creep resistance.

At high temperature approximately above 900℃ , the delta phase precipitates directly from austenite and at intermediate temperature γ'' phase grows when increase temperature and it replaces by delta. The $\gamma''$is a metastable in nature so when it gets the favoured situation it changed to stable nature is known as the delta.

Carbides

The cubic structured MC and $M_{23}C_6$ are the most commonly observed in nickel-based superalloy IN 718. Carbides are normally formed at grain boundaries during solidification or heat treatment. A minor amount of C is added to this alloy, forming MC-type carbides such as (Ti, Nb)C. These carbides are present at GBs and inhibit GB sliding, improving the high-temperature creep resistance properties. C content is kept to a minimum to facilitate Nb and Ti precipitation in the γ matrix.

Topological closed pack Laves Phase

Laves phases are clustered during the manufacturing process and negatively impact on the mechanical properties. The formation of these phases primarily relies on the presence of niobium. An approximate Nb content of 15-25% promotes the formation of laves phases, which can decrease the quantity of gamma double prime precipitates essential for precipitation strengthening. Homogenization at a temperature of 1150°C for an extended period can eliminate these phases.

Table 2 and Table 3 show summaries of possible phases or precipitates and the roles of the alloying elements in Alloy 718.

Table 2.1 Phases possibly present in the IN718 alloy after heat treatment and details.

Phase	Composition	Crystal structure	Particle morphology	Temperature range (°C)	Effect
γ'	Ni_3(Ti, Al)	FCC L_{12}	Spherical	650-850	Precipitation hardening
γ''	Ni_3Nb	BCT $D0_{22}$	Disc	620-900	Precipitation hardening
δ	Ni_3Nb	Orthorhombic $D0_a$	Plates	750 to 1020	Grain growth inhibition (few qty)
laves phase	Nb rich	HCP	Plates	During processing	Effect mechanical properties
carbides	Nb rich			1200	Inhibit grain sliding at grain boundary

Table 2.2 chemical elements and effects [8]

Elements	Effect
Nickel	Stabilize Matrix phase
Niobium	Precipitation hardening, Carbides
Titanium	γ' former, Precipitation hardening, Carbides
Aluminium	γ' former, corrosion resistance
Chromium	Solid solution hardening, corrosion resistance
Molybdenum	Solid solution hardening
Carbon	Grain boundary strengthening

2.2 Plastic deformation of metals

Metallic materials undergo deformation when subjected to external forces, which is influenced by their microstructure, mechanical properties, and loading conditions. Unlike elastic deformation, plastic deformation is irreversible and persists even after the removal of forces. In manufacturing processes, intentional plastic deformation is utilized to achieve desired shapes. Consequently, understanding the factors that influence plastic deformation plays a crucial role in comprehending material behavior during manufacturing. This chapter provides a literature review on mechanisms related to plastic deformation.

Crystalline defects

Most metals and alloys exist as polycrystalline solids, meaning they consist of numerous crystals or grains. These crystals possess a highly organized arrangement of atoms or molecules known as a crystal structure or crystal lattice. The lattice pattern repeats in all directions and is referred to as a unit cell. The individual crystals within a solid material are commonly referred to as grains. When it comes to plastic deformation, which occurs when a material undergoes permanent changes in shape, the behavior is influenced by defects within the crystal lattice. These defects are disruptions in the regular crystal structure and can be classified into four categories based on their spatial dimensions: point defects, line defects, planar defects, and volume defects. The primary mechanism of plastic deformation in metals is the movement and propagation of dislocations. Dislocations play a crucial role in the deformation process by allowing atoms to shift and rearrange within the crystal lattice [2].

Dislocation slip

A slip system refers to a collection of symmetrically identical slip planes and slip directions, which allow for easy movement of dislocations. These slip planes and directions are described using the Miller index notation [2]. Specifically, slip occurs along densely packed planes and directions where the atomic density is highest. The orientations of slip systems differ from one grain to another. At low or moderate temperatures ($T < 0.5Tm$, where Tm represents the melting temperature) dislocation slip becomes the dominant mechanism of deformation.

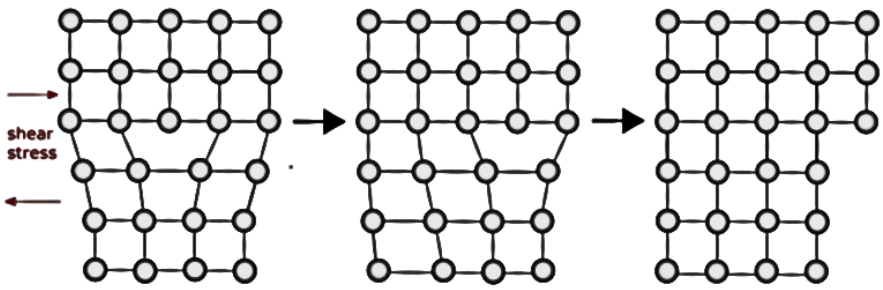

Figure 2.1 Edge dislocation glide Mechanism [2]

Dislocation climb

Dislocation Climb is a thermally activated mechanism driven by the diffusion of vacancies through the crystal structure, to or away from the site of dislocation. It allows edge dislocations to move in a direction perpendicular to the slip plane to overcome obstacles, as illustrated in Figure 2.2. Being a diffusion process, the importance of this mechanism increases with the temperature [2].

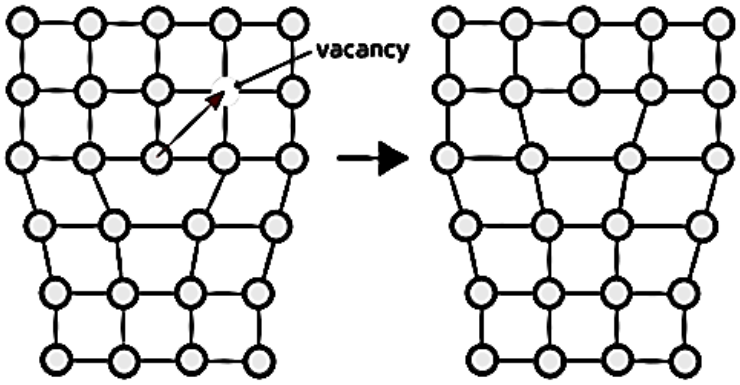

Figure 2. 2 Dislocation climb mechanism [2]

Strengthening mechanism

The movement of dislocations governs plastic deformation, but it can be hindered by various obstacles. These obstacles are typically associated with defects present in the crystal lattice play a role in strengthening the material by impeding the motion of dislocations.

Strain hardening

The movement of dislocations within a material is significantly influenced by their interactions with each other, which can hinder their paths. As plastic deformation increases, the density of dislocations and their interactions make their movements more challenging. Finally, increase the resistance to slip necessitating a higher shear strain to sustain motion, which leads to an increase in flow stress.

Two types of dislocation interactions can occur:

Dislocation pile-up: This occurs when dislocations accumulate in a specific region, creating a barrier to the movement of subsequent dislocations.
Dislocation entanglement: This happens when dislocations become entangled with each other, impeding their individual motion. These interactions contribute to the overall strengthening of the material and impact its mechanical properties.

Grain boundary strengthening

Grain boundaries serve as barriers to dislocations, making them influential in determining the strength of a material. A fine microstructure characterized by small grain sizes enhances material strength due to the larger grain boundary area. This phenomenon, known as the Hall-Petch effect. Grain boundaries exert a significant influence on the properties of polycrystalline materials, and therefore, the grain size is an important material parameter that profoundly impacts the deformation behavior.

Precipitation strengthening

Precipitation hardening, also known as precipitation strengthening, involves the introduction of fine precipitates such as γ' & γ'' into a material. These precipitates typically represent additional phases within the material. When the precipitates are sufficiently small, they are considered can shear, allowing dislocations to cut through them as shown in figure 2.3 (a). In contrast, larger precipitates that cannot shear cause dislocations to bow around them by arresting dislocations creating an Orowan loop as shown in figure 2.3 (b) [2].

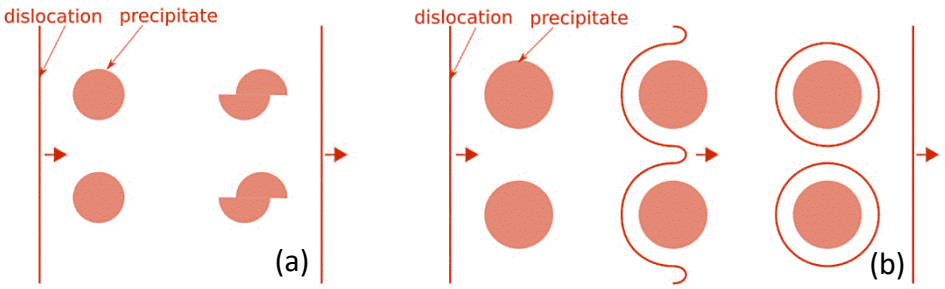

Figure 2. 3 a) Dislocations shearing through precipitates. b) Dislocations bowing around a Precipitate [2].

Precipitation hardening involves a series of aging treatments that are carefully designed to achieve optimal mechanical properties by controlling the volume fraction, distribution, morphology, and spacing of the precipitate phase within a material. The typical temperature range for these aging treatments is between 600 and 850°C, with durations ranging from 2 to 24 hours for the precipitation of γ' & γ'' phases, and between 700 and 1000°C for various carbide phases. It is also dependent on size and shape of specimen.

The standard heat treatments are designed for effective way to do precipitation hardening. It is purely dependent on applications and desired properties required. This quenching helps to retain the desired microstructure and ensures the effectiveness of the precipitation hardening process [3].

Solid solution strengthening

Solid state strengthening involves the introduction of atoms from a different element into the crystal structure of a base material. This can result in two types of solid solutions, depending on the size relationship between the solute and base material atoms. A substitutional solid solution occurs when there is similar-sized atom incorporation, while an interstitial solid solution forms when smaller solute atoms occupy spaces within the larger base material atoms [2].

The incorporation of Cr and Mo is crucial for the solid solution strengthening mechanism in alloy IN718 due to differences in atomic sizes. By introducing these alloying elements into the crystal lattice, the strength, hardness, and overall mechanical performance of alloy 718 are improved through solid solution strengthening. The introduction of dissolved atoms generates strain within the lattice structure and restricts dislocation motion, which is responsible for plastic deformation in metals. The solid solution strengthening effect in alloy 718 is highly effective due to the compatibility of alloying elements with the nickel matrix. Elements like Nb, with similar atomic radii and chemical affinity for nickel, promote a stable and homogeneous microstructure through solid solution formation. The manufacturing processes involved in producing Inconel 718, such as solution annealing and aging, further enhance the strength achieved through solid solution strengthening. These treatments enable controlled diffusion and precipitation of additional phases like γ" and γ' precipitates that contribute to reinforcing the alloy's structure [2,3].

2.3 Mechanism literature study

Embrittlement mechanisms in nickel-based superalloys can be attributed to several factors, including intergranular precipitates, dynamic strain aging, glide plane decohesion, and gas phase embrittlement. This literature study explained each mechanism.

1) Intergranular Precipitates:

Intergranular precipitates have been recognized as one of the primary factors causing embrittlement in nickel-based alloys. Studies dating back to 1925 by Merica and Waltenberg identified the formation of a Ni-Ni_3S_2 eutectic film at grain boundaries because of sulphur (S) contamination, leading to reduced ductility as shown in figure 2.4. At lower temperatures, smaller precipitates have minimal impact on crack initiation, thus preserving high ductility. However, at intermediate temperatures, larger intergranular precipitates facilitate crack initiation and result in reduced ductility. At higher temperatures, the dissolution of precipitates restores the ductility of the alloys [1,5].

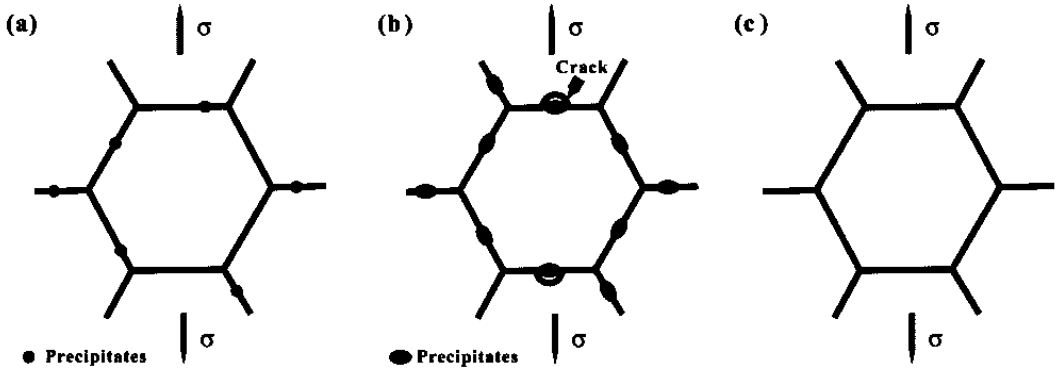

Figure 2.4 Shows ITE due to Intergranular Precipitates [1]

2) Gas Phase Embrittlement

Studies have demonstrated that nickel-based superalloys can experience brittle intergranular failure and decreased ductility when exposed to aggressive environments, especially with oxygen infiltration at moderate temperatures as illustrated in figure 2.5. At lower temperatures, there is limited oxygen penetration and grain boundary sliding which leads to increased ductility. As the temperature increases, oxygen penetration along grain boundaries occurs causing the pinning effect to the boundaries and subsequent embrittlement occur. The presence of oxygen weakens grain boundaries, making them more susceptible to cracking under stress. In addition, oxygen can cause oxidation of grain boundary particles such as carbides, sulfides, and delta phases. This continuous oxide

formation or the presence of oxide particles in the boundaries prevents sliding or migration and leads to cracks and a significant decrease in ductility. However, at high temperatures, the energy gained by the boundaries allows for dynamic recrystallization and recovery of ductility by overcoming these barriers. Higher levels of moisture in the test environment introduce hydrogen as a primary embrittling species, which is known as gas-phase embrittlement [1,7].

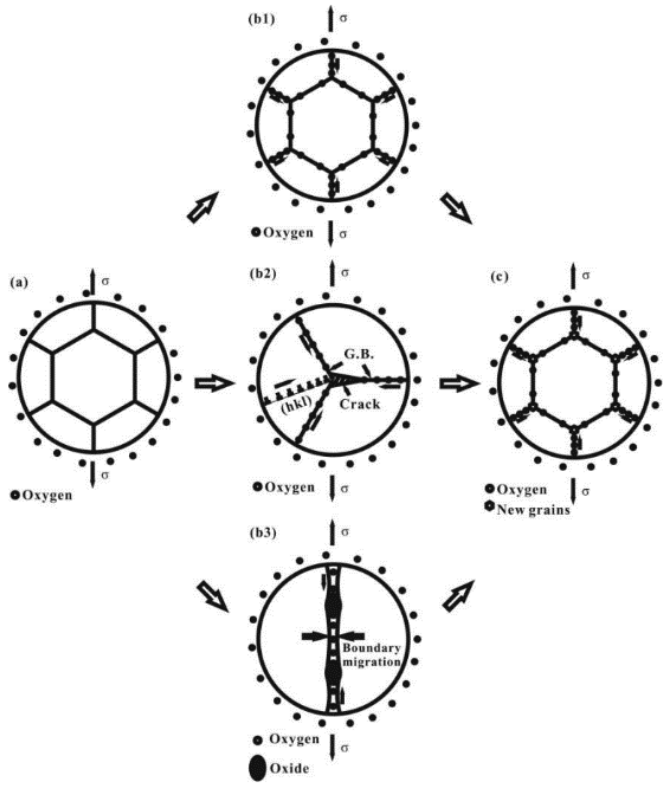

Figure 2.5 Shows the ITE due to Dynamic Strain Aging [1]

3) Glide Plane Decohesion

The concept of glide plane decohesion was proposed by Jensen and Tien in 1985 as shown in Figure 2.6 [1]. They suggested that deformation behaviour is homogeneous or localized then possibility of ductility variation with temperature. At low temperatures, deformation is inhomogeneous and restricted to a few slip bands. As the temperature increases, the mobility of dislocations increases, leading to more dislocations being trapped at the γ/γ interface. Continuous dislocation movement boosts stress concentration at the interface and resulting in glide plane decohesion. At higher temperatures, the thermally activated dislocation climb becomes the dominant mechanism, that is leading to more homogeneous deformation and recover ductility. Therefore, an intermediate temperature range exhibits minimum ductility due to localized strain inhomogeneity [1,6].

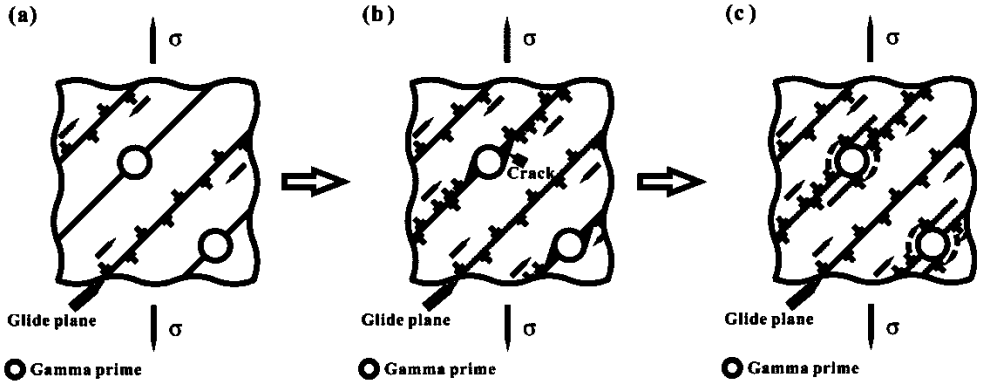

Figure 2.6 Shows Mechanism due to Glide Plane Decohesion [1]

4) Dynamic Strain Aging:

At low temperatures, the less mobility of solute atoms compared to dislocations allows for normal dislocation multiplication and movement and resulting in relatively high ductility. At intermediate temperatures, solute atoms dynamically cluster around migrating dislocations, forming Cottrell atmospheres due to accelerated mobility as observed in figure 2.7. These atmospheres impede dislocation movement, leading to reduced strain distribution and decreased ductility. Further increasing temperatures, the clustering tendency reduces, and dislocations are free from the impediment of solute atoms and restoring ductility [1,4].

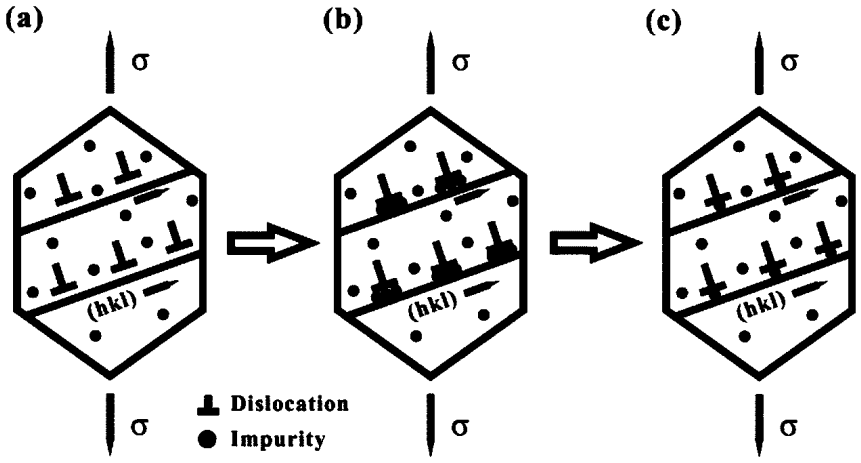

Figure 2.7 shows Mechanism due to Dynamic Strain Aging [1]

2.4 Heat Treatment

Nickel based super alloy IN718 is a precipitation-strengthened alloy that can provide high strength and elongation at high-temperature service applications. The strengthening mechanism is responsible for improving the strength of the material at high temperatures and it is achieved only after heat treatment called precipitation hardening aging after the manufacturing process & ST. The strengthening phases such as γ'' and γ' are stick with the gamma matrix and provide high strength to the material during precipitation hardening heat treatment known as aging. In addition to that strengthening phase gamma double prime is metastable in nature and tends to transform into delta at certain temperature hike. So, it is mandatory to optimize heat treatment by controlled heating, soaking, and cooling to avoid the generation of unnecessary phases that are detrimental to the strengthening mechanism. Theoretical and prediction-based thermodynamics modelling tools are necessary to obtain a well-defined heat treatment method. The precipitation hardening mechanism involves several stages, such as solution annealing at an elevated temperature of approximately 1050℃ followed by quenching, then again raising the temperature at which formation precipitates, then holding its specific time, then cooling by either air cooling or furnace cooling that depends upon the application of the material. The advantage of stage-1 solution annealing is to dissolve all phases in matrix and water quenching enables to freeze the desired microstructure condition [9].

Homogenization annealing

Homogenization annealing is employed to reduce or eliminate segregation of unwanted phases. This process aims to dissolve undesirable segregation phases, such as Laves phases, and Nb rich carbides to achieve an even distribution of potential precipitation constituents. Homogenization is typically performed at temperatures above the solvus temperatures of segregated phases around 1160-1170°C with standard exposure time. Slow heating is commonly used to prevent melting at grain boundaries [3].

Stress relief through annealing and Recrystallization

Stress relief treatments are used to reduce residual stress that occurs during joining and working processes. The main objective of these treatments is to prevent distortion, cracking, and improve the ductility of the material for future machining operations. Recrystallization is commonly induced as a result of stress relief treatments in work-hardened materials. The temperature range for stress relief annealing depends on the alloy type and typically ranges from 850°C to 900°C. This process usually takes about one or two hours. Full annealing involves complete recrystallization and softening of the material. The temperature range for full annealing varies between 955°C and 1080°C with a duration of approximately 1-4 hours. [3].

Solution annealing

All precipitates in the matrix and grain boundary dissolve after this treatment. This heat treatment is commonly used to prepare an alloy for precipitation hardening without any other unwanted precipitates. The temperature for solution annealing is determined by the solvus temperatures of the precipitate phases. This is typically ranging from 900 to 1050°C for the gamma prime and gamma double prime phases and 900 to 1100°C for carbides. It is common to choose solution anneal temperatures slightly below the solvus temperatures to retain a small fraction of the precipitate phase and inhibit grain growth. After solution annealing, the alloy is rapidly cooled to freeze the archived condition as well as prevent premature reprecipitation before the precipitation-hardening aging treatment [3].

Precipitation hardening

Precipitation hardening involves multiple step heat treatments for achieving optimal mechanical properties through the appropriate fraction, distribution, morphology, and particle spacing of the precipitate phase. The typical aging treatments for γ'' and γ' precipitation range between 600 and 850°C for 2-24 hours, while various carbide phases require temperatures between 700 and 1000°C. Nb is the key element for introducing this precipitate into matrix and act as binders for strengthen the material. Time of exposure during heat treatment provides uniform distribution of gamma and gamma prime in matrix. During deformation these nano precipitates can fight with dislocations and provide strain hardening effect to the material. These heat treatment processes play a vital role in optimizing the properties of nickel-based superalloys, such as Inconel 718, by controlling the microstructure and precipitation behaviour [3].

2.5 Uniaxial Tensile testing at different temperature

The uniaxial tensile test is a commonly used and fundamental experimental method in materials science for evaluating the mechanical properties. The process involves applying tension to the specimen until it fails while simultaneously recording data on force and elongation. This analysis provides crucial information such as Young's modulus, strain hardening behaviour, yield strength, ultimate tensile strength and maximum elongation. This mechanical test has important role in engineering applications such as material selection and design procedures. The tensile test specimen has threaded ends for gripping. The gauge section is an important part of the specimen since deformation and failure occur only in this section. Testing machine MTS landmark servo hydraulic test system and it includes a furnace for conducting tensile tests at high temperatures. Additionally, a major part of measuring the gauge length upon testing is the extenso meter made by MAYTEC PMA. At regular intervals throughout the test, the load and elongation are measured and then converted to average stress and strain values using the equations provided in the previous section. To conduct a tensile test, it is necessary to affix the specimen to a suitable apparatus, as outlined in the preceding section and apply tension to it. The resulting tensile force must then be measured in relation to the corresponding elongation of the gage length.

The term Engineering stress denoted by σ. It can be calculated as

$$\sigma = F/A_0 \quad (2\text{-}1)$$

where F represents the applied tensile force & A_0 is the initial cross-sectional area of the gage section.

Engineering strain represented by ε

$$\varepsilon = \Delta L/L0 \quad (2\text{-}2)$$

where L0 denotes the initial gage length, and ΔL stands for the change in gage length (L - L0).

True stress and true strain

$$\text{True stress } \sigma_t = \sigma (1+ \varepsilon) \quad (2\text{-}3)$$
$$\text{True strain } \varepsilon_t = \ln (1+ \varepsilon) \quad (2\text{-}4)$$

True stress accurately measures material stress during deformation by considering the instantaneous area and dividing it into the applied load. This shows how well a material can resist load as its dimensions change. True strain, on the other hand, describes actual deformations compared to the original length using logarithms of differences in lengths throughout testing for more dependable data collection. Simply put, true stress and true strain help us understand how strong a material is and how much it can bend before breaking. This information is important when choosing materials for different applications to ensure they will perform as expected under pressure. Knowing the behavior of these factors also allows experts to assess structural integrity, predict failure modes, identify design limits, and evaluate the external load's impact on the structure's resilience properties, among other necessary safety measures needed in designing safer structures that are more dependable [10].

Effect of High Temperature on Material Behavior and Fracture

Temperature significantly impacts the properties of material by improving the strength and elongation. However, these properties can vary greatly when heated or cooled material. Typically, increasing the temperature of material results in a decrease in strength due to reduced energy required for plastic flow, while its ductility increases. However, certain temperature ranges may cause structural changes such as precipitation, strain aging, or re-crystallization, altering this general behavior. Therefore, it is crucial to understand the properties of materials at elevated temperatures for certain applications, particularly the hot

working of materials or any scenarios where a component is exposed to high temperatures for an extended period [11].

2.6 Microstructure characterization

The microstructure of the tensile-tested specimens was examined using a FEG-SEM. The specific microscope used was the ZIGMA VP FEG-SEM with Gemini Column, manufactured by ZEISS. It was equipped with multiple detectors, including In Lens, secondary electron (SE), backscattered electron (BSD), EDS, and EBSD detectors. The characterization process was conducted under high vacuum conditions, although the voltage settings varied depending on the type of examination. The analysis settings employed are outlined below. To investigate the presence of precipitates and fine particles, the analysis utilized low voltage (<7kV) to medium voltage (10kV) settings with BSD/SE detectors. Higher voltages were avoided as they could result in overlapping with the matrix due to a larger interaction volume caused by increased energy input and penetration depth. EDS analysis was also performed within the same voltage interval. For EBSD measurements, high voltage (20kV) was utilized. To enhance contrast and clarity of images obtained with the BSD-detector were given preference. This choice was made because variations in atomic numbers among elements led to clearer differentiation of areas with different chemical compositions. This contrast enhancement assisted in distinguishing the characteristics of each phase during analysis.

The expected volume of data generated during the analysis was managed using a suitable database, specifically the Mobility Data platform. This platform facilitated efficient storage and organization of the acquired data for further analysis and interpretation.

EDS

To estimate the chemical compositions of the precipitates or phases of interest, Energy Dispersive X-ray Spectroscopy (EDS) analysis was conducted. The EDS analysis utilized an X-MAX 50 detector manufactured by Oxford Instruments, which was controlled using the accompanying Aztec crystal software. Three different types of EDS analysis were employed.

- Single point analysis
- EDS mapping of a region
- Line scan

Fractography

Fractography analysis following the tension test was carried out using a FEG-SEM equipped with a secondary electron (SE) detector. Prior to the fracture analysis, the samples underwent a thorough cleaning process using ultrasonication in acetone for a duration of 5 minutes. The fractured portion of the samples was securely placed in the SEM holder to facilitate examination and imaging using the FEG-SEM system.

Electron backscattered diffraction image

The EBSD technique is widely used for the characterization of crystalline materials as it can provide valuable information about the crystallographic orientation and phases of the material. It can provide the mechanical deformation details in connection with microstructure. An automatic EBSD system is composed of an EBSD detector and a SEM. The EBSD detector includes a phosphor screen and a CCD camera that are linked to a computer for image processing. The figure illustrates the setup. Typically, tilting the sample 70° from the horizontal axis is necessary to generate patterns with sufficient intensity. The prime intention of the EBSD analysis is to find the deformation behaviour after uniaxial tension test. It is providing the crystallographic information along with microstructure with good penetration capability. Crystallographic information can be used to analyse the plasticity of deformed sample in terms of KAM analysis as well as grain boundary angles. Geometrical necessary dislocation is quantitatively analysed by using EBSD scan and data analysis with external softwires. In this study, EBSD is used to analyse the deformation behaviour of samples by KAM and disorientation angles of grain boundaries to study about plasticity [12].

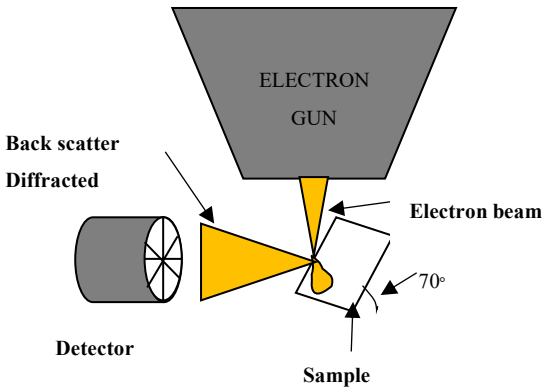

Figure 2.8 Pictorial explanation of EBSD working set up.

Electron Channelling Contrast Imaging (ECCI)

The Electron channelling contrast imaging is an effective method employed in the scanning electron microscope to observe various types of crystal defects, such as dislocations, stacking faults, twins, and grain boundaries. Electron Channelling Contrast Imaging is a technique that relies on the phenomenon of electron channelling through a crystalline substance to generate contrasting images based on crystallography [13]. By utilizing backscattered electrons, ECCI produces contrast in the form of channels within the material. The amount of backscatter experienced by an electron depends on its proximity to the scattering atom's nucleus. Consequently, different orientations of the lattice relative to the incident beam result in varying numbers of backscattered electrons. This method is utilized

for assessing the deformation characteristics when comparing images. Specifically, in this investigation, the focus lies on analysing slip and twin deformations after subjecting a material to tensile forces. It is essential that the specimen undergoes proper polishing to prevent any scratches since a low working distance is employed.

The combination of ECCI with EBSD offers a highly efficient and rapid method to examine crystal defects, such as dislocations, cells, and stacking faults while controlling diffraction conditions to enhance contrast. EBSD-based ECCI approach for microstructure characterization, including the characterization of single dislocations, measurement of dislocation densities, and characterization of dislocation substructures in deformed bulk materials.

3 MATERIALS AND EXPERIMENTAL METHODS

3.1 Material

The starting material was cast alloy 718 that is rolled into the plate and bar form and plate form sample designated as No-3 and bar form is designated as No-2. The detailed material composition can be seen in Table 3.1. The No-3 was undergone heat-treatments such as homogenization, solution annealing and double aging as standard heat-treatment procedure. However No-2 exempted from homogenization for analysing laves phases involvement on mechanical properties. The detailed explanation has been provided in table 3.2. The figure 3.1 is the graphical visualization for heat treatment method performed for No-3.

Table 3.1 chemical composition of alloy 718 in weight percentage.

IN718	Ni	Cr	Fe	Mn	Si	Al	Ti	C	Nb	Co	Cu	W	Mo	V	B
Wt%	51.94	19.12	19.4	0.22	0.27	0.43	0.99	0.017	5.04	0.01	0.01	0.001	2.55	0.001	0.001

3.2 Heat treatment

Heat treatment is the essential part of this experiment to introduce strengthening phases gamma prime and gamma double prime, stress relieving and dissolving all precipitate and carbides. In this experiment we used two different types of heat treatment methods for analysing the heat treatment difference affecting the microstructure and subsequent changes in mechanical properties upon deformation. Both double ST and aging method is used for heat treatment process that designed with reference to TTT diagram and CCT diagram generated by using JMAT pro software as discussed below. diagrams for Alloy 718 calculated by JMAT. They will be described in the later chapter.

Table 3. 2 Heat treatment performed for material No-2 and No-3

Sample	Homogenization	Solution Annealing	Aging	Aging
No-2	NA	980℃(WQ)	720℃ (FC 5℃)/Min	620℃(AC)
No-3	1150℃(WQ)	980℃(WQ)	720℃ (FC 5℃)/Min	620℃(AC)

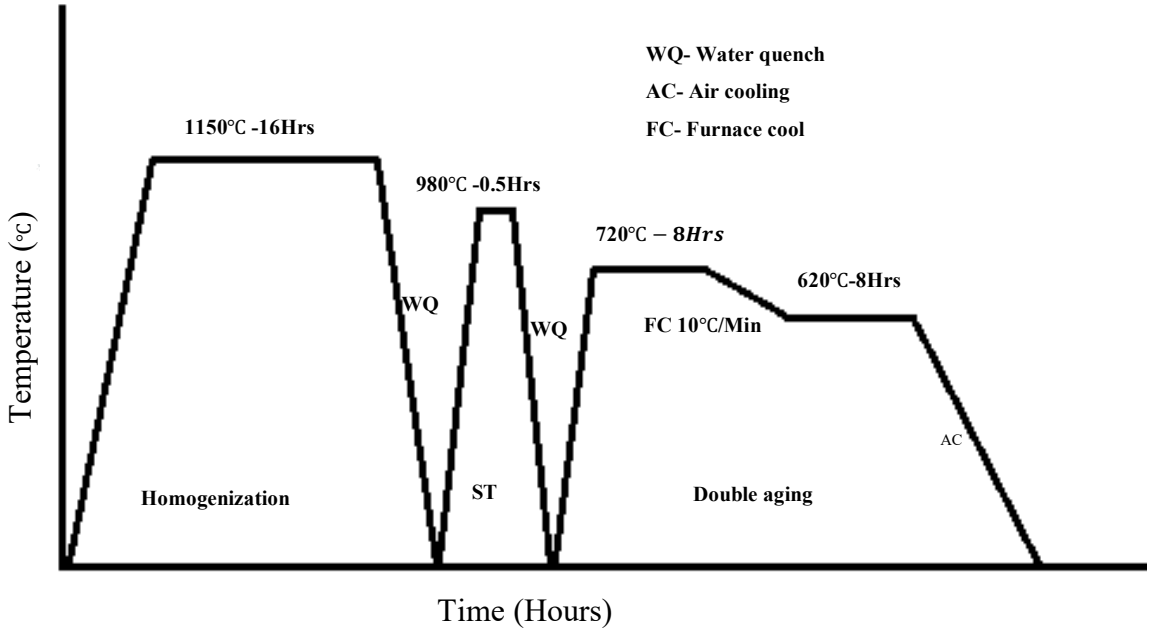

Figure 3.1Temperature vs time plot for heat treatment process brief pictorial view.

3.2 Tensile test

The initial stage in conducting a tensile test involves the preparation of the specimen, which must adhere to the guidelines outlined in ASTM E8. The gauge length of the sample is measured and recorded. The dimensional assessment is carried out using stereography, and the accuracy of the measurements is ensured by utilizing a calibrated micrometre. According to the standard, the gauge length should be five times the diameter. The figure 3.2 shows the dimensions and shape of the samples used for uniaxial tension test. However, slight deviations may exist between the actual measurements and the specified dimensions.

Table 3. 3 Tensile test sequence as per temperature and strain for samples No-2 and No-3.

Strain Rate	Temperature (℃)		
	RT	650	750
10^{-1}	No-3	No-3	No-3
10^{-2}	No-2	No-2	No-2
10^{-3}	No-3, No-2	No-3, No-2	No-3, No-2
10^{-4}	No-3, No-2	No-3, No-2	No-3, No-2

The MTS Landmark servo hydraulic test machine was utilized in this experiment to conduct various tests. This machine allows us to customize the temperature and strain rate based on the specific requirements of each test. After preparing the sample, which involved primary marking and measurements of gauge length and diameter, the sample was positioned at both ends of the grip. To ensure accurate temperature readings, all temperature sensors were carefully positioned to contact the sample and grip. Furthermore, the test area was securely enclosed for safety purposes. Once the sample and sensors were in place, the extensometer was attached to the sample. Finally, commands were given to the computer, which was linked to the test machine, to initiate the testing process.

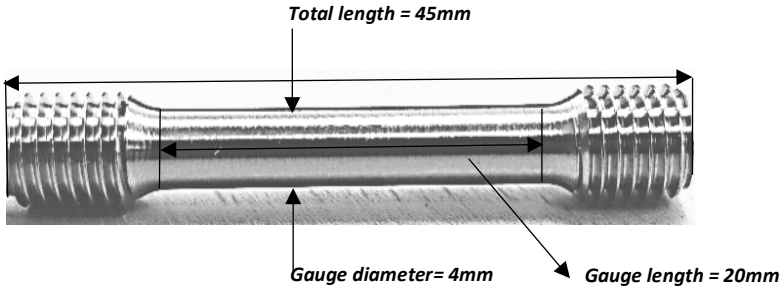

Figure 3.2 shows the sample prepared for uniaxial tension test with dimensions.

3.3 Metallographic preparation

To evaluate and analyse the microstructural evolution and stability of the tensile tested specimens, it was necessary to prepare them before conducting any characterization. The following procedures were used to ensure the specimens were properly prepared for analysis. The figure 3.3 explains brief overview about the sample preparation method followed for this entire project. Firstly, the tensile tested specimens were carefully cut using the Struers Accutom-5 cutting machine. Two specific sections were selected for further examination, the undeformed cross-section and the deformed longitudinal section. The cutting process aimed to obtain precise sections of the specimens for subsequent analysis. The selected specimens were mounted in PolyFast using a CitoPress-30 hot mounting press. This mounting technique involved embedding the specimens in a polymer resin to securely hold them in place during subsequent preparation steps. The mounting process ensured that the specimens were immobilized and protected during grinding and polishing. To achieve a scratch-free surface of high quality suitable for EBSD, the hot mounted specimens underwent a series of grinding and polishing steps using the Buehler AutoMet®-300 grinding and polishing system. Initially, approximately 1.2 mm of material was removed from the deformed longitudinal section using 120/240 grit SiC-paper to reach the central region of interest. Following the coarse grinding step, diamond polishing was performed using a 9/3µm diamond suspension. This step aimed to further refine the specimen's surface, reducing any remaining roughness or imperfections caused by the grinding process.

Subsequently, oxide polishing was carried out using a 0.02µm colloidal silica suspension. This final polishing stage aimed to achieve an extremely smooth surface finish necessary for high-resolution microscopy techniques. Between each stage of grinding and polishing, the specimens were rinsed in water to remove any debris or residual particles. Additionally, ultrasonic cleaning in ethanol was performed to ensure thorough cleaning of the specimens before proceeding to the next stage of preparation.

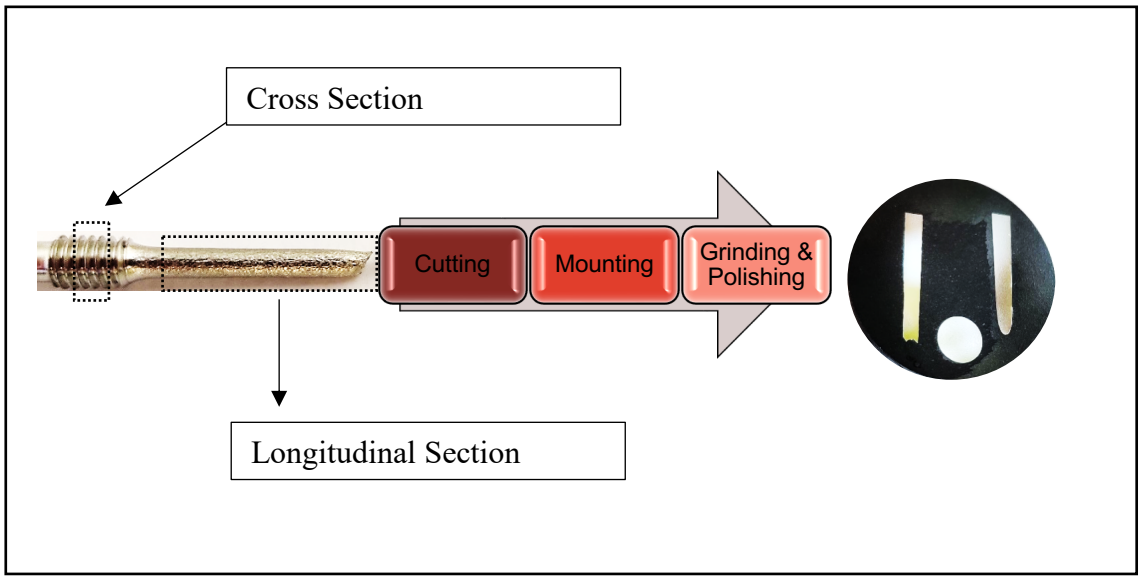

Figure 3.3 shows the sample preparation methods for microstructure analysis.

3.4 characterization method

Microstructure characterization methods play a crucial role in understanding the structural properties of materials. Here are some commonly used methods for microstructure characterization.

Phase identification using EDS technique used in scanning electron microscopy to identify the elemental composition of different phases present in a material. By analyzing the characteristic X-ray emissions from the sample, EDS can determine the chemical composition of specific regions or phases within the microstructure.

Fractography analysis using SEM is a powerful tool for examining the fractured surfaces of materials. By analyzing the surface topography and morphology of fracture surfaces, SEM can provide insights into the fracture mechanisms, crack propagation paths, and the presence of various defects. SEM images can reveal features such as dimples, cleavage planes, intergranular or trans granular fracture modes, which help in understanding the fracture behavior and failure mechanisms.

The deformation behaviour of the samples analysed using a combination of EBSD and ECCI techniques to understand the underlying mechanisms of plastic deformation. The

well-polished samples were securely placed in the EBSD holder and inserted into the FEG-SEM chamber. The chamber undergoes a vacuum-filling process to ensure optimal imaging conditions. The EBSD detector was positioned at a 70-degree tilt toward the sample to capture the diffraction patterns. A small step size was utilized during scanning to accurately index each Kikuchi band, providing detailed crystallographic information in a localized area. The EBSD scan data was saved and later analysed using Aztec crystal software to identify twin deformations based on high-angle grain boundaries, typically with a CSL value greater than or equal to 60 degrees. The MTEX MATLAB package is employed to confirm the presence of twin deformations further using the detected high-angle grain boundaries. The ECCI technique also performed in the same FEG-SEM setup, utilizing a short working distance. ECCI relies on backscattered electrons to create contrast images, specifically targeting the locations where EBSD measurements conducted. Combining EBSD and ECCI methods allows for a comprehensive analysis and verification of twin deformations in the samples.

4 RESULTS AND DISCUSSIONS

This chapter will discuss the results obtained from Thermo-Calc, JMATPRO modelling for heat treatment process, deformation behavior by tensile test results, fractography and microstructure analysis of samples deformed with different temperature and strain rate.

4.1 Simulation results - Heat treatment

Thermo-calc equilibrium diagram presented in figure 4.1 holds the significance of two parameters: the solvus temperature of the phases and the weight percentage of the phase that can be formed at RT through adequate heat treatment. These values are indicated explicitly for the γ' and δ phases. The equilibrium diagram 4.1 illustrates the mol fraction of the γ' phase, indicated by the yellow line, at various temperatures ranging from 600 °C to its solvus temperature. Similarly, the δ phase is represented by the black line. The solvus temperatures for these phases can be determined by observing the points where the yellow and black lines intersect with the x-axis. The solvus temperature for the γ' phase is measured as 940°C, while for the δ phase, it is 1050 °C. Additionally, in the γ matrix, the wt% of these phases at RT is 12 % for the γ' phase and 15% for the δ phase.

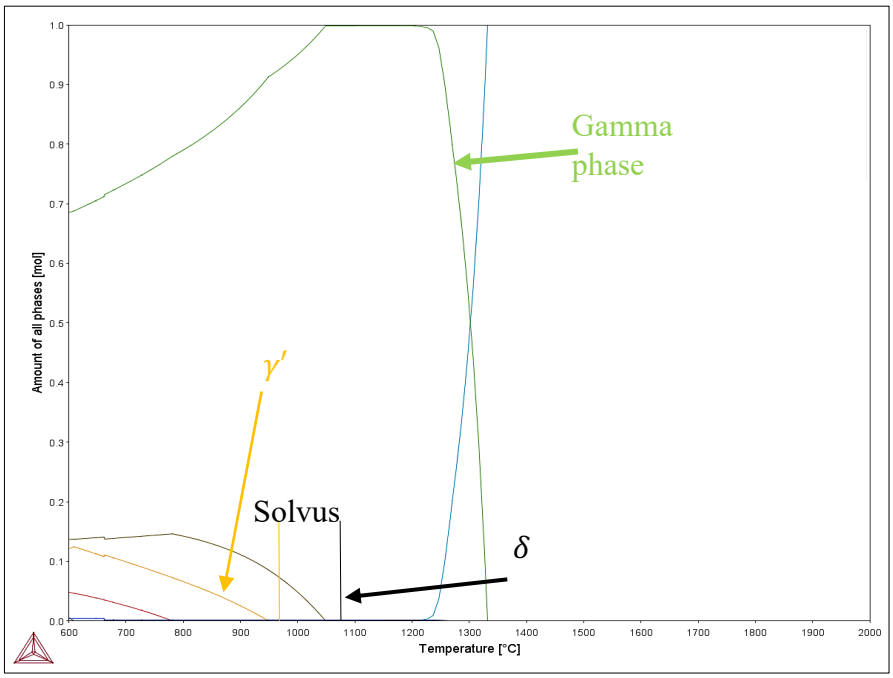

Figure 4. 1 Thermo-calc simulation for predicting the possible phases formation and volume percentage in mol vs temperature.

Thermo-calc Prisma is utilized to simulate the growth rate of precipitates under varying temperature conditions as mentioned in figure 4.2. The simulation results reveal that at 750°C, no significant alteration is observed in the precipitates mean diameter. However, there is a substantial increase in the mean diameter from room temperature up to 400°C. Beyond this temperature, the change in mean diameter becomes minimal, eventually leading to dissolution at the solvus temperature.

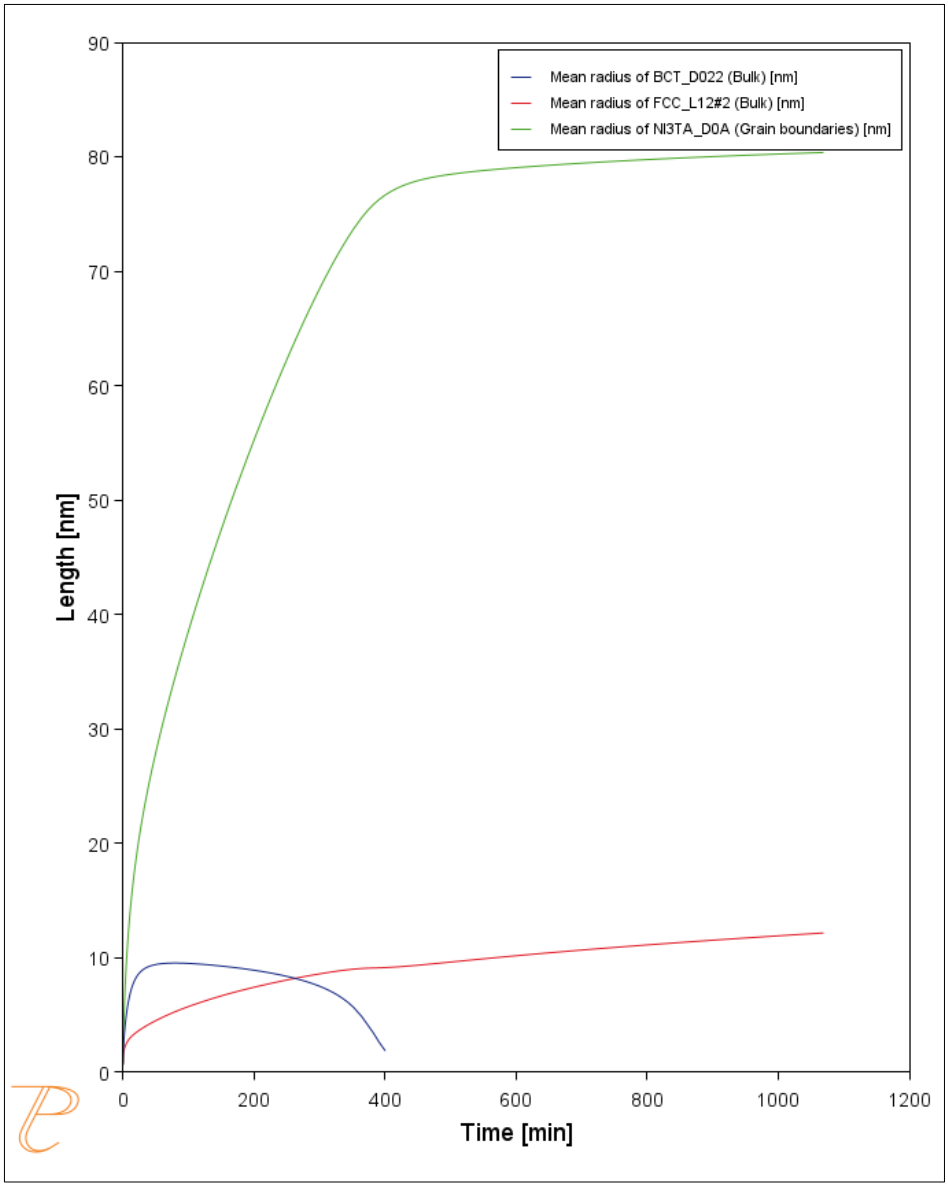

Figure 4. 2 Thermo-calc Prisma precipitation module to analyse the size variation of precipitates.

TTT Diagram

The software JAMAT pro thermodynamic simulation software can predict the possible precipitates or phases at different temperature upon heating and cooling. Figure 4.3 shows the TTT and CCT. The TTT diagram illustrates the duration required for the initiation of transformation in phases γ', γ" and delta phase within the temperature range of 600 to 1050 °C. In the case of the γ' phase, the transformation begins promptly after approximately 7 minutes when the temperature reaches around 840 °C and γ" the transformation begins promptly after approximately 5 minutes when the temperature reaches around 880 °C. As the temperature deviates from this point, both above and below, the time required for transformation initiation increases. Similarly, a similar pattern is observed for the δ phase. However, in contrast to the γ' phase, the precipitation kinetics of the δ phase are significantly slower, which is commonly referred to as sluggish.

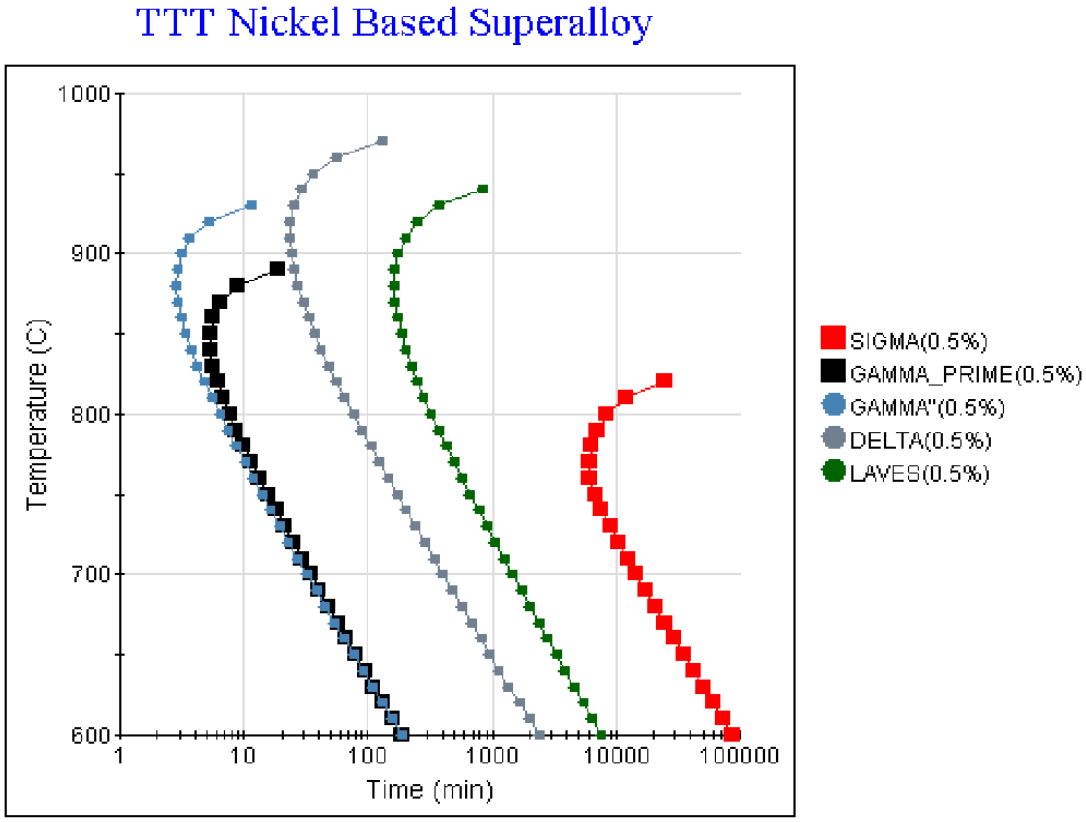

Figure 4.3 Time-Temperature-Transformation JMAT pro for analysing temperature and time relation connected to formation various precipitate.

4.2 Mechanical test results

Tensile tests were performed at room temperature, 650°C, and 750°C with strain rates ranging from 10^{-1}, 10^{-2}, 10^{-3} & $10^{-4}s^{-1}$ are summarised in table 4.1 and figure 4.4 & 4.5. The tensile strength and elongation were compared with different test conditions. The embrittlement phenomena were observed at 650°C and 750°C under low strain rates of 10^{-3} & $10^{-4}s^{-1}$ respectively and resulting in significantly reduced elongation and strength.

Table 4.1 Mechanical test results of samples No-2 and No-3

Sample no	Strain rate	Temperature (°C)	A (%)	Z (%)	Rp0.2 (MPa)	Rm (MPa)
No2	10^{-2} s^{-1}	RT	16,94	25,32	1072	1253
		650	18,51	35,94	817	959
		750	9,77	18,99	678	775
	10^{-3} s^{-1}	750	5,44	12,35	684	735
	10^{-4} s^{-1}	750	3,39	7,88	638	661
No3	10^{-1} s^{-1}	RT	14,03	28,91	-	-
		650	15,62	43,11	754	828
		750	20,65	41,02	631	723
	10^{-3} s^{-1}	750	6,23	20,90	628	638
	10^{-4} s^{-1}	RT	16,99	31,13	964	1099
		650	9,05	33,66	728	773
		750	2,30	7,75	641	677

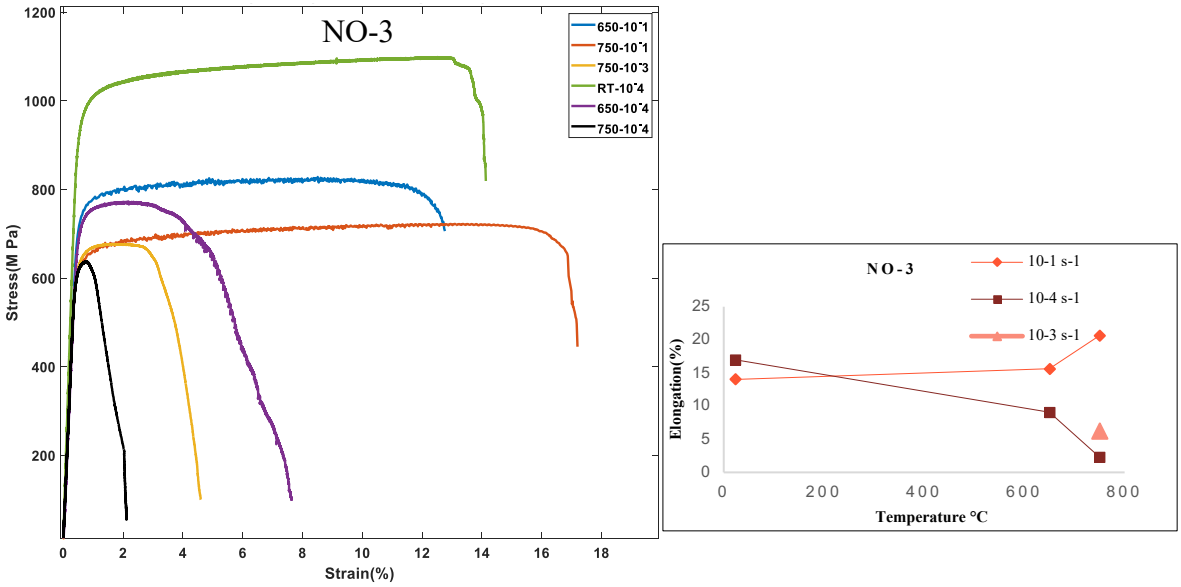

Figure 4.4 shows stress strain plots for samples of NO-3 left and elongation vs Temperature -No-3 right.

Tensile tests were conducted on Sample No. 3 at room temperature RT, 650°C, and 750°C, employing strain rates ranging from 10^{-1}, 10^{-3} & $10^{-4}s^{-1}$. The primary objective was to analyse the stress-strain behaviour of the samples and investigate the effect of temperature

and strain rates on tensile strength and elongation properties. The stress-strain analysis shown considerable variations in the tensile strength and elongation of Sample No. 3 under different test conditions. The sample exhibited high tensile strength at RT with a low strain rate, indicating excellent mechanical properties. In the case of a test performed at 650°C ,750°C with a high strain rate$10^{-1}s^{-1}$, it shows good elongation of nearly 20% compared with RT. As the temperature increased to 650°C and 750°C with a low strain rate, the tensile strength decreased, that is indicating reduced strength at elevated temperatures. The test performed at 650°C and 750°C with strain rates of 10^{-3} & $10^{-4}s^{-1}$ consistently resulted in a decline in both ductility and strength for the sample. The strain rate also played a crucial role in determining the mechanical behaviour of Sample No. 3. Embrittlement phenomena observed at 650°C and 750°C under low strain rates of 10^{-3} & $10^{-4}s^{-1}$ respectively. This embrittlement led to a substantial reduction in elongation and strength percentages. The tensile test data was not recorded by machine at RT with low strain rate $10^{-1}s^{-1}$ due to some technical error and fast response.

The stress-strain analysis and temperature vs elongation analysis of Sample No. 3 displayed temperature and strain rate-dependent mechanical behaviours. The alloy exhibited good elongation at 750°C with high strain rate of 10^{-1} but experienced reduced strength and elongation at elevated temperatures with high strain rate. Embrittlement phenomena were observed at higher temperatures and lower strain rates, leading to a significant reduction in elongation and strength percentages. Higher strain rates were found to free of embrittlement and enhance elongation. These findings provide valuable insights into the behaviour of Alloy 718 under different testing conditions and can provide the optimization of its mechanical performance in practical applications.

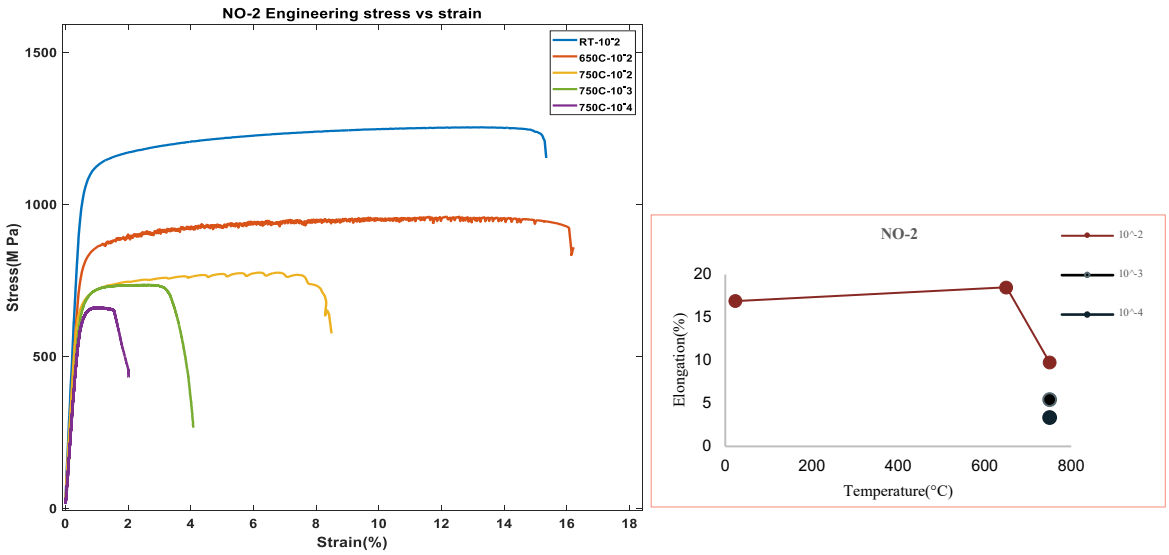

Figure 4.5 shows stress strain plots for samples of NO-2(left) and elongation vs Temperature -No-2(right).

Tensile tests were conducted on Sample No. 2 at room temperature RT, 650°C, and 750°C, employing strain rates ranging from 10^{-2}, 10^{-3} & $10^{-4}s^{-1}$. The primary objective was to analyse the stress-strain behaviour of the sample and investigate the effect of temperature and strain rate on tensile strength and elongation. The sample exhibited high tensile strength at RT with a low strain rate $10^{-2}s^{-1}$,indicating excellent mechanical properties. As the temperature increased to 650°C with a strain rate$10^{-2}s^{-1}$ sample is showing high elongation even compared to RT, but the tensile strength decreased. The test performed at 750°C with strain rates of 10^{-2}, 10^{-3} & $10^{-4}s^{-1}$ consistently resulted in a decline in both ductility and strength for the sample.

4.3 Microstructure analysis and evaluation for material No 3

The material No - 3 is taken from the plate that hot rolled condition and heat treatments homogenization, solution annealing and double aging performed.

4.3.1 Microstructure analysis after heat treatment

After completion of a double aging heat treatment process, the designated sample No-3 is subjected to analysis by cutting out a specific part before tension test. This analysis aimed to determine the phases present within the sample after heat treatment. The EDS point analysis method has revealed the presence of Laves phase, delta phase and Nb-rich carbides mostly at the grain boundary as shown in figure 4.6. The chemical composition varies between the laves and delta phases. Laves phases consist of silicon around 0.33 at%, while delta phases have a lower amount of niobium 19.58 at% and do not contain any silicon as shown in table 4.2. The presence of delta phase is more dominant in the case of No-3 sample compared to No-2. The microstructure of the matrix is composed of a gamma phase, with a uniform distribution of both gamma prime and gamma double prime phases. The laves and delta phase are present at the grain boundary and triple point after the heat treatment process. Furthermore, along the grain boundaries is a precipitation of Nb-rich carbides, which extends into the bulk but few amounts. These carbides were observed in the initial stages of heat treatment.

Table 4.2 Atomic percentage of each element in the EDS identified phases.

Phase	Ni	Nb	Fe	Cr	Ti	Si
laves	31,54	30,66	15,24	16,21	6,02	0,33
Delta	38,02	19,58	17,67	19,9	4,82	

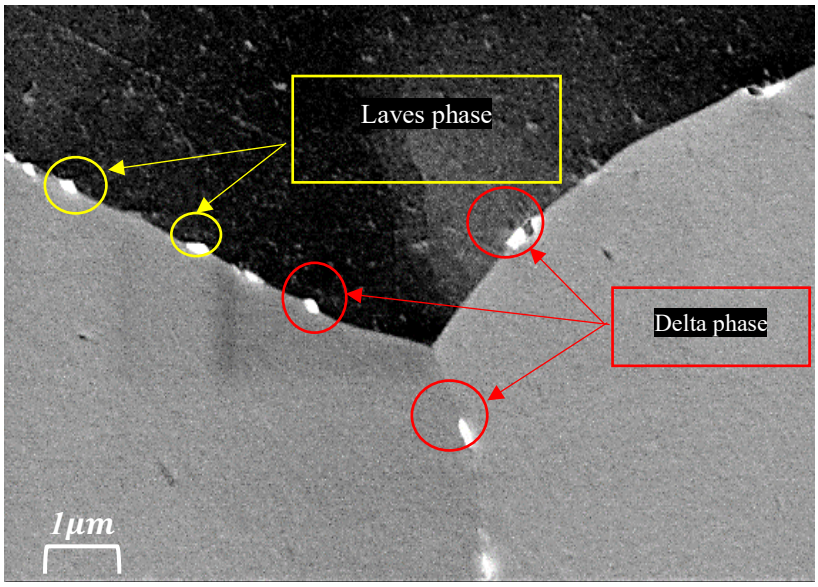

Figure 4.6 Shows the specimen No-3 EDS point analysis after heat treatment.

4.3.2 Samples deformed at high strain rate.

The double aged samples deformed at RT, 650, 750°C with high strain rate of $10^{-1}s^{-1}$ and analyzed the deformation behavior in terms of EBSD KAM analysis and fracture surface analysis with SEM technique. The EBSD KAM analysis used to understand the strain distribution over the grain, grain boundary and along the precipitate. Fracture analysis can provide the fracture behavior, which can determine whether the sample fractured with brittle or ductile. This analysis can provide solid explanation about the loss of ductility in correlation with mechanical stress strain plots.

Deformation analysis with EBSD KAM and ECCI

Figure 4.7 (a) shows the deformation analysis results obtained through EBSD and ECCI methods. The findings indicated that the material deformed at different temperatures and strain rates, leading to distinct deformation behaviors. The analysis confirmed the occurrence of cross-slip deformation behavior. Specifically, in Figures 4.6 (a) and (b), the ECCI analysis revealed the activation of cross slip. On the other hand, figure 4.6 (c) showed slip deformation with higher dislocation concentration observed both within the grain and along the grain boundaries. The EBSD analysis also demonstrated a more homogenized strain distribution in figure 4.6 (c), resulting in superior elongation properties compared to the other two cases.

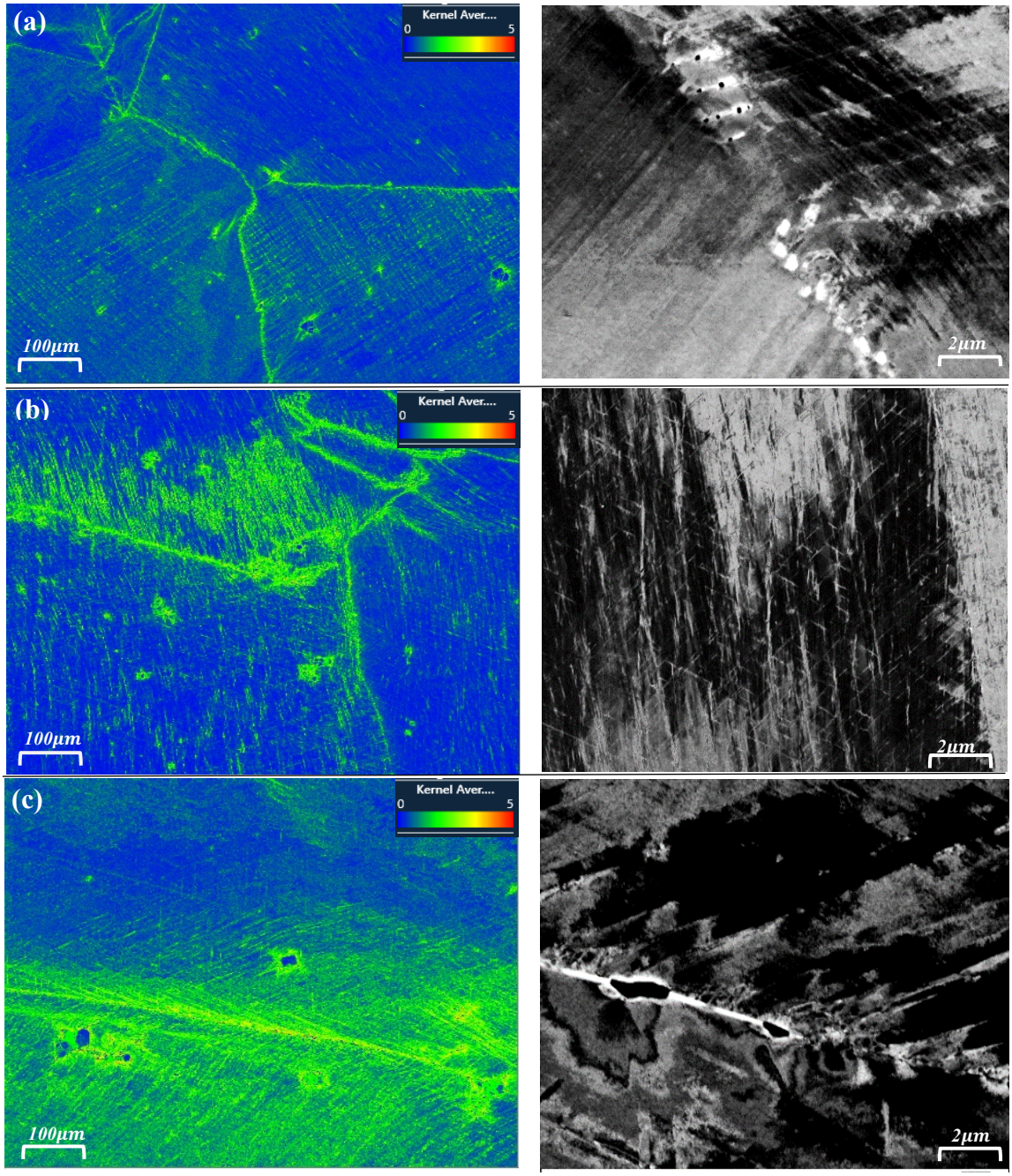

Figure 4.7 shows EBSD KAM & ECCI analysis of samples deformed (a) Room temperature strain rate - $10^{-1}s^{-1}$, (b) 650°C $10^{-1}s^{-1}$, (c) 750°C $10^{-1}s^{-1}$.

Fracture analysis

The figure 4.8(a) illustrates the fractography of the deformed specimen subjected to deformation at room temperature with high strain rate $10^{-1}s^{-1}$. It is revealing a fractured nature characterized by enhanced ductility, evident from the presence of dimples, with only a few intergranular cracks observed. Figure 4.8(b) illustrates the overall fracture surface of specimens evaluated under uniaxial tensile with $10^{-1}s^{-1}$at 650°C. The fracture surface exhibits non equiaxed dimples, indicating a ductile trans granular fracture mode. Additionally, discrete voids can be observed on the surface. The surface analysis reveals a mixed structure consisting of equiaxed dimples and shallow dimples along the shear regions and it indicates trans granular ductile fracture mode. But the presence of smooth facet is indicating the absence of ductile behaviour at that area and ductile to brittle transition zone. Presence of intergranular crack along with dimples make it combination of brittle ductile fracture behaviour. Figure 4.8(c) illustrates the overall fracture surface of specimens subjected to uniaxial tensile testing at 750°C with strain rate of $10^{-1}s^{-1}$.Further analysis reveals mixed structure on the fracture surface, characterized by the presence of both equiaxed dimples and shallow dimples along the shear regions. This observation strongly agreed for existence of trans granular ductile fracture mode.

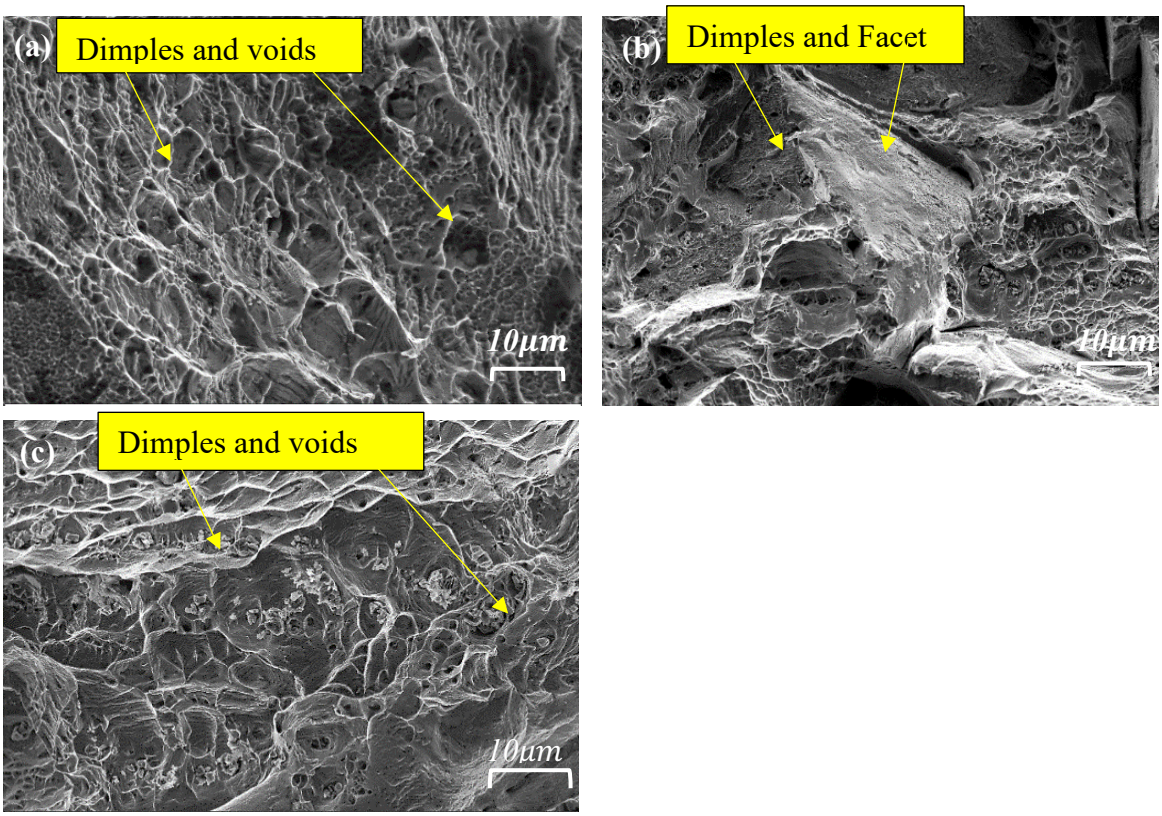

Figure 4.8 shows the fractography of samples deformed at (a) Room temperature strain rate - $10^{-1}s^{-1}$, (b) 650°C $10^{-1}s^{-1}$, (c) 750°C $10^{-1}s^{-1}$

4.3.3 Samples deformed at low strain rate.

The samples deformed at RT, 650°C, 750°C with high strain rate of $10^{-4}s^{-1}$ for analyzing the difference in deformation analysis in terms of strain rate. It was observed that strain rate significantly affected the deformation behavior, particularly at high temperature.

Figure 4.9 (a) ECCI image that provides strong evidence of cross-slip activation as the dominant deformation behaviour in the material. The presence of dislocations and the activation of slip mechanisms significantly contribute to enhancing the strength and elongation of material. Although the ECCI image does not provide any dislocation and precipitate interaction that play a role in the strengthening effect. But EBSD images combined with KAM analysis has shown a homogeneous strain distribution within the matrix. This suggests that dislocations interact with specific precipitates present in the matrix [15]. Both figure 4.9 (b), (c) ECCI images showing very few slips deformation activated and it is not contributing the complete plastic deformation. This is strongly supported by the EBSD KAM analysis reveals the strain distribution is only focus on grain boundary and a few noticeable strain distributions occurring within the grains themselves. The analysis of the microstructure shows a decreasing trend in slip deformation as temperature increases. This suggests that strain rate alone does not significantly affect material properties, but temperature can have an influence on them.

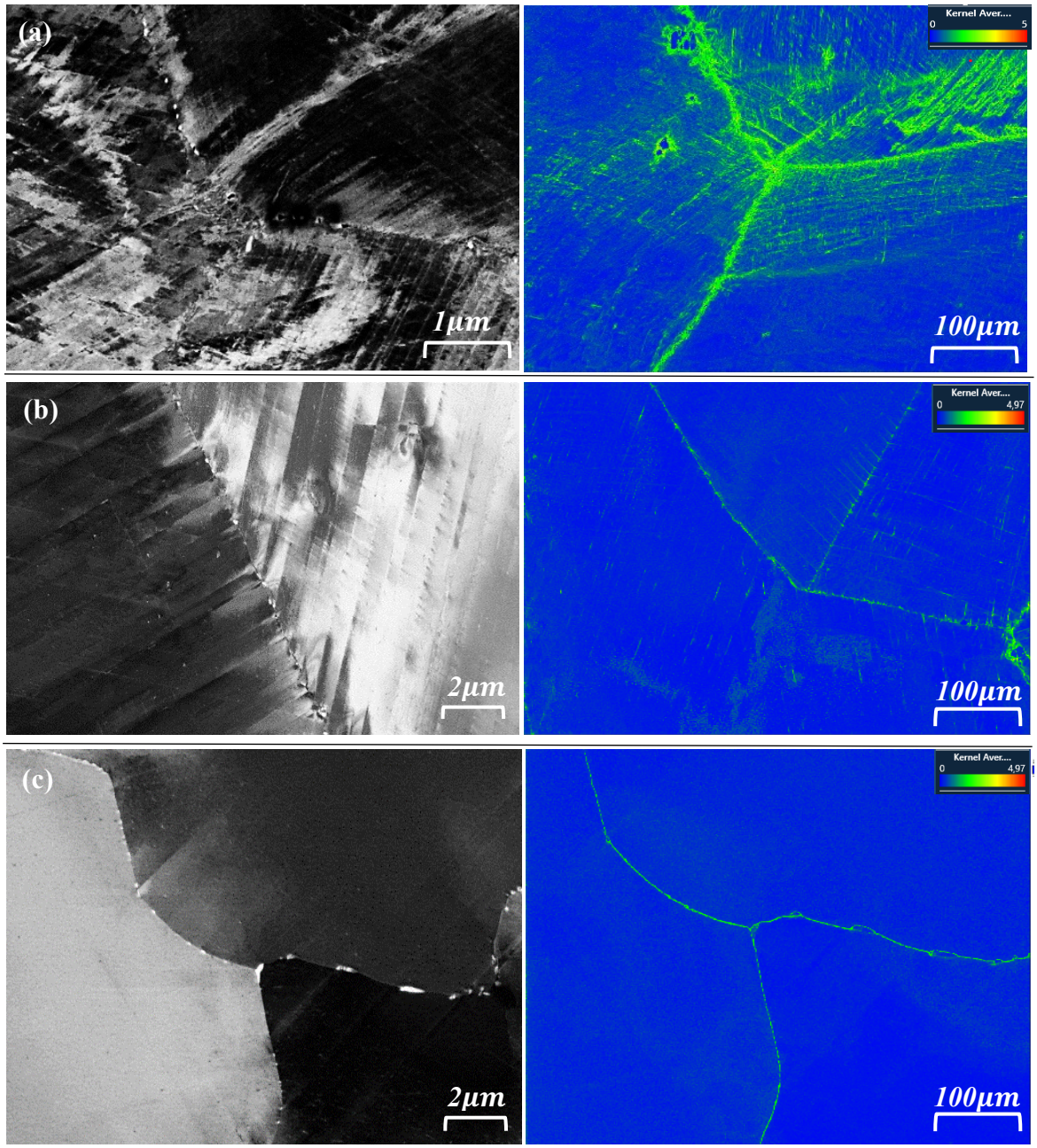

Figure 4.9 shows the EBSD KAM & ECCI analysis of samples deformed (a) Room temperature strain rate - $10^{-4}s^{-1}$, (b) 650°C $10^{-4}s^{-1}$, (c) 750°C $10^{-4}s^{-1}$.

Fracture analysis

Figure 4.10 (a) displays a surface with a mixed structure characterized by the presence of equiaxed and shallow dimples along the shear regions, suggesting trans granular ductile fracture mode. Additionally, few intergranular cracks observed on the fracture surface, indicating a combination of both trans granular and intergranular fracture modes as the cause of failure. The presence of shallow dimples also suggests that the material displays ductile behavior. From the figure 4.10 (b) shows the dimples and smooth facet with intergranular cracks. As the stress strain diagram, sample shows the embrittlement behaviour and fracture surface is also agreement with brittle behaviour. However, in the case of sample deformed at 750°C with strain rate of $10^{-4}s^{-1}$ shows completely loss the elongation led to the embrittlement behaviour. From the fracture surface it is very clear that smooth facet and intergranular cracks as mentioned in figure 4.10 (c) indicating only brittle characteristics of sample with loss of ductility.

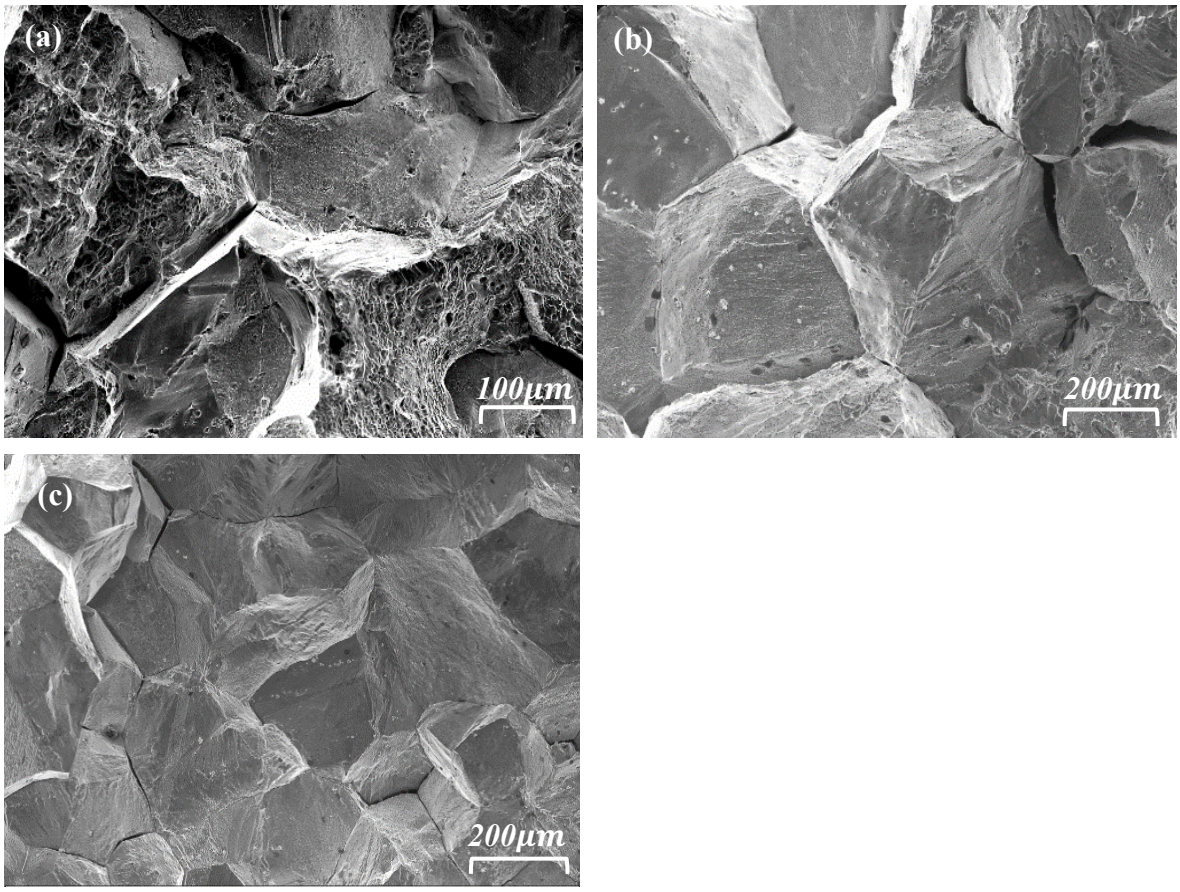

Figure 4.10 shows the fractography of samples deformed at (a) Room temperature with strain rate - $10^{-4}s^{-1}$, (b) 650°C $10^{-4}s^{-1}$, (c) 750°C $10^{-4}s^{-1}$

4.4 Microstructure analysis and evaluation for material No 2

The sample No- 2 is taken from the bar that hot rolled condition and heat treatments solution annealing and double aging are performed. The homogenization process was not performed to analyse the laves phase effect during material deformation.

4.4.2 Sample deformed at high strain rate.

In figure 4.11 (a) & (b), the ECCI images provide the evidence of cross slip activation as the dominant deformation behaviour. The EBSD-KAM image reveals more homogeneous strain distribution within the matrix. This suggests the interaction of dislocations with some precipitates within the matrix. The presence of dislocations and slip plays a critical role in enhancing the strength and elongation of the material and it effect flow stress characteristics. This indicates a uniform strain distribution throughout these regions and presence of small angle grain boundaries from EBSD KAM analysis, indicating a consistent and uniform slip deformation behaviour [15]. This type of strengthening mechanism is the main reason behind good elongation properties with samples deformed at room temperature as well as the 650°C with high strain rates. However, the sample has shown embrittlement behaviour upon deformed at 750°C and it is confirming from figure 4.11(c) ECCI image that provides evidence of slip activation as the dominant deformation behavior. However, the observed slip volume is small, and there are no signs of cross-slip activation. In this scenario, the dislocations primarily interact with slip but do not play a significant role in the plastic deformation mechanism. As a result, when loaded, the material does not receive enough support from plastic deformation mechanisms such as slip due to the limited activated volume. This can potentially cause sudden intergranular crack formation. Figure 4.11 (c) shows EBSD-KAM images that exhibit a localized concentration of strain along the grain boundaries and within precipitates. This suggests an interaction between dislocations and specific precipitates in the bulk material. The observed strain distribution is limited to these areas, indicating a heterogeneous distribution throughout these regions and inconsistent deformation behavior in other parts of the matrix.

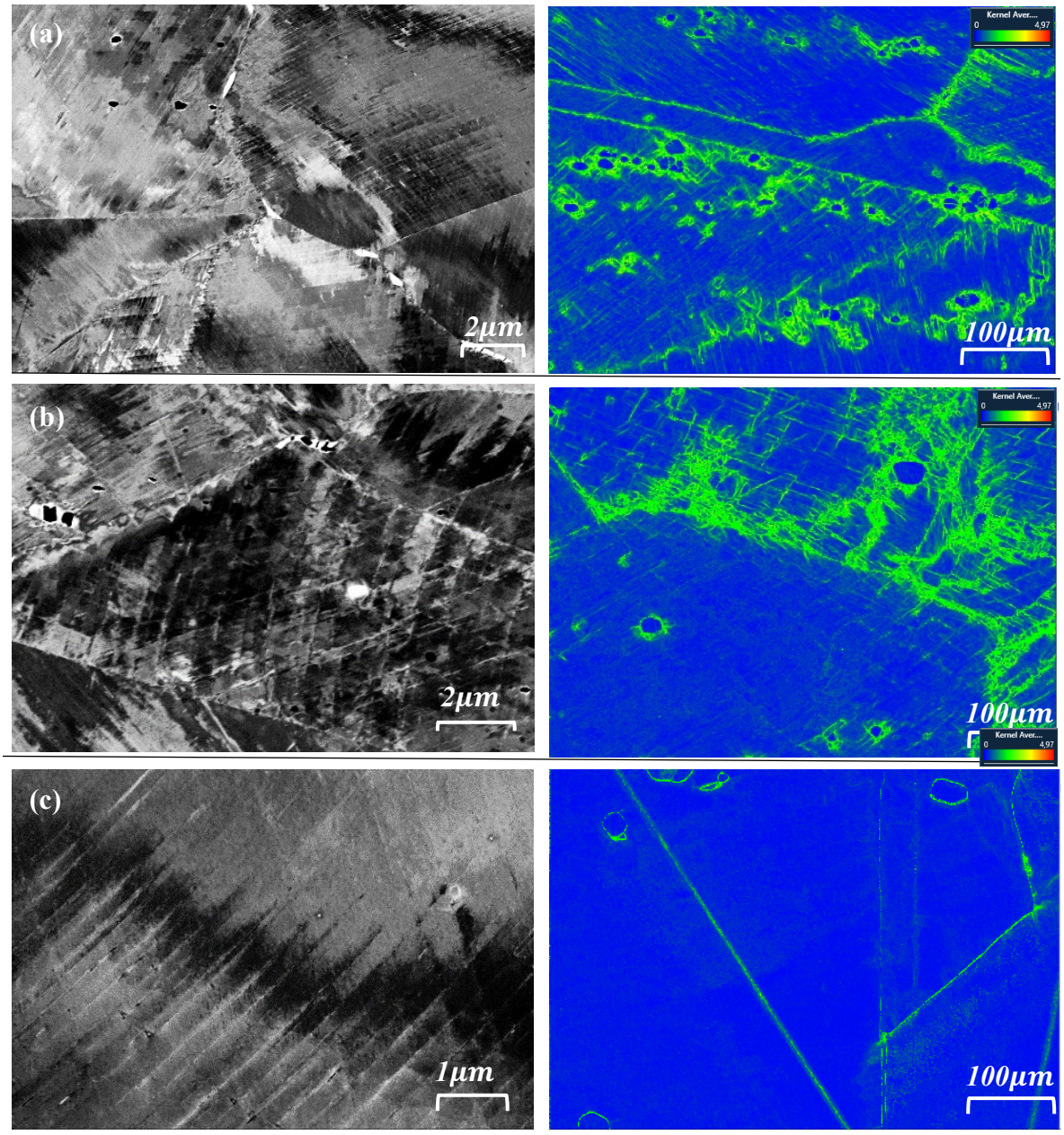

Figure 4.6 shows the EBSD KAM & ECCI analysis of samples deformed (a) Room temperature strain rate - $10^{-2}s^{-1}$, (b) 650°C $10^{-2}s^{-1}$, (c) 750°C $10^{-2}s^{-1}$.

Fracture analysis

The Figure 4.12 (a) & (b) fracture surfaces have shown uniform distribution of the equiaxed dimples along the shear regions, indicating a trans granular ductile fracture mode. The intergranular cracks are visible on the fracture surface, indicating a combination of both trans granular and intergranular fracture modes as the cause of the final failure. As the stress strain diagram also shows the ductile behaviour and fracture surface is also supported this observation. However, in the case of sample deformed at 750°C with strain rate of $10^{-2}s^{-1}$ shows completely loss the elongation. From the fracture surface, it is very clear that dimples with intergranular cracks as mentioned in figure 4.12(c) indicating brittle characteristics of sample with loss of ductility.

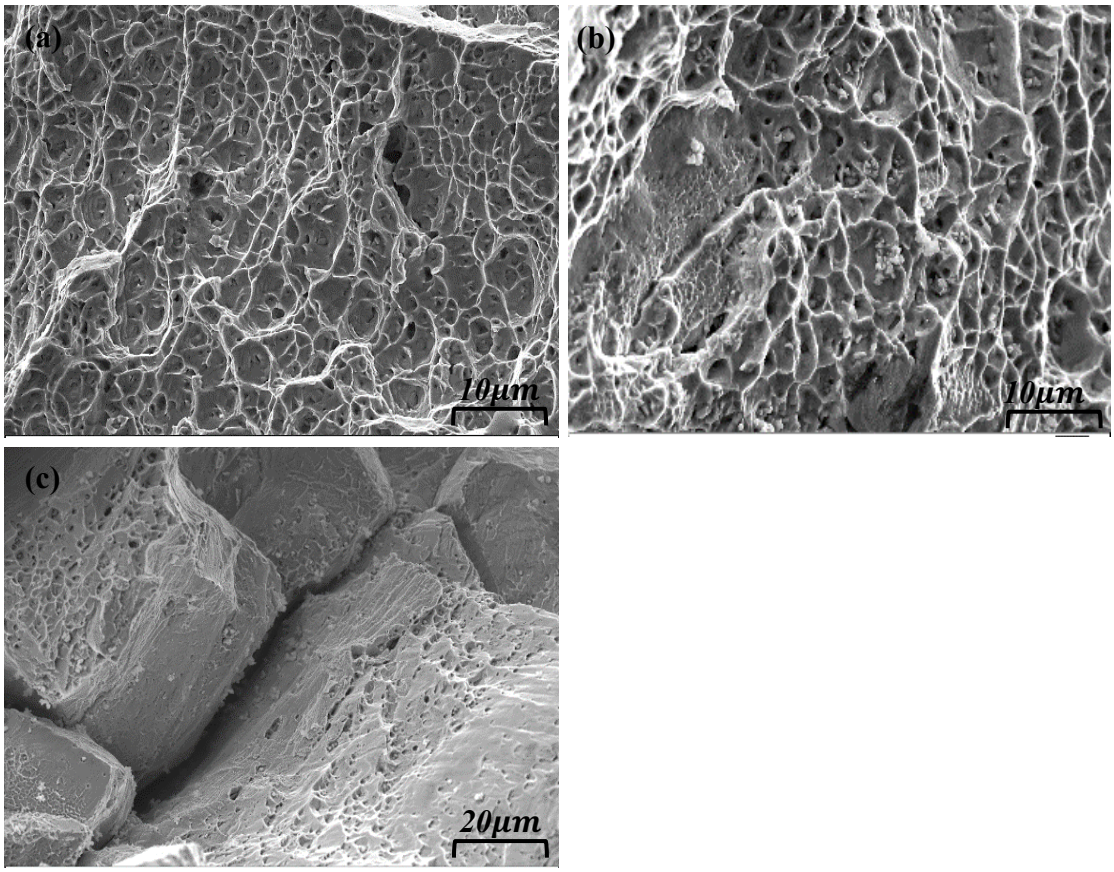

Figure 4.7 shows the fractography of samples deformed at (a) Room temperature strain rate - $10^{-2}s^{-1}$, (b) 650°C $10^{-2}s^{-1}$, (c) 750°C $10^{-2}s^{-1}$.

4.4.3 Sample deformed at low strain rate

The figures 4.13 (a) & (b) illustrate ECCI images providing evidence of a relatively low volume of slip and increasing temperature the plastic deformation is completely disappear and loss of elonagtion. The EBSD KAM analysis of both cases are showing that completely no more strain distribution at grain matrix and its internsity is lowered upon the incresing temperature is the main reason along with strain rate.This suggests that dislocations interctions arrested somehow in the bulk material and it became brittle. While the strain distribution is observed at the grain boundaries and precipitates, there is minimal strain distribution along slip lines within the matrix. This intriguing observation is followed by embrittlement in the matrix. Overall, these findings suggest a heterogeneous strain distribution throughout these regions, implying inconsistent deformation behaviour [15].

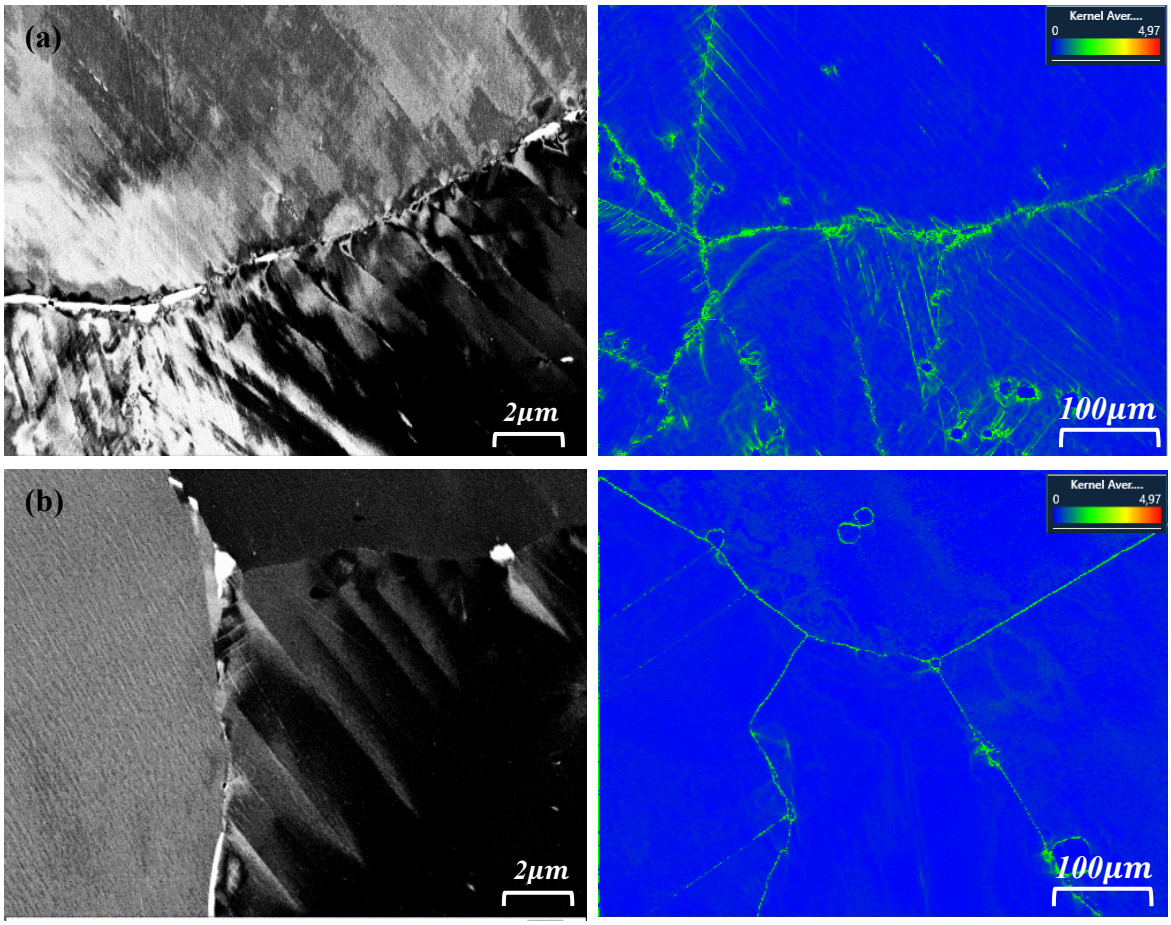

Figure 4.8 shows the EBSD KAM & ECCI analysis of samples deformed at (a) 750°C $10^{-3}s^{-1}$, (c) 750°C $10^{-4}s^{-1}$.

Fracture analysis

The figure 4.14 (a) and (b) depict the fracture surfaces of specimens tested under uniaxial tensile conditions at 750°C with a strain rate of $10^{-4}s^{-1}$& $10^{-3}s^{-1}$. The fracture surfaces exhibit a prominent presence of intergranular cracks along with dimples. This indicates that the sample exhibits embrittlement behaviour and confirmed by the stress-strain plot. An in-depth examination of the fracture surface provides additional indications of intergranular cracking with the presence of dimples. This observation suggests the occurrence of localized stress concentration at the grain boundaries, which could be influenced by various factors. The intergranular cracks and embrittlement phenomenon can be attributed to multiple reasons, including precipitate (laves phase) growth and the formation of oxidation-assisted intragranular cracks at 650 & 750°C.

However, Alloy 718 is strengthened by the precipitation strengthening mechanism and some gamma prime and gamma double prime are present at bulk, but no participation for strengthen mechanism ended up with intergranular crack and loss of ductility as seen in the literature studies. The strain distribution that is absence at the matrix phase and only at grain boundaries may lead to quick initiation of cracks. The possibilities of forming Cr oxides film at this temperature formed at grain boundary further quick chances of crack initiation and propagation may happen.

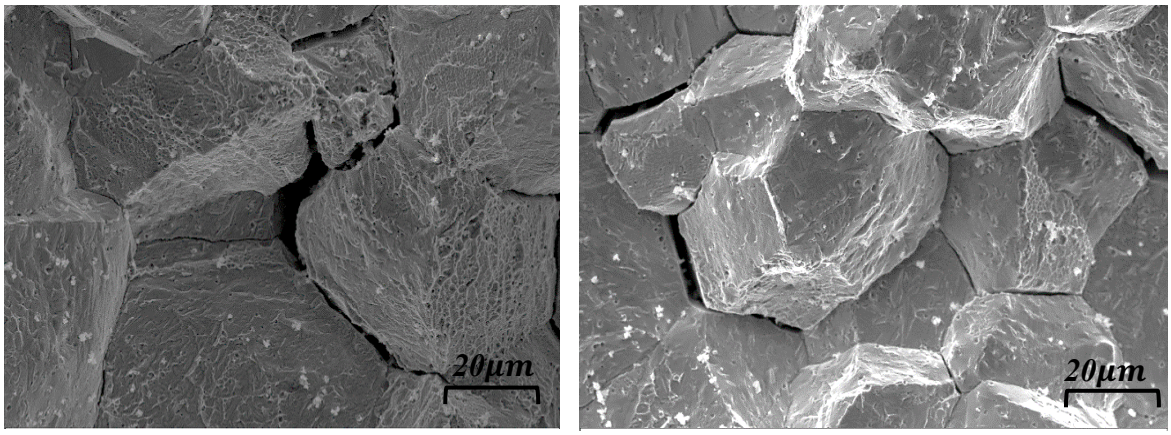

Figure 4.9 shows the fractography of samples deformed at (a) 750°C $10^{-3}s^{-1}$, (c) 750°C $10^{-4}s^{-1}$.

4.5 General discussion

This chapter will discuss about the different type of factors affect the embrittlement behaviour of IN-718.The concept of strain rate effect, temperature effect and heat treatment effect, Oxidation and dynamic strain aging discuss more comparative manner.

4.5.1 Strain rate and temperature effect

Strain rate has considerable effect on loss of ductility only with increasing temperature. The sample evaluated at 750°C with a high strain rate $10^{-1}s^{-1}$exhibited good elongation and displayed characteristics indicative of a ductile fracture mode in figure 4.15. Dimples and micro voids in the SEM fractography analysis support this. However, it noted that in certain regions, few intergranular fractures were noted. This intergranular fracture could be attributed to the fast elongation rate during the test, which may have induced localized stress concentrations and facilitated crack propagation along grain boundaries.

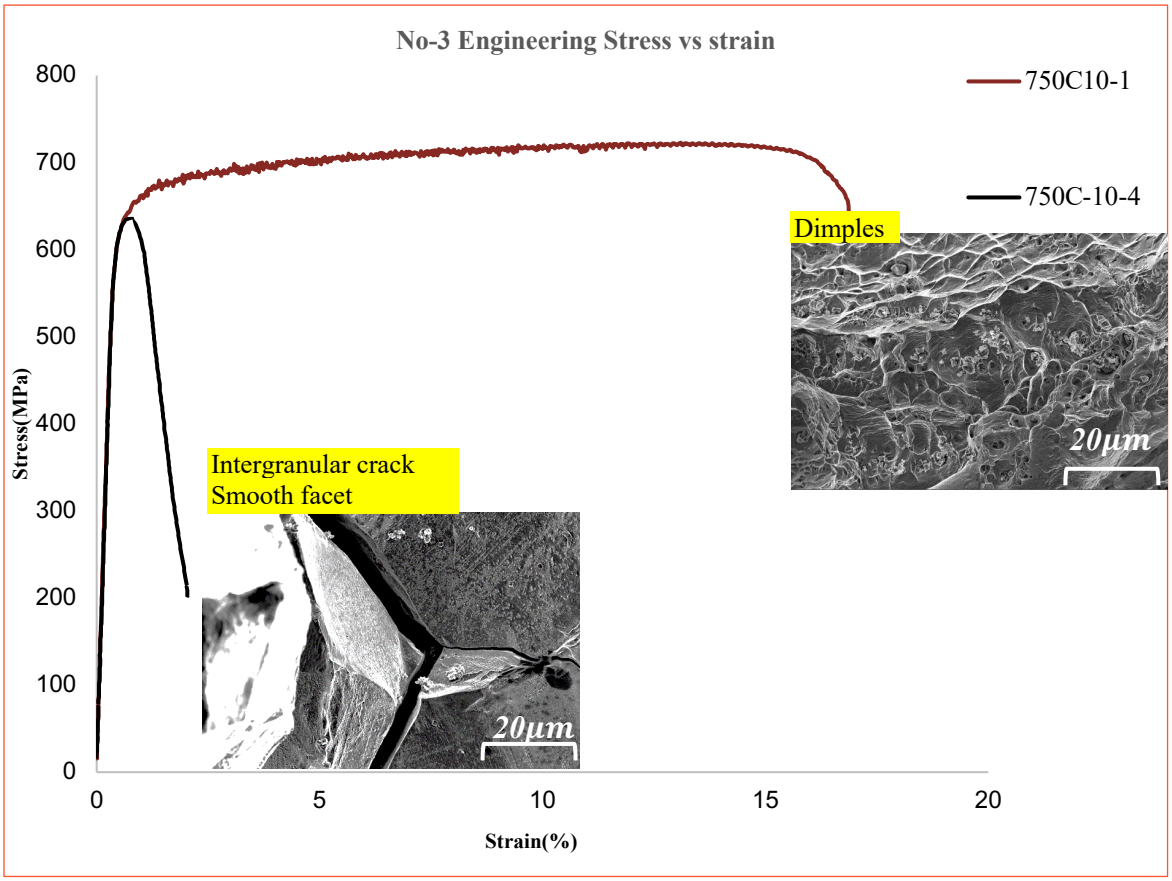

Figure 4.10 show the engineering stress vs strain plot along with fractographic view of fracture at 750℃ strain rate 10^{-1} & 10^{-4}

Figure 4.16 shows more volume percentage of LAGB analysed by EBSD BC for sample deformed at high strain rate at 750℃ . But HAGB is more dominant in sample deformed at low strain rate at intermediate temperature 750℃. The LAGB is the sign of sample deformed plastically and provides good elongation.

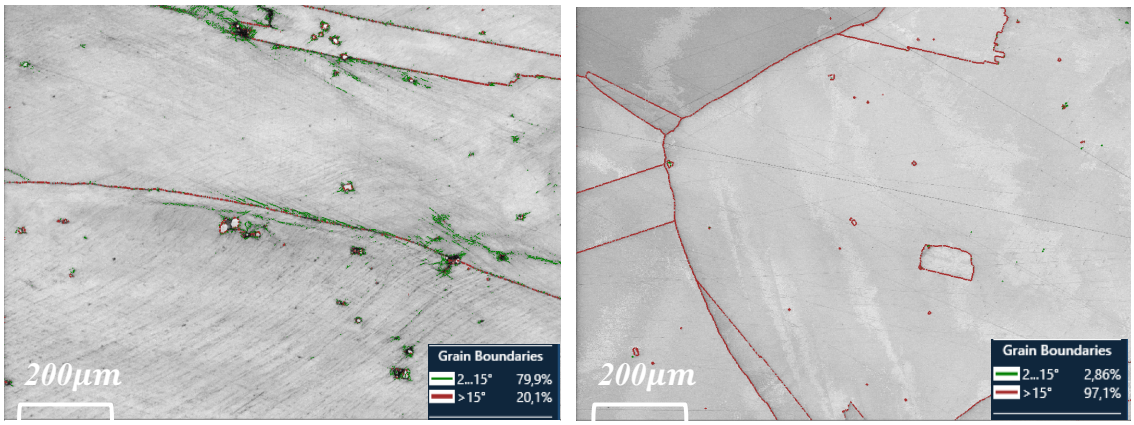

Figure 4.11 shows the EBSD BC images with LAGB (2-15°) & HAGB (>15°) of samples deformed at 750℃ strain rate 10^{-1} & 10^{-4} respectively.

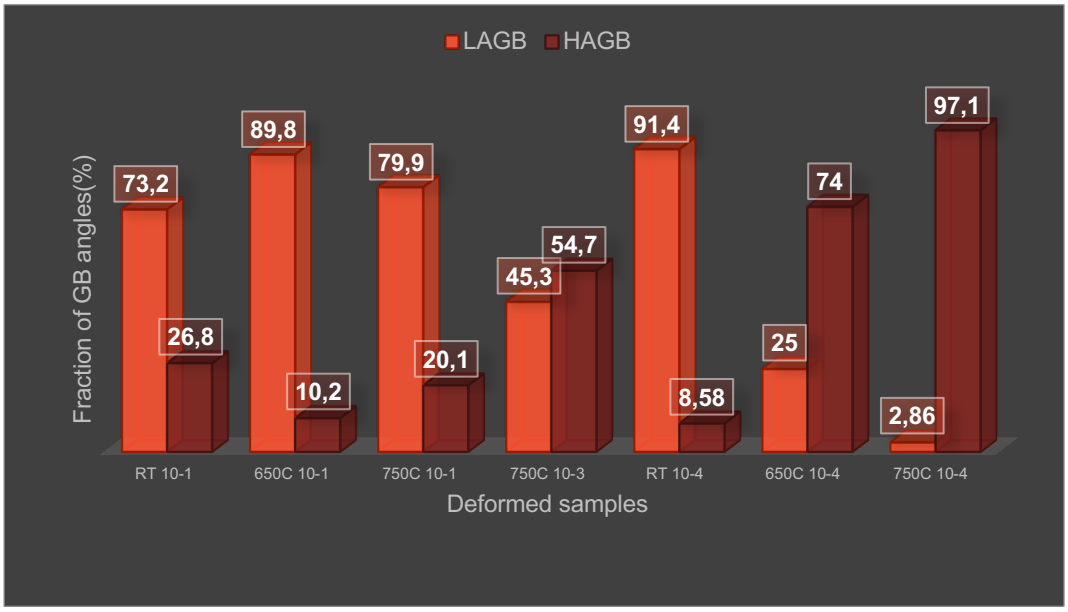

Figure 4.12 Shows the graphical visualization of fraction of LAGB & HAGB of sample No-3.

4.5.2 Role of oxidation assisted intergranular crack -Temperature Effect

In the case of samples deformed at high temperature, oxidation is the prime factor because the cracks are intergranular and originate inside the material, and starting from the surface is considered an important observation. This study focuses on an important aspect of the research, the formation potential of chromium oxide at grain boundaries and boost up crack initiation and propagation. This observation is consistent with previous studies conducted by researchers investigating nickel-based superalloys [16].

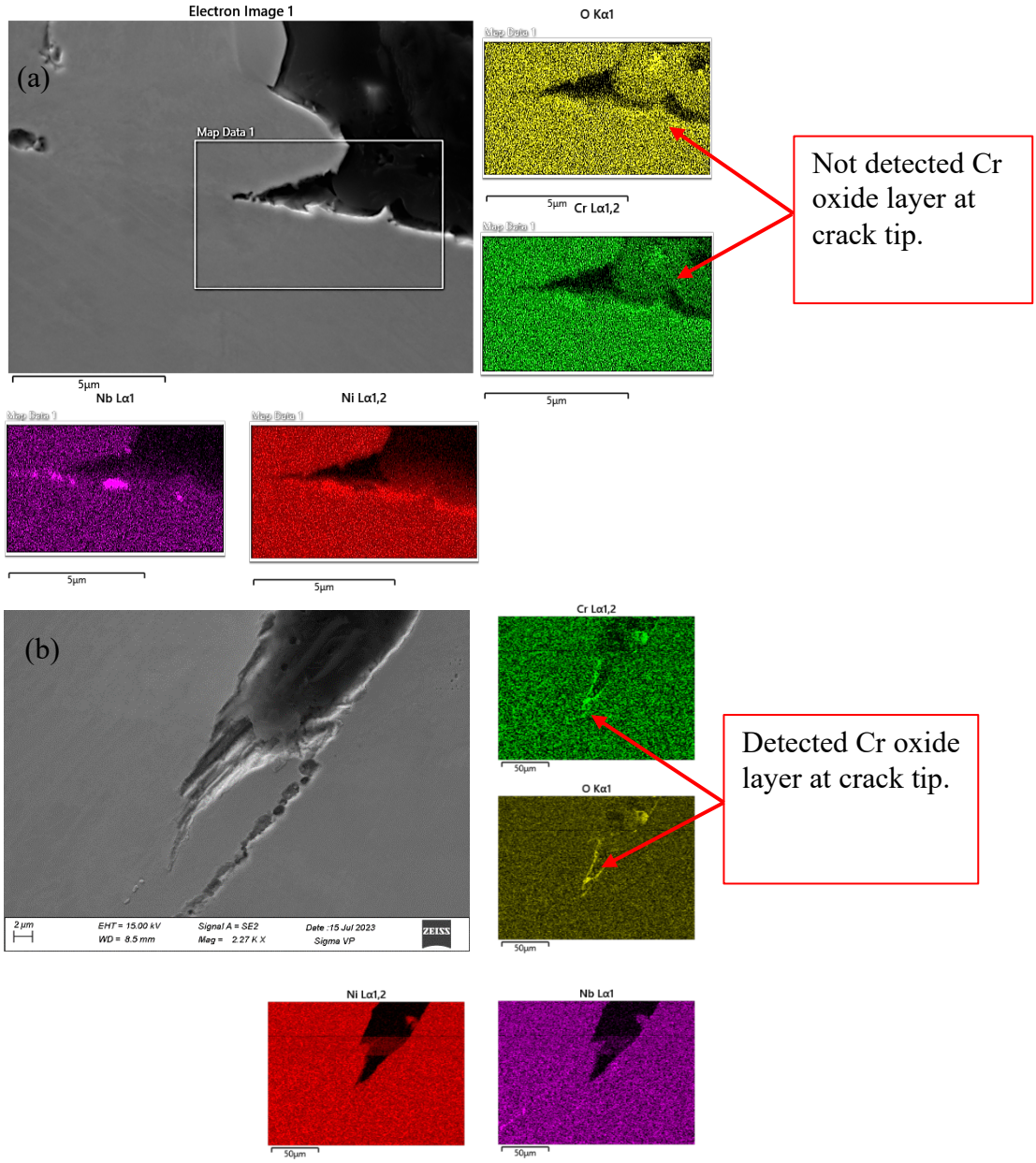

Figure 4.18 shows EDS map analysis of sample deformed at (a) RT (b) 750℃

Figure 4. 13 shows the EDX map detect chromium rich oxide at crack tip of sample deformed at 750℃ in figure 4.18(b). At same time it did not identify sample deformed at room temperature figure 4.18 (a). The Figure 4.14 illustrates two conditions where samples deformed at room temperature and 750℃. It is evident that the presence of Cr-rich oxide detected in the sample deformed at 750℃. But the sample deformed at RT, Cr-rich oxide not detected. The intergranular crack observed to propagate from the side surface of the sample suggests a higher probability of oxidation-assisted intergranular cracking during deformation at elevated temperatures [16]. The evidence obtained from EDX, EBSD, and fractography supports this observation. The strain rate also plays a significant role in this phenomenon. At higher strain rates, the exposure time during the tensile test is short, usually just few seconds. In contrast, at lower strain rates, the temperature has more time to interact with the material, leading to increased oxidation, which results in reduced elongation and embrittlement.

Figure 4.19 shows a noticeable presence of intergranular cracks at the surface. In Figure 4.18, it is evident that the Cr-rich oxide concentrated at the tip of the crack. These findings strongly support intergranular cracking, as crack propagation from the surface and the presence of the Cr-rich oxide layer contribute to this phenomenon.

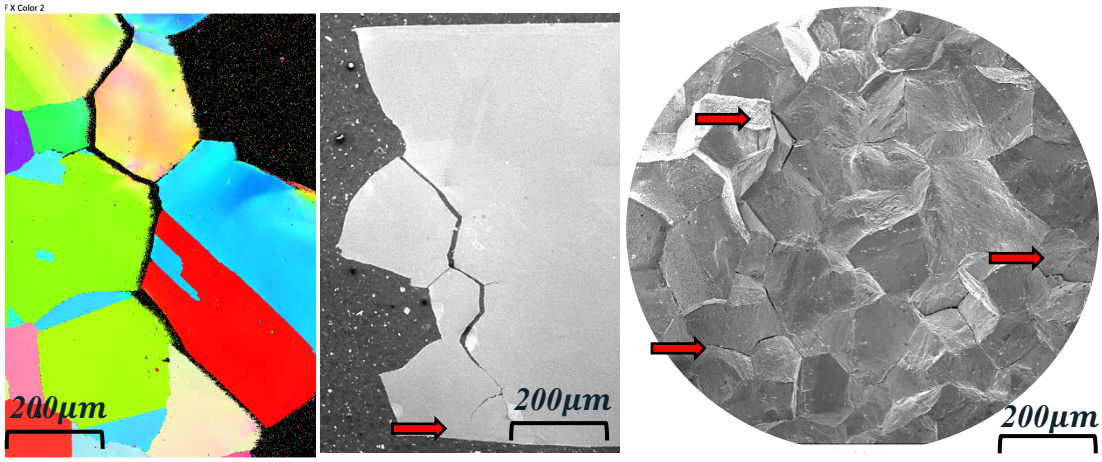

Figure 4.19 shows EBSD, SEM-SE & Fractography images crack behavior of sample deformed at 750℃ with low strain rate $10^{-4}s^{-1}$. Cracks are more observed at surface of specimen.

4.5.3 Effect of precipitate and dislocation characteristics (DSA)

Figure 4.20, along with other analyses has already confirmed the presence of an intergranular crack. The focus of research is examining the influence of Laves phase and strain distribution in GB and matrix with high strain rate and low strain rate strain rate at 750°C was analysed. As shown in Figure 4.20(a), it noted that the crack propagated through both grain boundaries and precipitate. The ECCI image displays a clear observation of stress concentration focused on the precipitate and matrix, indicating high strain rate deformation. This is consistent with previous discussions where dislocation interaction mentioned in section (4.4.1). Additionally, the presence of low-angle grain boundaries suggests that plastic deformation has occurred. At low strain rates, no stress concentration and very few plastic deformations occur that indicate dislocations to become trapped within the material. This phenomenon is attributed to specific factors that restrict the movement of dislocations.

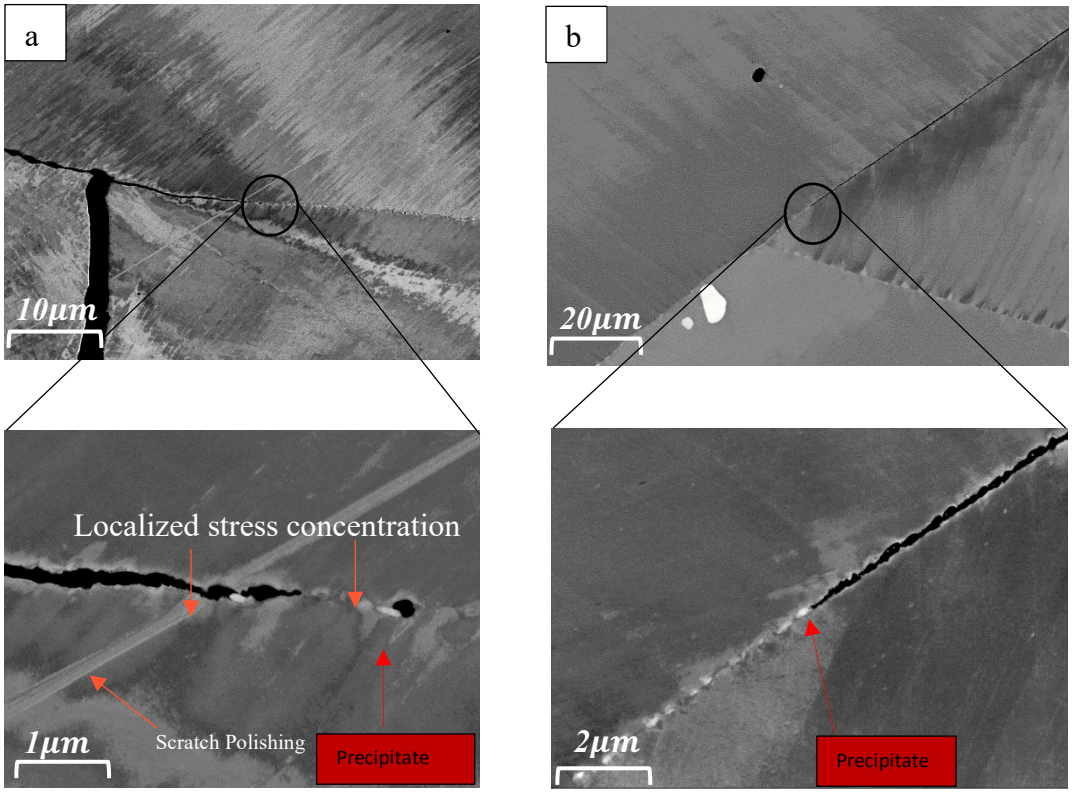

Figure 4.20 shows the crack propagation characteristics comparison of low strain rate and high strain rate sample No-3.

Kaisheng Ming [17] attributed to the chance of rapid nano-segregation of essential elements such as Ni, Cr, and Mn into GBs. This phenomenon leads to reduced cohesion within these boundaries and promotes crack formation along them. A potential solution proposed by the authors involves employing a strategy called GB segregation engineering. By actively promoting ting fast migration of principal elements away from GBs towards preexisting secondary phases that are rich in chromium, it is possible to counteract the loss of ductility.

This study also shows the incoherent behavior of laves phases at grain boundary may cause crack initiation area and due to no participation of dislocation activity can increase the intensity of crack propagation [15]. Additionally, at low strain rate may increase time for dislocation trapped somewhere in matrix because of dynamic strain aging since the flow curve indicate C type of low strain after UTS region as mentioned in figure 4.21. C type curves are more prone to dynamic strain aging with loss of ductility as it is clear from all curves following loss of ductility showing C type and A+B type of serration behavior [18,19]. During dynamic strain aging, at intermediate temperatures, solute atoms dynamically cluster around migrating dislocations, forming Cottrell atmospheres due to accelerated mobility as observed in figure 2.7. These atmospheres impede dislocation migration, leading to reduced failure strain and decreased ductility. At the same time sample deformed at high strain rate, curve is showing smooth A type make different from low strain rate with C type serration patterns. C type curve meaning is that locking and unlocking dislocation motion by solute atoms. In short deformation at low strain rate more prone to dynamic strain aging mechanism means locking only since the curve shows the deviation only downward not upward in figure highlighted below.

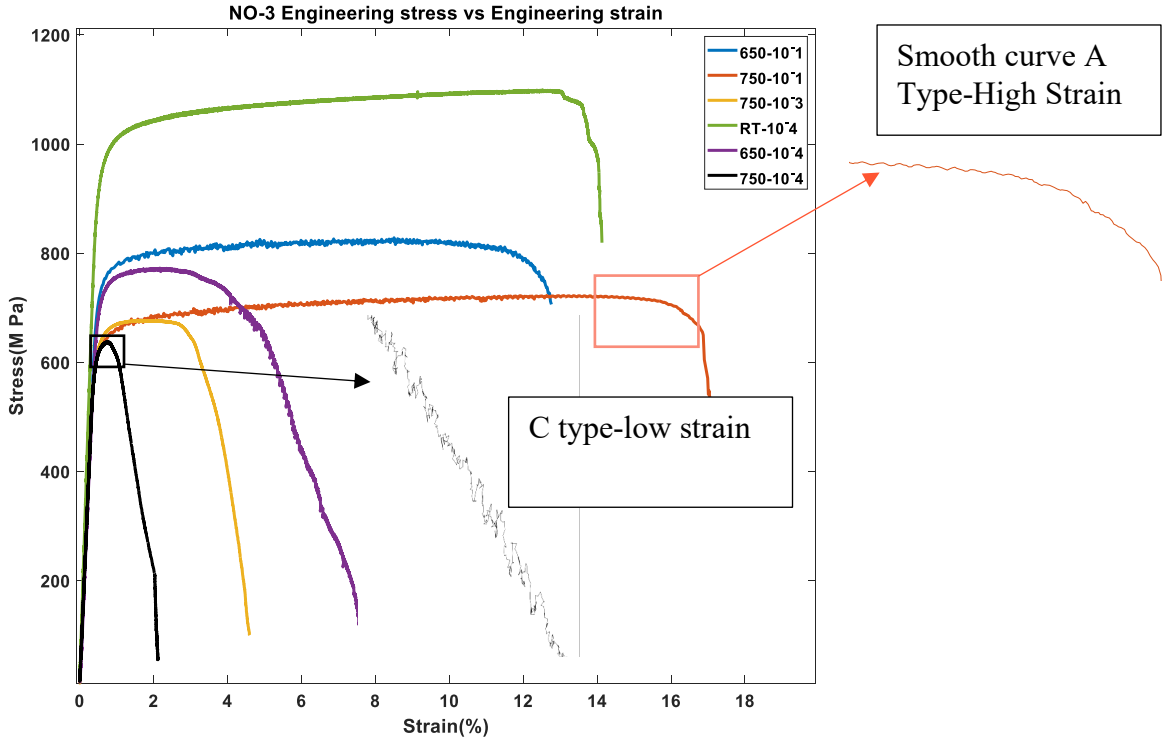

Figure 4.21 shows the stress strain curve with dynamic strain behaviors.

Figure 4.20 confirms the absence of dislocation motion based on ECCI microstructure analysis, and it is agreement with DSA behaviour mentioned in figure 4.21. Both observations strongly indicate that dislocations trapped somewhere in matrix or Grain boundary.

5 CONCLUSIONS

Alloy 718 exhibits intermediate temperature embrittlement (ITE) during tensile testing at an intermediate temperature range. The presence of the Laves phase at the grain boundaries and oxidation assisted intergranular cracks are prime factors for contributing intermediate temperature embrittlement. However, it observed that increasing the strain rate can help to minimize the ITE in Alloy 718.

1) The study reveals the presence of an intergranular mechanism facilitated by oxidation. A longer period of exposure at low strain rate increases the time of exposure compared to samples exposed to high strain rates. the formation of an oxide layer is dependent on the duration of exposure.
2) Dynamic strain aging can significantly influence the serrations present in stress-strain curves after the yield point, particularly for samples deformed at low strain rates. The presence of DSA and its associated serrations can be attributed to the trapping of dislocations within the material structure. At low strain rates, there is sufficient time for these dislocations to interact with solute atoms and accumulate within specific regions, leading to more pronounced serrated flow behaviour.
3) The exact mechanisms underlying ITE in this alloy are not yet fully understood. However, several proposed mechanisms shed light on this phenomenon. A higher strain rate promotes more homogeneous deformation in the matrix, reduces the dynamic strain effect, and limits the growth of precipitates, all of which contribute to improved elongation and reduced embrittlement.

Further research is essential to gain a comprehensive understanding of the mechanisms responsible for ITE in Alloy 718. This knowledge will be crucial in developing strategies to mitigate ITE and optimize the mechanical properties of the alloy for various applications.

6 REFERENCE

1) Zheng, L., Schmitz, G., Meng, Y., Chellali, R., & Schlesiger, R. (2012). Mechanism of Intermediate Temperature Embrittlement of Ni and Ni-based Superalloys. Materials Science and Technology, 28(9-10), 1053-1060. http://dx.doi.org/10.1080/10408436.2011.613492
2) Moretti, M. A. (Year). Microstructure and property models of alloy 718 applicable for simulation of manufacturing processes (Licentiate thesis). Lulea University of Technology, Lulea, Sweden.
3) Azadian, S. (2004). Aspects of Precipitation in the Alloy Inconel 718 (Doctoral thesis, No. 2004:20). Lulea University of Technology, Lulea, Sweden.
4) R. R. Jensen and J. K. Tien, Temperature and strain rate dependence of stress-strain behavior in a nickel-base superalloy, Metall.Trans. A, 16, 1049 (1985)
5) P. D. Merica and R. G. Waltenberg, The malleability of Ni, Trans AIME, 71, 709 (1925)
6) A. K. Roy, J. Pal, and C. Mukhopadhyay, Dynamic strain aging of an austenitic superalloy—temperature and strain rate effects, Mater. Sci. Eng. A, 474, 363 (2008).
7) R. H. Bricknell and D. A. Woodford, The embrittlement of nickel following high temperature air exposure, Metall. Trans. A, 12, 425 (1981)
8) Kushan, M. C., Uzgur, S. C., Uzunonat, Y., & Diltemiz, F. (Year). ALLVAC 718 Plus™ Superalloy for Aircraft Engine Applications. Journal Name, 2012
9) Chamanfar, A., Sarrat, L., Jahazi, M., Asadi, M., Weck, A., & Koul, A. K. (2013). Microstructural characteristics of forged and heat-treated Inconel-718 disks. Materials & Design, 52, 791-800. DOI: 10.1016/j.matdes.2013.06.004 http://dx.doi.org/10.1016/j.matdes.2013.06.004
10) Joseph R Davis. Tensile testing. ASM international, 2004 (cit. on p. 23).
11) Dieter, G. E. Jr. (Year). Mechanical Metallurgy. Philadelphia, PA: Drexel Institute of Technology Dieter, G. E. Jr. (Year). Mechanical Metallurgy. Philadelphia, PA: Drexel Institute of Technology.
12) T. Maitland och S. Sitzman," Electron Backscatter Diffraction (EBSD) Technique and Materials Characterization Examples,"Scanning Microscopy for Nanotechnology, Springer, 2007, pp. 41-75.
13) Gutierrez-Urrutia, I., Zaefferer, S., & Raabe, D. (2013). Coupling of Electron Channeling with EBSD: Toward the Quantitative Characterization of Deformation Structures in the SEM. JOM (Journal of Minerals, Metals, and Materials), 65(9). DOI: 10.1007/s11837-013-0678-0.
14) Kalh, S., Rao, K. B. S., Halford, G. R., & McGaw, M. A. (1994). Deformation and damage mechanisms in Inconel 718 superalloy. In E. A. Loria (Ed.), Superalloys

718, 625, 706 and Various Derivatives (pp. Page numbers). The Minerals, Metals & Materials Society. http://dx.doi.org/10.7449/1994/Superalloys_1994_593_606

15) Porter, D. A., & Easterling, K. E. (Year). Phase Transformations in Metals and Alloys (2nd ed.). Rautaruukki Oy Research Centre, Raahe, Finland: Exeter, UK.
16) Saravanan, K., Chakravadhanula, V.S.K., Manwatkar, S.K., Narayana Murty, S.V.S., & Ramesh Narayanan, P. (2020). Dynamic Strain Aging and Embrittlement Behavior of IN718 During High-Temperature Deformation.doi: https://doi.org/10.1007/s11661-020-05970-3
17) Ming, K., Li, L., Li, Z., Bi, X., & Wang, J. (Year). Grain boundary decohesion by nanoclustering Ni and Cr separately in CrMnFeCoNi high-entropy alloys. Science Advances 2019; 5: eaay0639
18) Saravanan, K., Chakravadhanula, V.S.K., Manwatkar, S.K., Narayana Murty, S.V.S., & Ramesh Narayanan, P. (2020). Dynamic Strain Aging and Embrittlement Behavior of IN718 During High-Temperature Deformation. The Minerals, Metals & Materials Society and ASM International.
19) Yamada, H.; Kami, T.; Ogasawara, N. Effects of Testing Temperature on the Serration Behavior of an Al–Zn–Mg–Cu Alloy with Natural and Artificial Aging in Sharp Indentation. *Metals* **2020**, *10*, 597. https://doi.org/10.3390/met10050597

PART -II

DEFORMATION BEHAVIOUR IN HIGH-MEDIUM ENTROPY ALLOYS

Abstract

The deformation behaviours of Fe-Ni-Cr-Mn-Mo high-medium entropy alloys were investigated at three different temperatures -196°C, room temperature, and 300°C. The study focused on understanding the effects of composition, entropy, and temperature on the deformation twinning behaviour through tensile testing and microstructure analysis using Electron Backscatter Diffraction and Electron Channelling Contrast Imaging The results revealed the presence of multi-order twinning, which explains the TWIP (Twinning-Induced Plasticity) mechanism. This research contributes to a deeper understanding of the deformation mechanisms in Fe-Ni-Cr-Mn-Mo high-medium entropy alloys, providing valuable insights for the development of advanced materials with enhanced mechanical properties.

Keywords: High entropy alloys, medium entropy alloys, tensile test, deformation, thermodynamics, EBSD, ECCI

Contents

Abbreviations

HEAs	High-entropy alloys
MEAs	Medium entropy alloys
VEC	valence-electron concentration
FCC	face-centred cubic
BCC	Body-centred cubic
RT	ROOM TEMPERATURE
BC	Band contrast
EBSD	Electron Backscatter Diffraction
SFE	Stacking fault Energy.
TWIP	Twinning Induced Plasticity
ΔHmix	Enthalpy of mixing
ECCI	Electron channelling contrast imaging
UTS	Ultimate tensile strength

1 INTRODUCTION

This chapter will provide background of the deformation behaviour of high entropy alloys with different temperature. The chapter will end with discussion of research objectives based on the studies and providing prime intention of the project.

1.1 Background

The concept of high entropy alloy was first introduced by J. W. Yeh and his colleagues in 2004 and proposed that such materials could exhibit novel properties due to their unique composition [1]. High entropy alloys are characterized by a complex microstructure that provides extra ordinary physical and mechanical properties such as high strength, ductility, and resistance to corrosion. These desirable attributes have led to widespread applications in aerospace, energy, and biomedical engineering. Ongoing research efforts aim to synthesize new compositions of high entropy alloys and gain deeper knowledge into their properties. High-entropy alloys have been the subject of recent attention due to their exceptional mechanical properties and unique microstructural characteristics. These alloys consist of multiple principal elements in non-equal atomic proportions forming a solid solution with high configurational entropy. The exploration of HEAs has created new opportunities for designing materials with improved mechanical performance and making them promising candidates for engineering applications. Fe-Ni-Cr-Mn-Mo high-medium entropy alloys offer a potential balance of optimal mechanical properties. High entropy alloys present impressive strength, ductility, and fracture toughness, making them suitable for various applications. However, the mechanisms governing their mechanical behavior at different temperatures are not well understood. Understanding these deformation behaviors is crucial for optimizing their microstructure for impressive mechanical properties. Twinning-induced plasticity is a process where materials deform through the formation and movement of twin boundaries, plays a significant role in improving the mechanical properties of alloys.

This study focuses on investigating the deformation behavior of Fe-Ni-Cr-Mn-Mo high-medium entropy alloys at three distinct temperature such as cryogenic (-196°C), room temperature, and 300°C.The aim is to comprehensively study how the deformation twinning behavior is influenced by alloy composition, entropy, and temperature. Tensile testing is a commonly accepted method for analyzing the mechanical properties of materials. It provides valuable insights into how alloys behave under different applied loads.

Advanced techniques like Electron Backscatter Diffraction and Electron Channeling Contrast Imaging technique are used to deeply study the microstructural features and twin deformation behavior. EBSD provides valuable information about the presence of TWIP behavior with exact crystal orientations while ECCI allows us to see nano twins and observe how contribution towards elongation and strength. The findings of this investigation show the existence of multiple orders of twinning in high-medium entropy alloys containing Fe-Ni-Cr-Mn-Mo chemical elements. This discovery sheds light on the underlying mechanism responsible for TWIP (twin-induced plasticity). By clarifying how deformations occur and

their reliance on factors such as alloy composition, entropy, and temperature. This study contributes to our understanding of the mechanical characteristics displayed by these alloys. These insights are important for advancing the development of advanced materials with improved mechanical properties, which have applications in various sectors such as aerospace, automotive, and energy industries.

The deformation behavior connected with role of twinning in high-medium entropy alloys, this research opens a wide overview for further optimization of their microstructure and mechanical properties. These insights can guide the design and development of new HEAs with tailored properties, creating advanced materials that exhibit superior performance in demanding environments and temperatures.

1.2 Research objective

This research aimed to investigate the deformation behavior of Fe-Ni-Cr-Mn-Mo high-medium entropy alloys at three different temperatures: -196°C, room temperature, and 300°C.The primary objective was to acquire an understanding of how alloy composition, entropy, and temperature influence the behavior of deformation twinning.

1) Thermodynamic calculations used to determine possibility of forming a disordered solid solution and phase stability in the high-medium entropy alloy based on enthalpy and entropy changes during alloying.
2) Analyse the mechanical performance of High-medium entropy alloys at cryogenic temperature, room temperature and high temperature and compare the strain hardening effect in terms of stress and strain concept.
3) Microstructure Analysis to identify deformation mechanisms connected to extraordinary elongation with strength property of High-medium entropy alloys.

1.3 Thesis Plan

1) Literature study
2) Test proposal
3) Tensile test
4) Sample preparation
5) SEM- EBSD+ECCI analysis
6) Obtain results plotting graphs and microstructure images.
7) Conclusion
8) Thesis writing

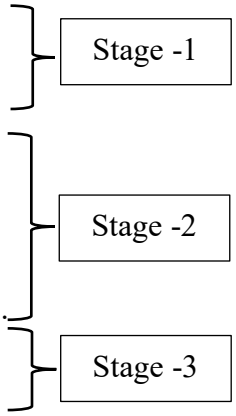

2 Theoretical backgrounds

The purpose of this chapter is to present the essential information studied from various literature studies necessary to understand the project. There is a general overview of high-medium entropy alloy regarding thermomechanical deformation behavior behind the extraordinary mechanical properties.

2.1 Definition

High entropy alloys are characterized by a unique combination of composition and configuration entropy. The composition is based on the number of alloying elements used to produce the alloys and at least five principal elements, and the atomic weight percentage of each element should be within 5–35% and minor element atomic weight percentage should be less than 5%. The presence of five or more elements in the composition of an alloy can increase the likelihood of forming a solid solution due to the resulting high degree of randomness. This randomness or configurational entropy enhances the solubility of the constituent elements and reduces the formation of intermetallic phases at high temperatures.

Configurational entropy is a critical characteristic that influences the classification of an entropy alloy as having high, medium, and low entropy is mentioned in figure 1.1. This property is closely associated with mixing and determines the degree of disorder within the alloy. A higher configurational entropy signifies a greater level of disorder and mixing in the system, resulting in an alloy with higher overall entropy. But lower configurational entropy implies more ordered arrangements within the structure, leading to form intermetallic compounds and chances of form other solid solutions.

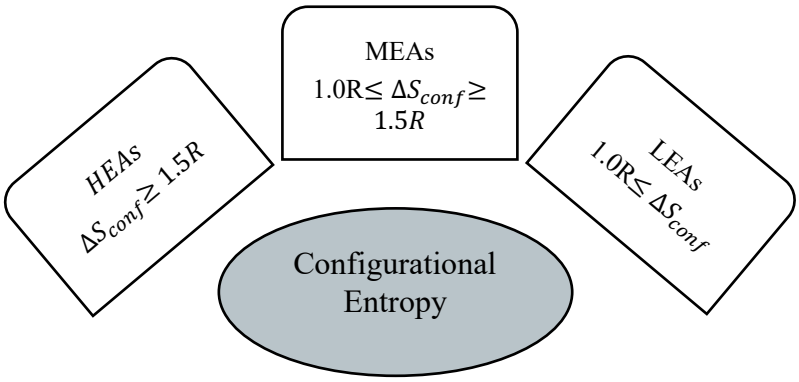

Figure 1.1Classification of entropy alloys based on entropy of configuration.

2.2 Thermodynamic calculation -Phase selection

Thermodynamic calculations are utilized to determine whether a HEA forms a disorder solid solution and the type of solid solution such as face-centred cubic, body-centred cubic or combination of both. HEAs are known for their distinct characteristic of increased disorder behaviour, primarily driven by higher entropy. This higher entropy effect in HEAs promotes the formation of disorder solid solutions and effectively eliminates the formation of intermetallic compounds, as there is no provision for ordered atomic networks. Therefore, by analysing the atomic weight percentages of the alloying elements and considering the impact of entropy, the thermodynamic calculations provide feasibility forming a disorder solid solution and provide insights into the specific type of solid solution (FCC, BCC, or both) that the HEA is likely to exhibit.

Configurational entropy

Configurational entropy expressed in terms of statistical thermodynamics- Boltzmann's equation.

$$\Delta S_{conf} = K_b \ln w \quad (2\text{-}1)$$

K_b - Boltzmann's constant and w- number of ways in which available energy can be distributed among the particles.

In the case of a solid solution with n components, in which the mole fraction of the ith component is x_i can be described as a random n-component solid solution. The ideal configurational entropy per mole of this solid solution can be expressed as [1]

$$\Delta S_{conf} = -R\sum_{i=1}^{n} x_i \ln x_i \quad (2\text{-}2)$$

R- gas constant -8,314J/K/mol

2.2.1 Phase selection rules in thermodynamic

Thermodynamic and geometry effect of HEAs are mainly contributed with Gibbs free energy, which is expressed in terms of enthalpy 'H' and entropy 'S'.

$$\Delta G_{Mix} = \Delta H_{Mix} - T\Delta S_{Mix} \quad (2\text{-}3)$$

ΔG_{Mix} - Gibbs free energy of mixing

ΔH_{Mix} - Enthalpy of mixing

ΔS_{Mix} – Entropy of mixing

T- Temperature required at which all elements are mixed.

From this equation to find the phase selection in HEAs and thermodynamic stability by using the values of ΔH_{Mix} & ΔS_{Mix} with respect to the temperature. Several factors can make impact on phase selection in HEAs, such as Enthalpy of mixing ΔH_{Mix}, Atomic mismatch δ, Entropy of mixing ΔS_{Mix}, New parameter Ω, Valance electron concentration VEC. Comparing the values of mutually related parameter in graphical way to highlight the phase formation location in graph and conclusion based on the theories invented by the scientists.

i) Enthalpy of mixing ΔH_{Mix}

$$\Delta H_{Mix} = \sum_{i=1, i\neq j}^{N} x_i \; 4\Delta H_{AB}^{mix} x_i x_j \qquad (2\text{-}4)$$

Where N- number of elements, x_i &x_j -composition of i_{th} and j_{th} elements and ΔH_{AB}^{mix}- pair enthalpy of mixing for possible pair of elements.

ii) Atomic mid mismatch δ

$$\delta = \sqrt{\sum_{i=1}^{N} x_i (1 - d_i / \sum_{j=1}^{N} x_j d_j)\text{^}2} \qquad (2\text{-}5)$$

Where $d_{i,} d_j$- atomic diameter of i_{th} and j_{th} element

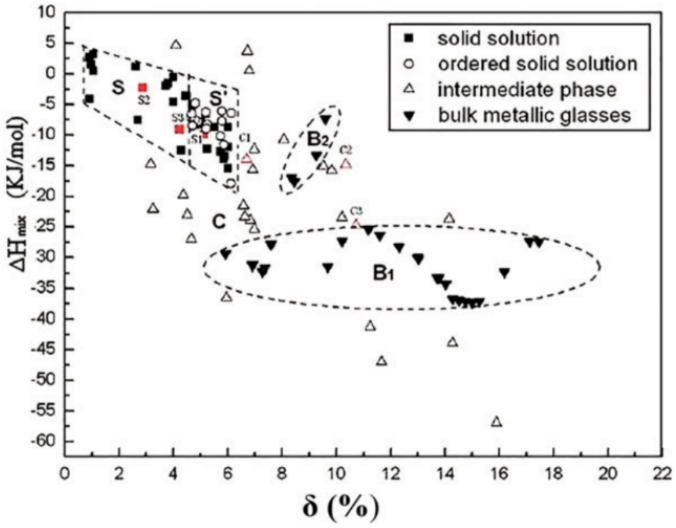

Figure 1. 2 Phase selection diagram based on enthalpy of mixing and atomic mismatch for HEAs according to reference [3]

The region marked with 'S' is representing the only disordered solid solution may form. Additionally, the atomic mismatch is very less so easily filling the lattice sites with component atoms for the formation solid solution.

iii) The new parameter Ω is dependent on ΔH_{Mix} & ΔS_{Mix} proposed by Yang and Zhang [3,4].

$$\Omega = \frac{T_m \Delta S_{Mix}}{|\Delta H_{Mix}|} \quad (2\text{-}6)$$

$$\Delta S_{mix} = -R\sum_{i=1}^{n} x_i \ln x_i \quad and \quad T_m = \sum_{i=1}^{N} x_i (T_m)_i \quad (2\text{-}7)$$

Where T_m – Average melting point of N element in the composition and $(T_m)_i$- melting point of ith element in composition.

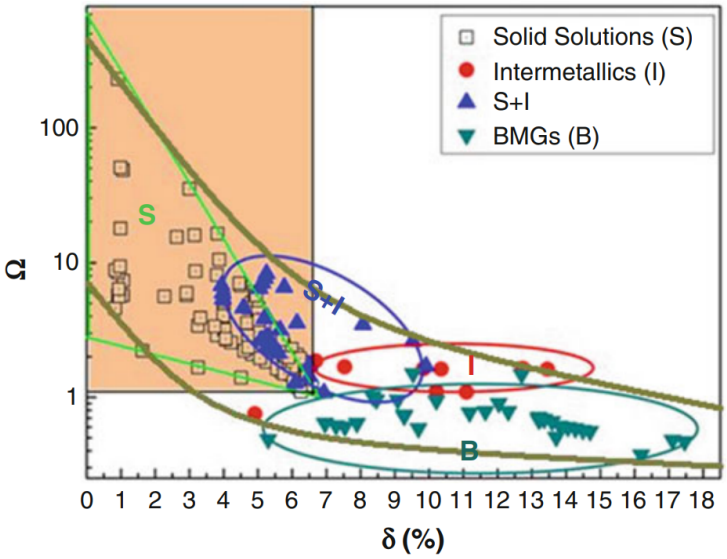

Figure 1. 3 Phase selection diagram based on Ω and atomic mismatch for HEAs [3,4]

As the new proposal is showing that solid solution is only formed when Ω ≥1.1 & $\delta \leq$ 6.6% [3,4]. In short upon design the alloys above and after the proposed range of values are indicating that formation of Intermetallic compound may form that is impact mechanical properties of the HEAs.

iv) Valence electron concentration is another parameter proposed by Guo's and it can determine probability of possible phases formation during mixing of elements and form solid solution [5].

$$\text{VEC} = \sum_{i=1}^{n} x_i \, (VEC)_i \tag{2-8}$$

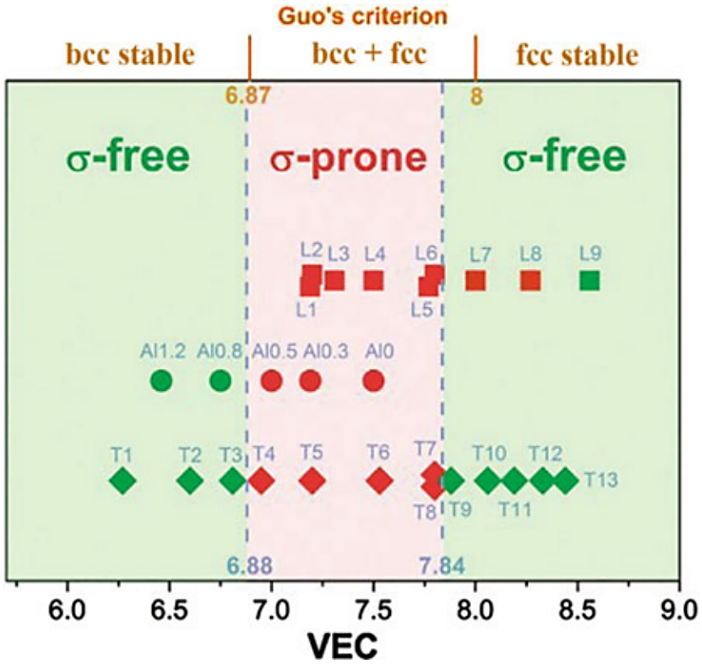

Figure 1. 4 Phase selection diagram based on VEC for HEAs [3]

2.3 Four core effect of high entropy alloy

Physical metallurgy is a scientific field investigating how composition and processing methods influence their microstructure's physical and mechanical properties of material. It is the relationships among composition, processing techniques, crystal structure, and microstructure through principles of thermodynamics, kinetics, and deformation theory [6,7]. Moreover, the connections between crystal structure, microstructure and material properties are explored using concepts from solid-state physics and theories related to strengthening, toughening, fatigue creep wear and other phenomena. Figure 1.5 briefly explains the core characteristics and impact on the properties of HEAs.

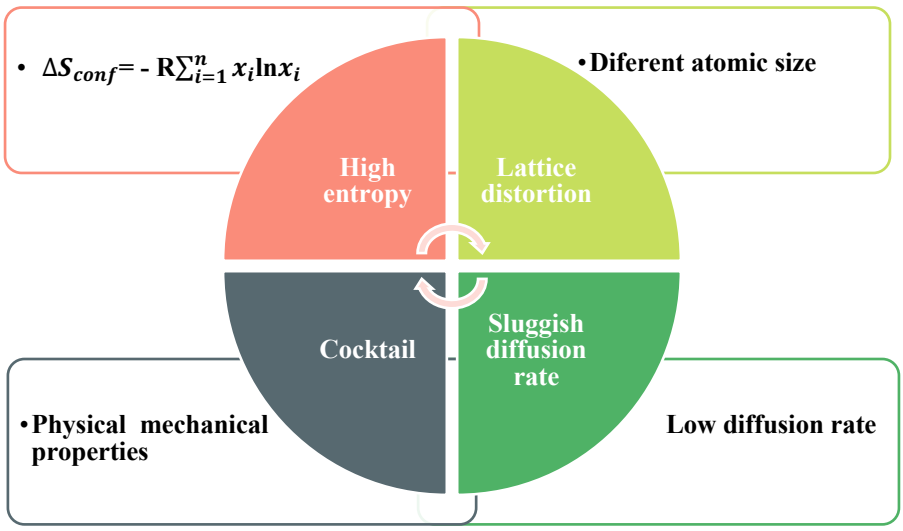

Figure 1. 5 Four core effect of high entropy alloy [8]

The high-entropy effect, sluggish diffusion effect, severe lattice distortion effect, and cocktail effect have significant impacts on various aspects of physical metallurgy. These effects play important roles in understanding the thermodynamics, kinetics, structure, and properties of materials. The high-entropy effect is particularly influential in determining the equilibrium structure and microstructure of materials. On the other hand, the sluggish diffusion effect affects how phase transformations occur over time and lag the diffusion process. The severe lattice distortion impact deformation theory as well as affects relationships between properties like strength or hardness with microstructure, along with potentially influencing both thermodynamics and kinetics. The cocktail effect in high-entropy alloys refers to the combined impact of composition, structure, and microstructure on their properties. Unlike conventional alloys that can be predicted using the rule of mixtures, HEAs display intricate atomic interactions and distinct phase characteristics which play a substantial role in defining their properties [6,7].

2.4 Deformation mechanism

The stacking fault energy is a fundamental property of alloys that plays a vital role in determining the deformation mechanism observed in HEAs with FCC solid solution. It refers to the energy required to create a stacking fault, which occurs when a crystal structure's regular stacking sequence of atomic layers is disrupted under deformation. This defect forms when shear forces cause the crystal plane of atoms to slip over the top and bottom layers of atoms. The SFE has long been recognized as alloys' critical intrinsic mechanical characteristic [11]. It significantly influences the plasticity and deformation behaviour of materials. Low stacking fault energy is desirable in alloys as it improves mechanical strength and ductility by mechanical deformation twinning, dislocation storage capacity, work hardening rate and Twinning Induced Plasticity [13]. By reducing the SFE, materials exhibit enhanced plastic deformation capabilities and are less prone to brittle fracture [12].

Understanding the SFE and its impact on deformation mechanisms is essential for this study. It helps in analysing mechanical elongation and designing materials with desired mechanical properties. By manipulating the SFE through alloying or microstructural modifications, it is possible to tailor the mechanical strength and ductility of materials to meet specific application requirements. The stacking fault energy is a crucial property influencing FCC alloys' plasticity and mechanical behaviour. Controlling the SFE optimizes material properties, improving mechanical strength and ductility [11].

2.4.1 Stacking fault

In FCC systems, the {111} planes are considered close-packed planes and are glide planes and coherent twin planes. These {111} planes exhibit an ABCABC stacking sequence, as depicted in Figure 2.1. The arrangement shows the atoms on the A plane, the subsequent plane on B sites and the third plane on C sites are normal to the A plane. The stacking fault energy is a measure of the energy required for partial dislocations to recombine and reorganize the stacking sequence of the material under applied shear stress. In FCC lattices, a stacking fault is represented by ABCAB|ABC, where A, B, and C denote the three instances of (111) planes in crystal. The missing of plane C indicates the presence of a stacking fault that is highlighted by "|" this symbol. The intrinsic stacking fault, characterized by a missing plane of atoms, is the most observed fault in FCC lattices. The B atoms are wrongly placed in position of c atom plane and create a fault in the plane. Figure 2.1illustrates an example of an intrinsic stacking fault resulting from applied shear stress. The faulted structure in Figure shows a missing "C" plane of atoms. In Figure 2.1 the atomic layers A, B and C are stacked in the ABC sequence along the c direction [4]. Reducing the stacking fault energy in a material is often advantageous for enhancing its strength and ductility. Materials with lower stacking fault energy tend to have a greater distance between dislocations, promoting deformation through twinning. This twinning deformation leads to increased strain hardening rate and improved ductility of the material. Consequently, stacking fault energy is a valuable indicator for predicting deformation behaviour and other

important properties, including radiation resistance, which are critical for designing and developing alloys.

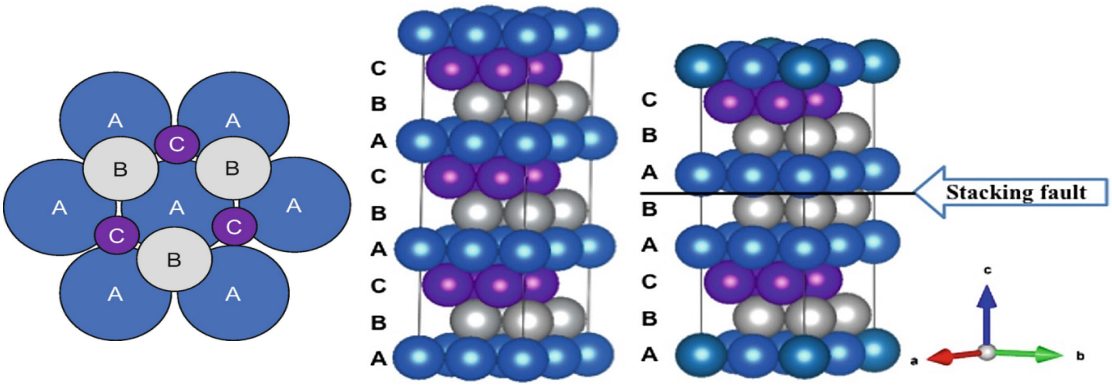

Figure 2. 1 shows the stacking fault mechanism and FCC with A (blue), B (white), and C (purple) layers shown along the c direction and intrinsic stacking fault present in FCC Visualization by VESTA [2,4].

The movement of dislocations typically controls plastic deformation in metals. In FCC, perfect dislocations with Burgers vectors [110] glide on the close-packed planes {111}. There are two types of dislocations in FCC structures, perfect dislocations, and partial dislocations. Perfect dislocations do not change the crystal structure during their motion, while partial dislocations create imperfections known as stacking faults. Perfect dislocations tend to split into Shockley partial dislocations, which the dissociation reaction can describe. The line energy reduction upon dissociation leads to the formation of Shockley partials with Burgers vectors as shown in figure 2.2.

$$\frac{a}{2}[10\bar{1}] \rightarrow \frac{a}{6}[11\bar{2}] + \frac{a}{6}[21\bar{1}] \quad -$$

$$b_1 \quad \rightarrow \quad b_2 \quad + \quad b_3$$

The creation of partial dislocation is not straight forward the perfect dislocation b_1 disassociate into b_2 leading partial and b_3 trailing partial. a is the lattice parameter and b is the burger vector.

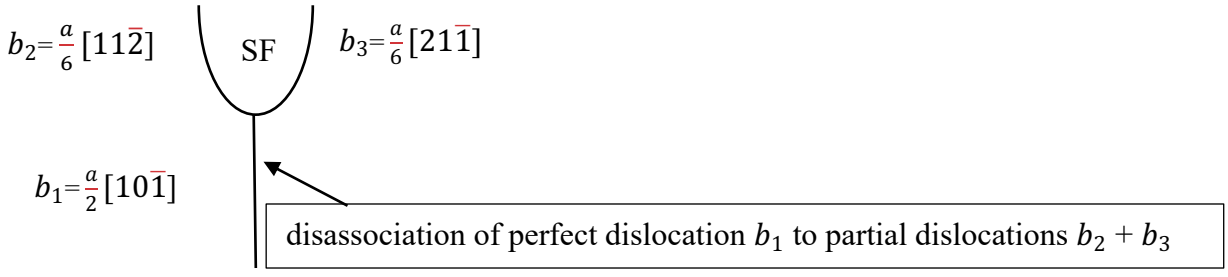

Figure 2. 2 Shows the disassociation of partial dislocations and area represents the stacking fault.

The dissociation distance between partial dislocations is significantly influenced by the SFE in a material. A low SFE indicates a larger separation distance between the two partials, while a high SFE suggests little or no separation distance. In practice, the stacking fault can extend throughout the entire grain. Materials with lower SFEs tend to form wide stacking faults and resulting in lower critical stress required for quasi-infinite dissociation compared to materials with higher SFEs.

2.4.2 Mechanical Twin deformation mechanisms

In FCC high -medium entropy alloys, the process of generating twins can be triggered by the sequential shearing of a three-layer {1 1 1} plane along a dislocation. This shear motion is responsible for determining the generalized planar fault energy, which governs twinning nucleation. The deformation process is visually depicted in Figure 2.3. Initially, Figure 2.3 (a) represents an ideal FCC lattice structure. Figure 2.3 (b), (c), and (d) shows atomic configurations after each step of successive shearing along one partial Burger's vector. As a result of this shearing action, there will be an alteration in the atomic stacking sequence from ABCABCABC as it appears in perfect lattice to ABCACBABC characteristic configuration observed in the three-layer twinning arrangement. This change indicates the formation of a twin boundaries within the material [6]. Deformation twinning is commonly associated with low and intermediate stacking fault energy values. This is because twinning occurs as successive stacking faults on adjacent {111} planes. The presence of a low SFE enables the formation of wider stacking faults and enhances the lattice parameter distances of their occurrence on neighbouring planes.

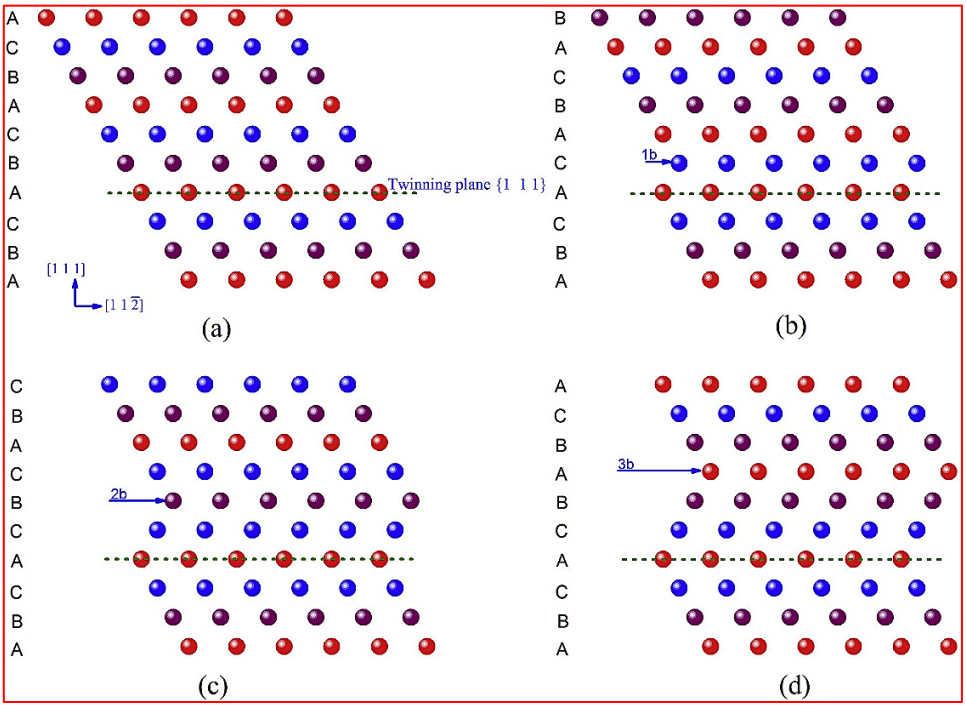

Figure 2.3 represents Twinning deformation mechanism in high entropy alloys [6]

2.5 Uniaxial Tensile testing

This chapter has already discussed in part -1 chapter 2.5 and same procedure is followed this uniaxial tension test. However, the strain hardening behaviour analysed in this study for understanding the work hardening effect linked with material elongation property. It is plotted by finding the $d\sigma_t$ & $d\ \varepsilon_t$ from true stress and true strain data. Then apply it equation (2-5) to obtain strain hardening rate. This rate is then plotted against true stress on the x-axis and strain hardening rate on the y-axis. By examining the resulting plot, we can gain insights into the plastic deformation behaviour by observing any bumps in the plastic region before the point of fracture.

The strain-hardening rate is calculated by the following equation.

$$\text{Strain hardening rate} = \frac{d\sigma_t}{d\ \varepsilon_t} \qquad (2\text{-}5)$$

3 Material and Experimental Method

This chapter will go through the detailed description about materials, mechanical test methods and microstructure analysis conducted to resolve the research questions.

3.1 Material

The experimental specimens were prepared through the manufacturing process of casting, followed by hot rolling to produce the desired bar material 7x7x500 millimetre. The annealing heat treatment was conducted on the high-medium entropy alloys at temperatures ranging from 1100°C - 1200°C for the purpose of homogenization. During this heat treatment process, the alloys were subjected to elevated temperatures within this temperature range for 30 minutes. After the material treatments, the specimens underwent machining processes to achieve the precise dimensions necessary for the subsequent mechanical testing. This preparation methodology ensured the production of high-quality specimens for accurate and reliable experimental tension testing.

Table 3. 1 Chemical composition of all six M-HEAs in atomic weight percentage.

Alloy	Heat	Ni	Cr	Fe	Mn	Mo	Co	Al	N	Cu
No 1	5299	27,18	19,63	44,28	5,88	3,03				
No 4	5302	49,24	35,37	0,12	6,29	4,16	4,82			
No 6	5304	28,67	23,89	28,57	6,03	3,01	4,74	5,09		
No 7	5382	27,92	23,28	29,65	5,99	2,99	4,27	3,65		2,25
No 10	5385	60,9	22,54	5,7	6,25	4,21			0,4	
No 17	5392	26,16	19,83	44,26	5,77	3,05			0,93	

3.2 Uniaxial tension test

The first step in conducting a tensile test is to prepare the specimen according to ASTM E8 guidelines. The gauge length of the sample is then measured and recorded. To ensure accuracy, stereography and a calibrated micrometre are used for dimensional assessment. According to the standard, the gauge length should be five times the diameter. In this sample, the length measures 20 millimetres while the diameter measures 4 millimetres as explained in figure 3.2. It is important to note that slight deviations between actual measurements and specified dimensions may exist. The purpose of the tension test is to find the mechanical properties such as ultimate tensile strength, elongation, and strain hardening behaviour.

Tensile experiments were carried out utilizing the MTS landmark servo-hydraulic test system at three different temperature such as -196°C, room temperature, and 300°C. The tests conducted at RT and 300°C took place in a regular ambient air environment, while those performed at -196°C involved a specially designed chamber filled with liquid nitrogen

to completely submerge both the specimens and grips. Strains during RT & 300°C testing were measured using an extensometer connected to the gauge section of the material, for accurate determination of engineering stress-strain curves by combining these strains with data from the load cell output. Due to extremely low temperatures during testing at -196C°, extensometer could not be employed. Instead, it determined the elongation by manual examination using stereographic measurement technique.

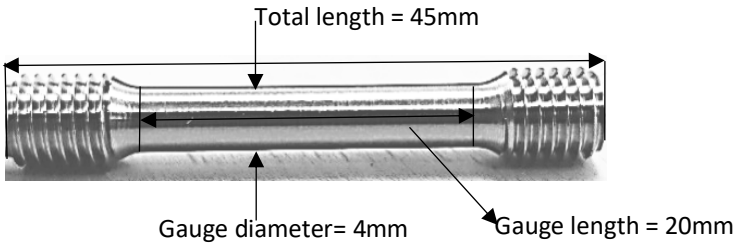

Figure 3. 2 Dimension information of samples used in this experiment for tension test.

3.3 Metallographic preparation

This chapter is already discussed in Part-1 chapter 3.3 and same methods have been followed by this experimental study.

3.3 Microstructure characteristics

The deformation behaviour of the samples is analysed using a combination of EBSD and ECCI techniques to understand the underlying mechanisms of plastic deformation. The well-polished samples are securely placed in the EBSD holder and inserted into the FEG-SEM chamber. The chamber undergoes a vacuum-filling process to ensure optimal imaging conditions. The EBSD detector is positioned at a 70-degree tilt toward the sample to capture the Kikuchi diffraction patterns. A small step size is utilized during scanning to accurately index each Kikuchi band, providing detailed crystallographic information in a localized area. The EBSD scan data is saved and later analysed using Aztec crystal software to identify twin deformations based on high-angle grain boundaries, typically using Misorientation variation Σ3 60° <111> CSL. The MTEX MATLAB package is employed to confirm the presence of twin deformations further using the detected high-angle grain boundaries.

The ECCI technique is also performed in the same FEG-SEM Ziess Sigma setup, utilizing a short working distance. ECCI relies on backscattered electrons to create contrast images and can provide nano twins that cannot provided by EBSD. Combining EBSD and ECCI methods allows for a comprehensive analysis and verification of twin deformations in the samples.

Detailed information has also been discussed in part-1 chapter 3.4 section.

4 Results and discussion

This chapter will discuss about results of six alloys deformed under different temperature. Each alloy is individually analysed and discussed in terms of mechanical properties, thermodynamic properties, and microstructural characteristics.

4.1 Thermodynamic phase selection calculation

The phase selection in HEAs is strongly influenced by the enthalpy of mixing ΔH_{mix} and atomic-size difference (δ). According to data in Table 4.1 and plots in figure 4.1, where all six alloys meet the condition of ΔH_{mix} and atomic-size difference at high temperatures near the melting point, these alloys are likely to form solid solutions, as depicted by the region of disorder solid solution in the Figure 4.1 marked as red rectangle [3].

However, certain as-cast samples with ΔH_{mix} below -15 kJ/mol and an atomic-size difference greater than 6.6% can exhibit stable intermetallic compounds or metastable metallic glasses. This suggests that under specific conditions, these alloys may undergo phase transformations leading to the formation of different structures. The VEC is another factor that helps determine the solid solution structure. In the provided table, all alloys exhibit VEC values greater than 7.8, indicating the stability of the FCC phase. As the results from calculation that put into the Figure 4.2 with red marking. From that it is clear that all alloys are FCC stable solid solution form and experimentally it is identified. The data from the table and plot confirm that the six alloys meet the conditions for solid solution formation at high temperatures. The VEC values further suggest the prevalence of the FCC phase in these alloys. These findings contribute to our understanding of the phase selection behaviour in HEAs and provide insights into their structural properties under specific thermodynamic conditions [5]. The Ω vs atomic mismatch is another method to design HEA whether it form only solid solution or other mix of solid solution with intermetallic compound and metallic glass. But as per the calculated data of Ω and atomic mismatch into the theoretical graph and it is obeying the theory invented by researchers. Phase selection in HEAs is influenced by multiple factors, including mixing enthalpy, atomic-size difference, and valence-electron concentration. Understanding these relationships can aid in predicting and controlling the formation of different phases in HEAs under varying temperature and processing conditions.

Table 4.1shows the thermodynamic phase selection test results.

Alloy	ΔH_{mix}(kJ/mol)	Atomic mismatch(δ)	VEC	ΔS_{mix}(j/mol)	Ω	ΔS_{conf}
No 1	-3,5	3,2	8,02	10,86	5,7	1,3
No 4	-6,5	3,3	8,17	9,8	2,83	1,2
No 6	-6,7	4,3	7,8	13,54	3,64	1,6
No 7	-5	4,1	7,9	13,88	5,17	1,7
No 10	-7,2	3,5	8,6	9,39	2,38	1,1
No 17	-6,69	3,65	7,98	11,19	3,09	1,3

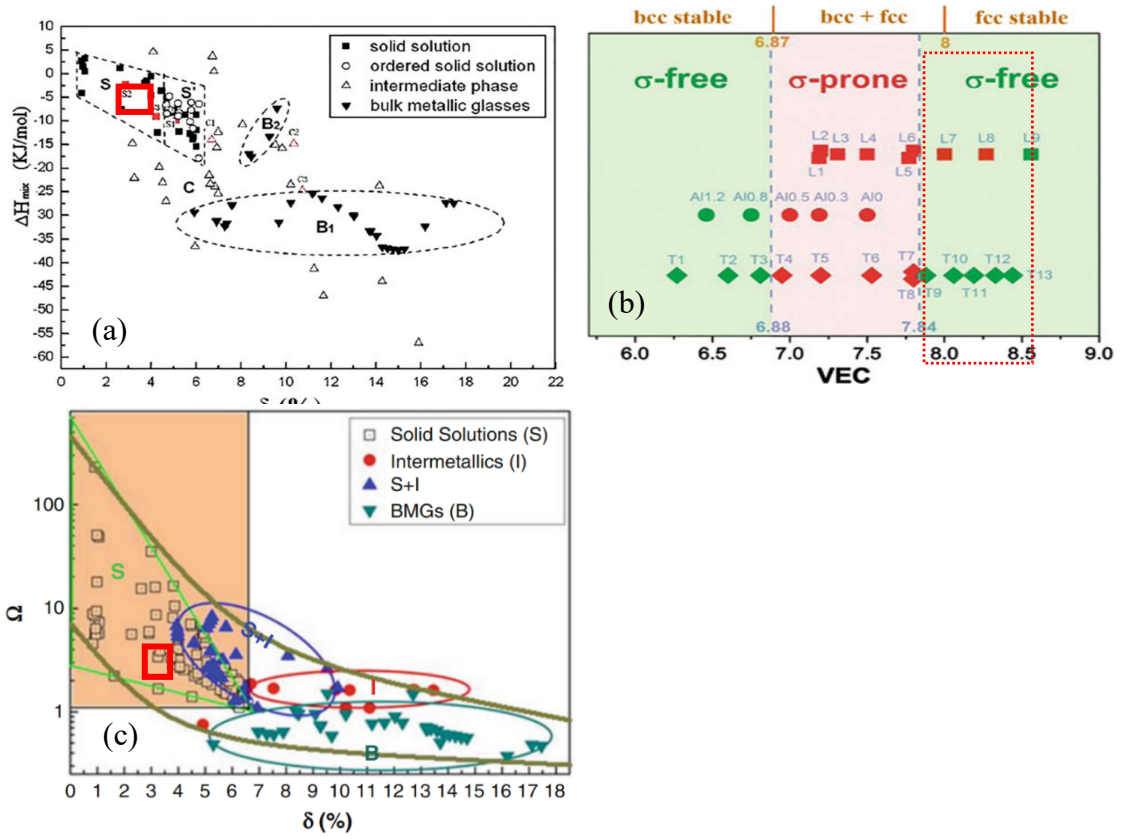

Figure 4. 1(a) Phase selection diagram based on enthalpy of mixing and atomic mismatch, (b) Phase selection diagram based on VEC, (c) Phase selection diagram based on Ω and atomic mismatch.

4.2 Mechanical test results

For each test, the UTS and elongation values are provided at three different temperatures are shown in figure 4.1,4.2 & 4.3 and table 4.1. MEA TWP-1 demonstrates significantly increased elongation at cryogenic temperature compared to other alloys at -196℃. At -196℃, the elongation reached an impressive 89.4%, while it decreases to 51.0% at room temperature and further drops to 46.0% at a higher temperature of 300℃. These findings indicate that MEA TWP-1 possesses extra ordinary ductility behaviour, enabling it to undergo greater deformation without fracturing when exposed to cryogenic temperature. TWP-1 exhibits lower strength as the temperature rises from cryogenic to high levels. At -196 ℃, it demonstrates an ultimate tensile strength of 943 MPa, which decreases to 564 MPa at room temperature and further down to 453 MPa at 300℃. The decline strength in TWP-1 with increasing temperature suggests that its ability to bear loads reduces as temperatures rise.
MEA TWP-17 demonstrates superior strength at extremely low temperatures, particularly at -196 ℃. At this temperature, it has ultimate tensile strength reaches an impressive value of 1277 MPa. However, as the temperature increases to room temperature and above, the UTS decreases considerably to 730 MPa and 566 MPa, respectively. It is evident that MEA TWP-17 performs exceptionally well under cryogenic conditions by displaying remarkable resistance towards high-stress levels even when exposed to low temperatures.

MEA TWP-10 has exceptional strength and elongation properties at different temperature ranges. At room temperature and 300℃, MEA TWP-10 exhibits high tensile strength. Specifically, it demonstrates a UTS of 762 MPa at room temperature, which increases to 1138 MPa at -196℃. However, the UTS slightly decreases to 639 MPa when exposed to higher temperatures. TWP- 10 exhibits consistent and stable elongation properties across all range of temperatures. At room temperature, the value is recorded at 65.3%, while at -196℃, it slightly decreases to 64.8% and further drops to 63.3% at 300℃. This indicates that MEA TWP-10 retains its ability to deform plastically throughout varying temperature conditions without significant deviations in elongation values by activating different deformation behaviour. TWP-6 & TWP-7 are HEA category that means more entropy and disorder and it has good elongation at cryogenic temperature but not superior over TWP-1.

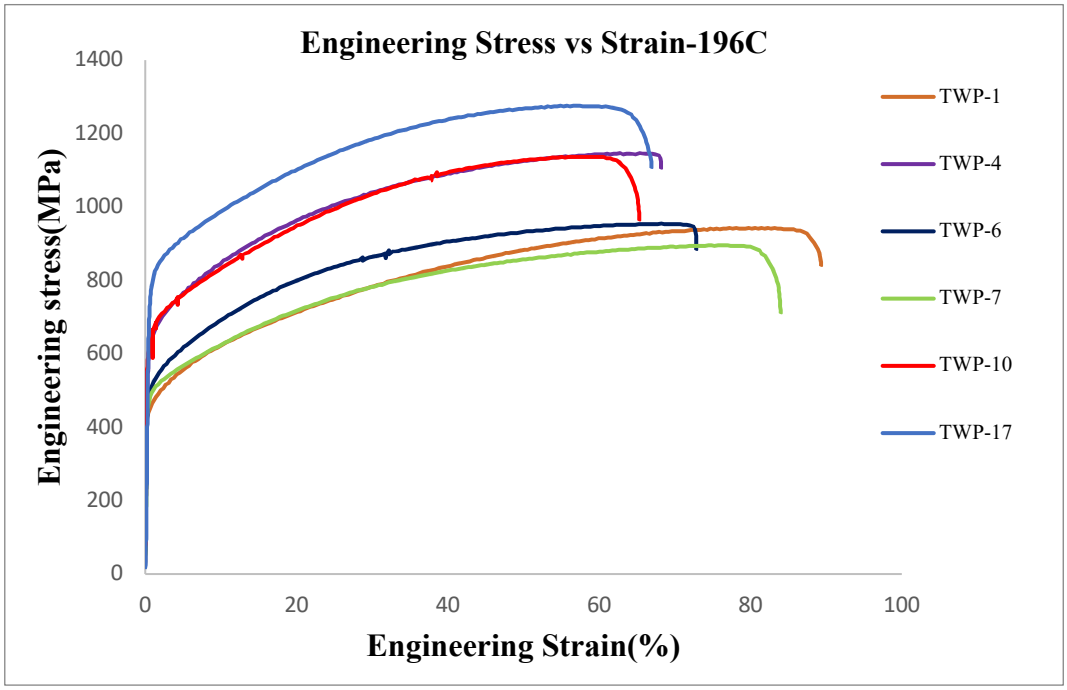

Figure 4. 2 Shows engineering stress vs engineering strain diagram for 6 alloys deformed at -196℃.

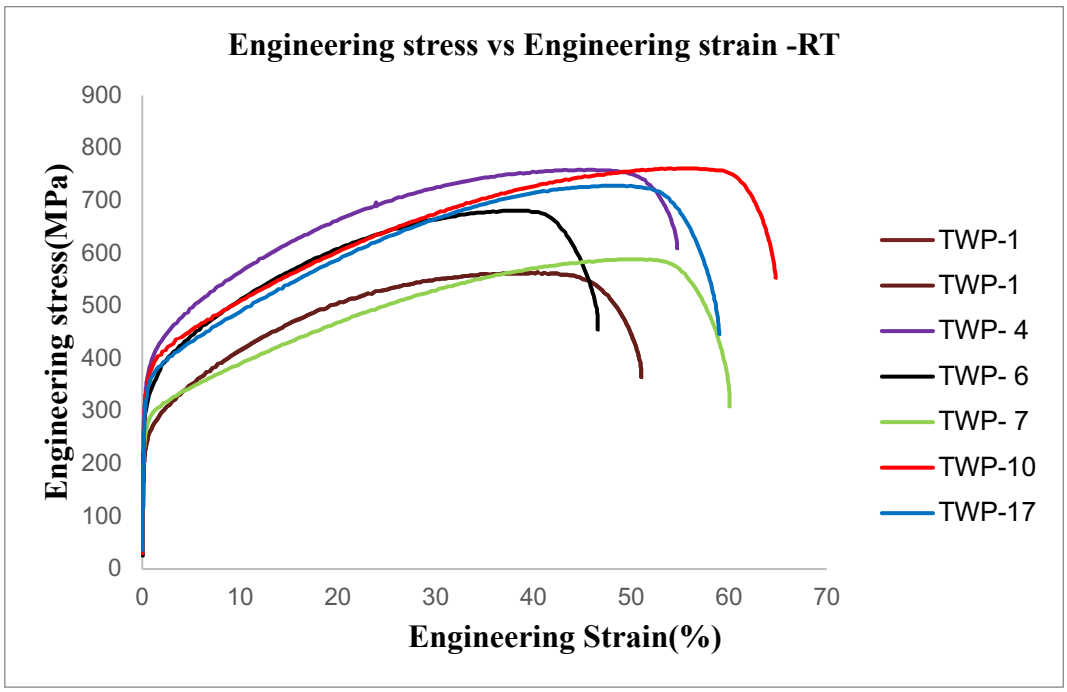

Figure 4. 3 Shows engineering stress vs engineering strain diagram for 6 alloys deformed at RT.

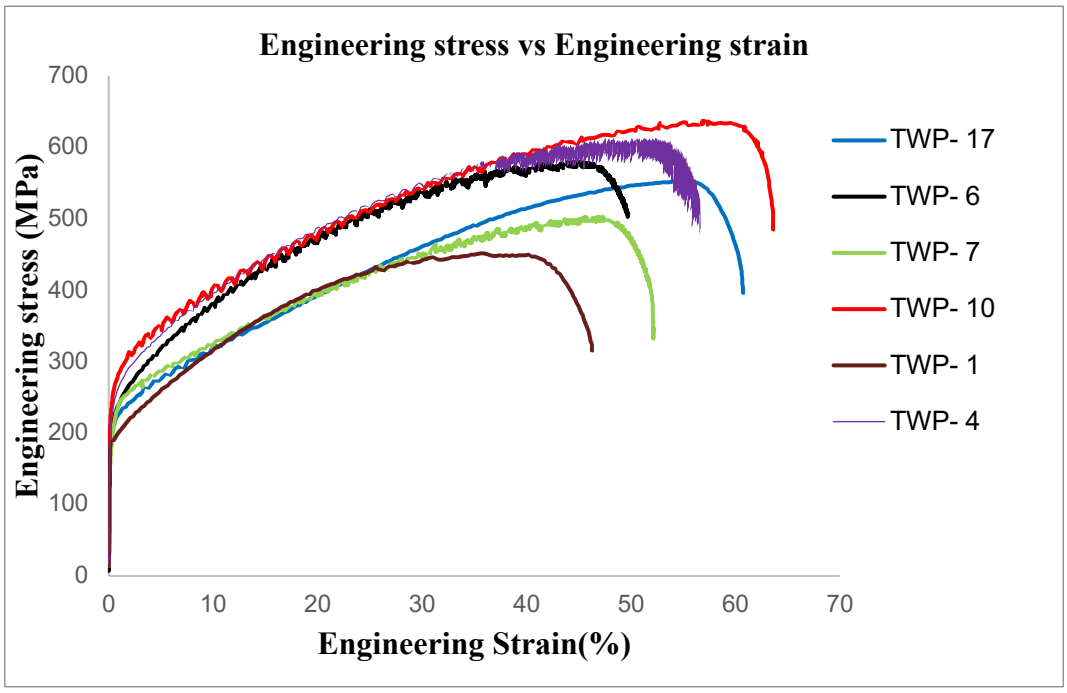

Figure 4.4 Shows engineering stress vs engineering strain diagram for 6 alloys deformed at 300℃.

Table 4. 2 Mechanical test results of 6 High -Medium entropy alloys

Test no	UTS (MPa)			Elongation (%)		
No	**RT**	**-196**℃	**300**℃	**RT**	**-196**℃	**300**℃
No7	590	896	503	60,1	84,0	52,5
No10	762	1138	639	64,8	65,3	63,3
No17	730	1277	566	59,0	67,0	56,4
No1	564	943	453	51,0	89,4	46,0
No4	759	1148	615	54,7	68,2	56,3
No6	682	954	581	46,6	72,9	50,1

4.3 MEA-TWP -1

This MEA Ni-Fe-Cr-Mn-Mo has conducted uniaxial tension test at 196℃,RT and 300℃ with same strain rate. Both mechanical test results and microstructure analysis are discussed in this section.

Deformation hardening behaviour

Figure 4.5 shows strain hardening curve, that provides valuable information about the different stages of deformation behaviour. At cryogenic temperatures, the curve initially falls that is termed first stage in the plot, where deformation is primarily driven by dislocation slip. This indicates that the material is undergoing plastic deformation through the movement of dislocations within the crystal lattice. Middle of the curve there is a noticeable peak in the strain hardening curve. This suggests that twin deformation becomes the dominant mechanism contributing to the strain-hardening effect that confirmed from microstructure analysis. Twinning involves the formation of mirrored crystal structures, leading to increased strength and deformation resistance by increasing the lattice parameter [16]. In the middle of the strain hardening curve, specifically at a strain rate of 35%, there is possibility to activate secondary twin deformation. This indicates the occurrence of additional twin formations, possibly of multi order twin pattern. The presence of multiple twin deformations suggests complex deformation behaviour in this region. However, as the temperature increases towards room temperature and further to 300°C, there is a significant reduction in elongation. This is clearly reflected in the strain hardening curve, which shows a declining trend without any noticeable peak in the strain hardening effect.

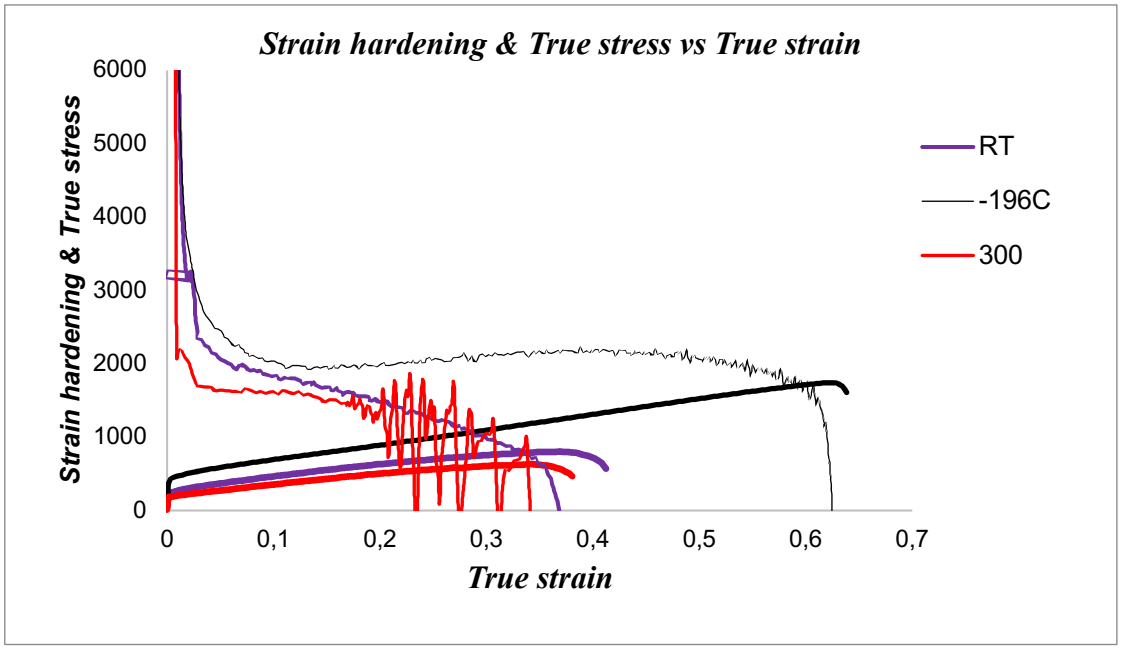

Figure 4.5 Strain hardening vs true strain plots for samples deformed at 196℃, RT and 300℃

Deformation Microstructure

At -196℃, the EBSD & ECCI high magnification images reveal a significant volume of twin deformation. The presence of numerous twins indicates that the material has undergone extensive twin formation during deformation at this temperature. Furthermore, upon closer examination, the EBSD images show the occurrence of multi-order twins as shown in figure 4.7. This suggests that the material has experienced multiple stages of twin deformation with possibly involving multi order twin structures. The high volume and complexity of twin deformation at -196℃ indicate a pronounced twinning behaviour in the material under these cryogenic conditions. Moving to RT, the EBSD and ECCI in figure 4.8 shows the presence of twins is still observed, but the volume of twin deformation relatively lower compared to -196℃. While the extent of twin deformation may be reduced, it is important to note that the material still exhibits a significant number of twins. These twins contribute to the deformation behaviour and influence the mechanical properties of the material at RT. The EBSD and ECCI clearly shown that there is no more multi twins found in case of sample deformed at room temperature. As the temperature increases to 300℃, EBSD images in figure 4.6 shows much less presence of twins compared to both -196℃ and RT. This indicates that the material exhibits fewer twin formations at elevated temperatures. The reduced occurrence of twins at 300℃ suggested that dislocation may be dominant over the twin deformation mechanism. CSL high angle detected at grain boundaries Σ3 60° <111> **as** well as annealing twin boundaries are noted.

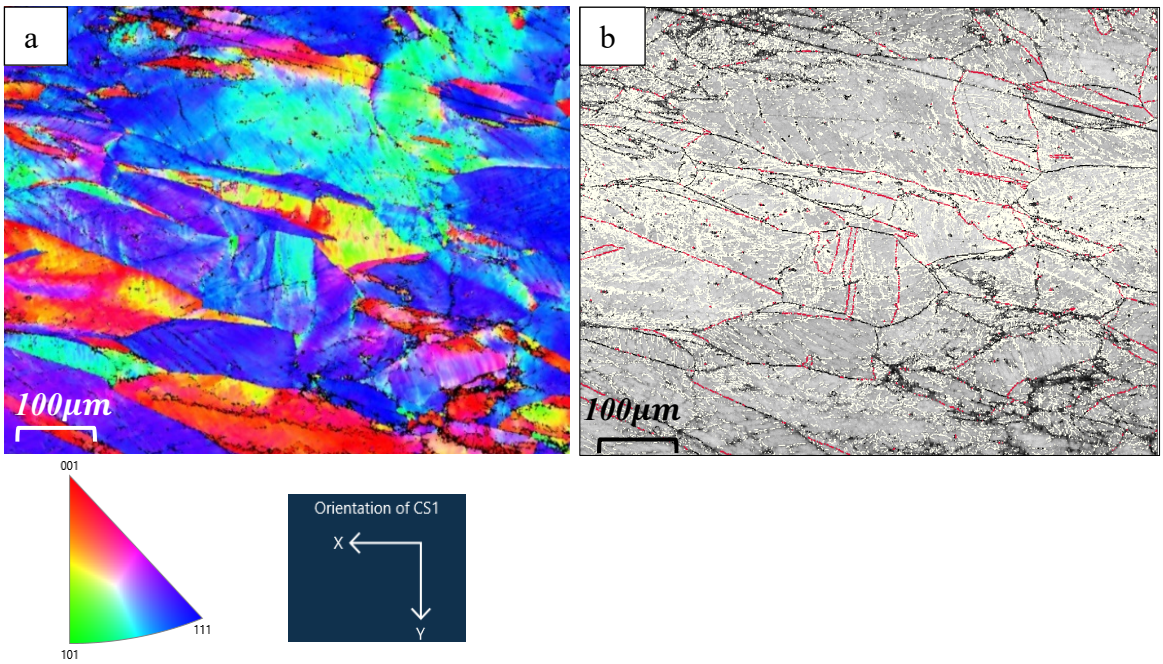

Figure 4. 6 shows sample deformed at 300℃ (a) EBSD IP shows the deformation twins red colour grains and blue represents the FCC austenite matrix. (b) EBSD BC and red colour represents the CSL Misorientation variation Σ3 60° <111>

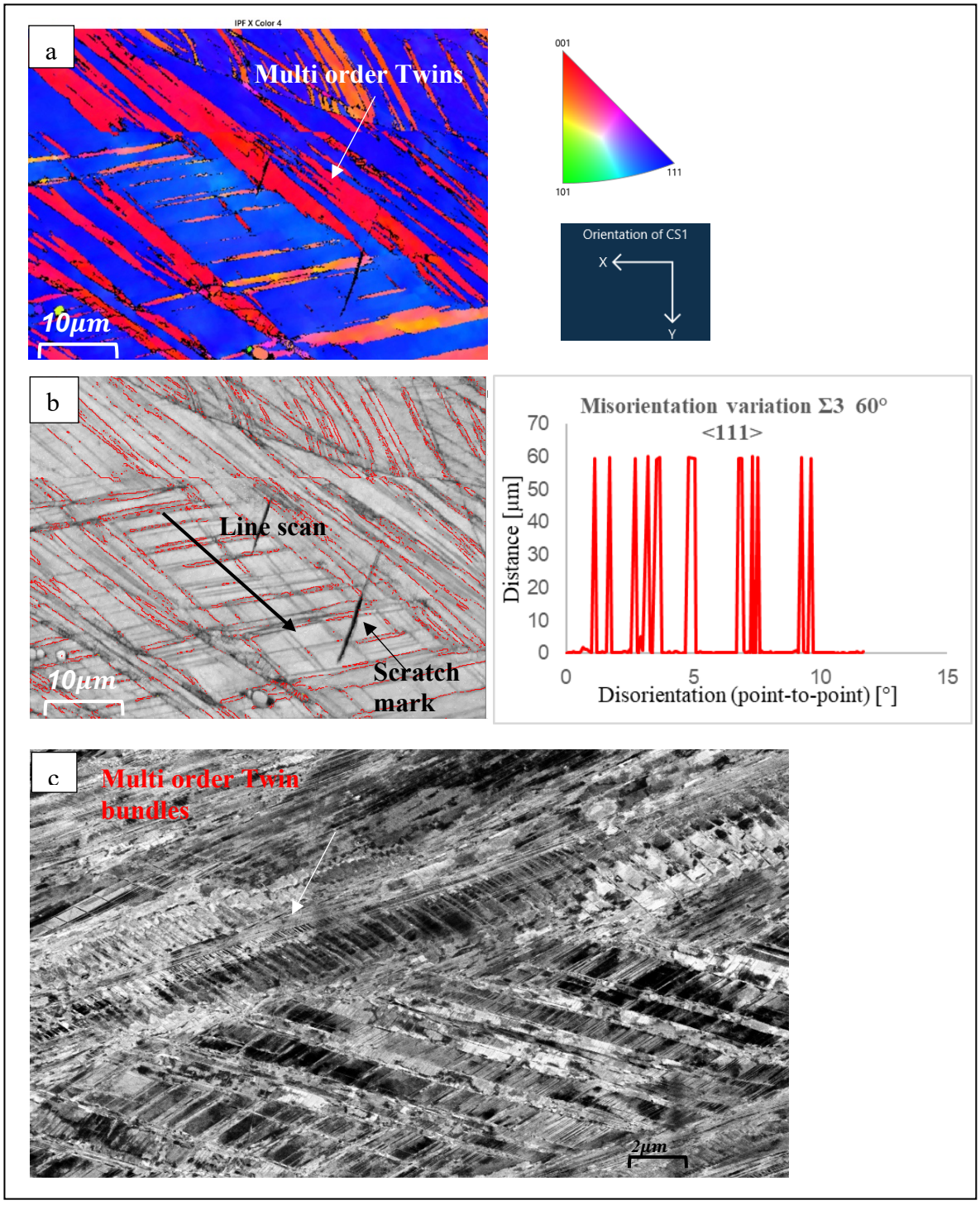

Figure 4. 7 Shows sample deformed at -196℃ (a) EBSD IP shows the deformation twins red colour grains and blue represents the FCC austenite matrix. (b) EBSD BC and red colour represents the CSL Misorientation variation Σ3 60° <111>. (C) ECCI image showing deformation twin bundles with multi order.

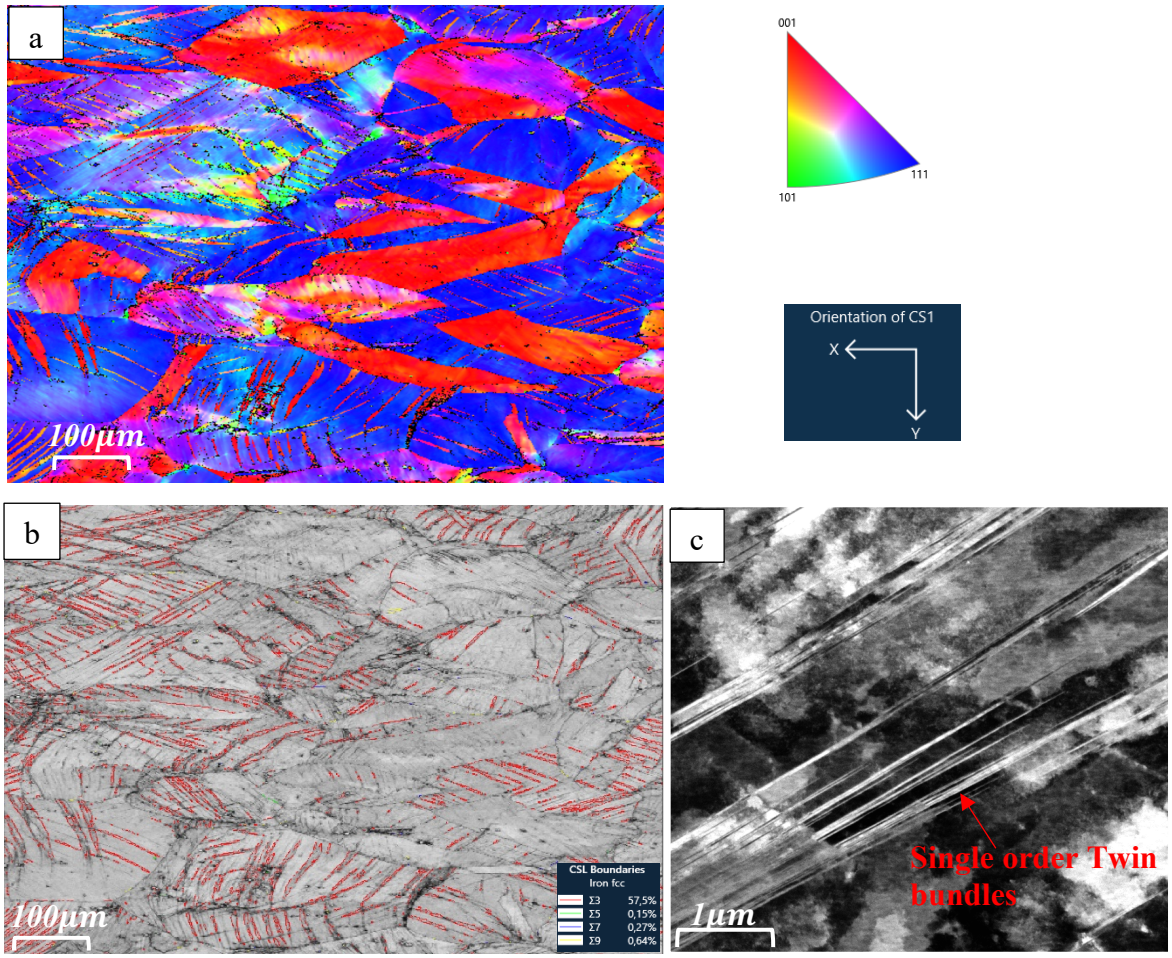

Figure 4. 8 Shows sample deformed at RT (a) EBSD IP shows the deformation twins red colour grains and blue represents the FCC austenite matrix. (b) EBSD BC and red colour represents the CSL Misorientation variation Σ3 60° <111>. (C) ECCI image showing deformation twins.

4.4 MEA-TWP - 4

This MEA with Ni-Fe-Cr-Mn-Mo-Co alloying elements with non-equiatomic alloying elements was deformed uniaxial tension test at 196℃, RT and 300℃ with same strain rate. Both mechanical test results and microstructure analysis are discussed in this section.

Deformation hardening behaviour

The curves in figure 4.9 demonstrates that the onset of work hardening occurs at different strain hardening values, with a decreasing trend from cryogenic to high temperatures. Observations reveal that samples deformed at cryogenic temperatures shows greater strength and work hardening effect and indicating the initiation of work hardening in the 3000 MPa range after yielding strain hardening curve large area under the curve. The range of work hardening diminishes for room temperature and high-temperature deformations. Furthermore, the plastic deformation region appears more extensive for cryogenic temperatures than the other two. This disparity has prompted further investigation and studies. The temperature variation is associated with activating different deformation behaviours that contribute to work hardening. The curve's behaviour changes as the temperature fluctuates. The intersection points of the curves representing true stress versus true strain and strain hardening versus true strain signifies the fracture point. Serration behaviour is observed in the high-temperature curve, suggesting potential dynamic strain aging. This phenomenon occurs after yielding and continues until fracture within the plastic deformation region. However, additional analysis is needed to confirm the presence of dynamic strain aging. Microstructural examination has shown that twin deformation is a key factor influencing the observed deformation behaviour, requiring further explanation.

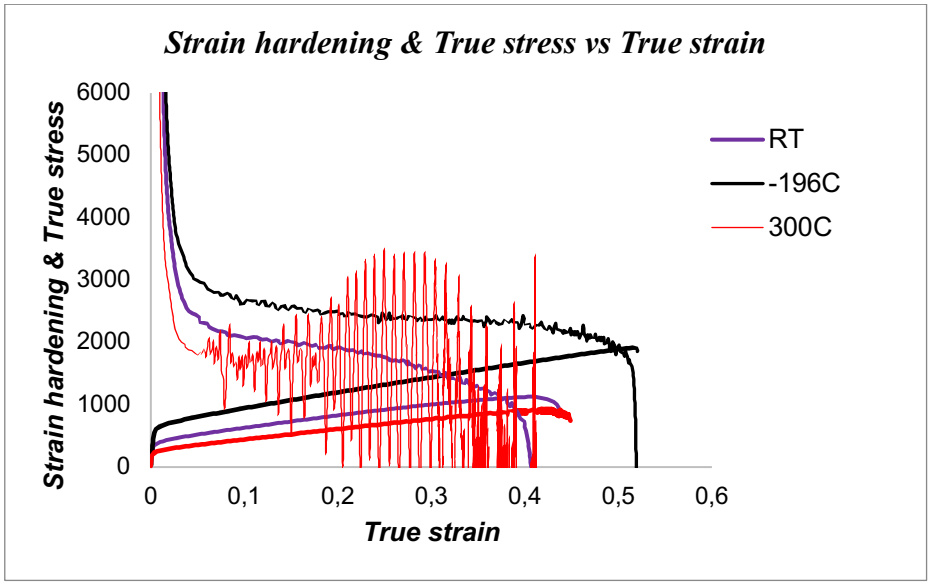

Figure 4. 9 Strain hardening vs true strain of samples deformed at 196℃, RT and 300℃

Deformation Microstructure

At a temperature of -196℃, figure 4.10 EBSD images exhibit substantial twin deformation. The prominence of numerous twins signifies that the material has experienced extensive twin formation during deformation under these cryogenic conditions. Upon closer examination, it becomes apparent from the EBSD images that a few multi-order twins have also formed. Moving on to room temperature, it is clear from Figure 4.11 EBSD, that twinning persists within the material, although comparatively lower levels of twin deformation may be present compared to those observed at -196℃. Despite the reduced extensiveness of twin formation at RT, twins still contribute significantly to the material's deformation behaviour and affect its mechanical properties. As the temperature increases to 300℃, Figure EBSD IP shows the twin deformation detected even further at elevated temperatures. But less twin volume fraction when compared to both -196℃ and room temperature RT. Dislocation slip may dominant mechanisms for deformation in the material and that is discussed in general discussion part. The work hardening nature is also showing that significant increases in middle of the curve showing in Figure 4.12 and that is evident coupled with microstructure revealing that presence of twin deformation may be the reason for increasing trend in the strain hardening.

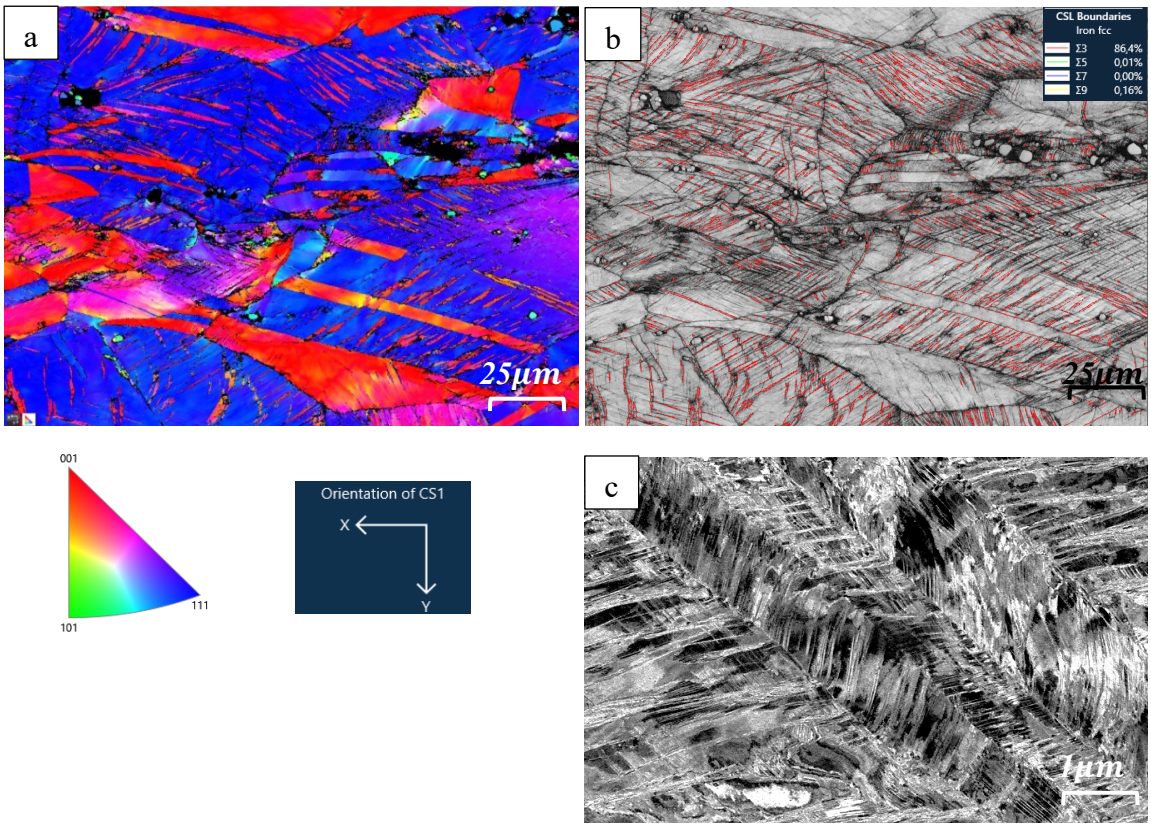

Figure 4. 10 shows sample deformed at -196℃ (a) EBSD IP shows the deformation twins red colour (b) EBSD BC and red colour represents the CSL Misorientation variation Σ3 60° <111>. (C) ECCI image showing deformation twin bundles

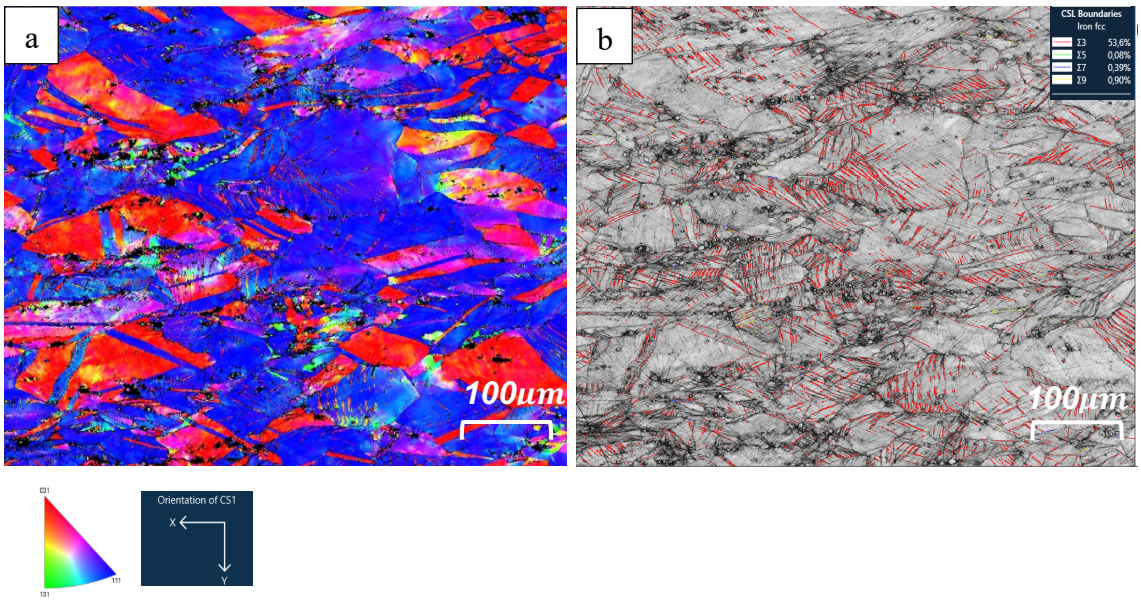

Figure 4.11 shows sample deformed at RT (a) EBSD IP shows the deformation twins red colour grains and blue represents the FCC austenite matrix. (b) EBSD BC and red colour represents the CSL Misorientation variation Σ3 60° <111>

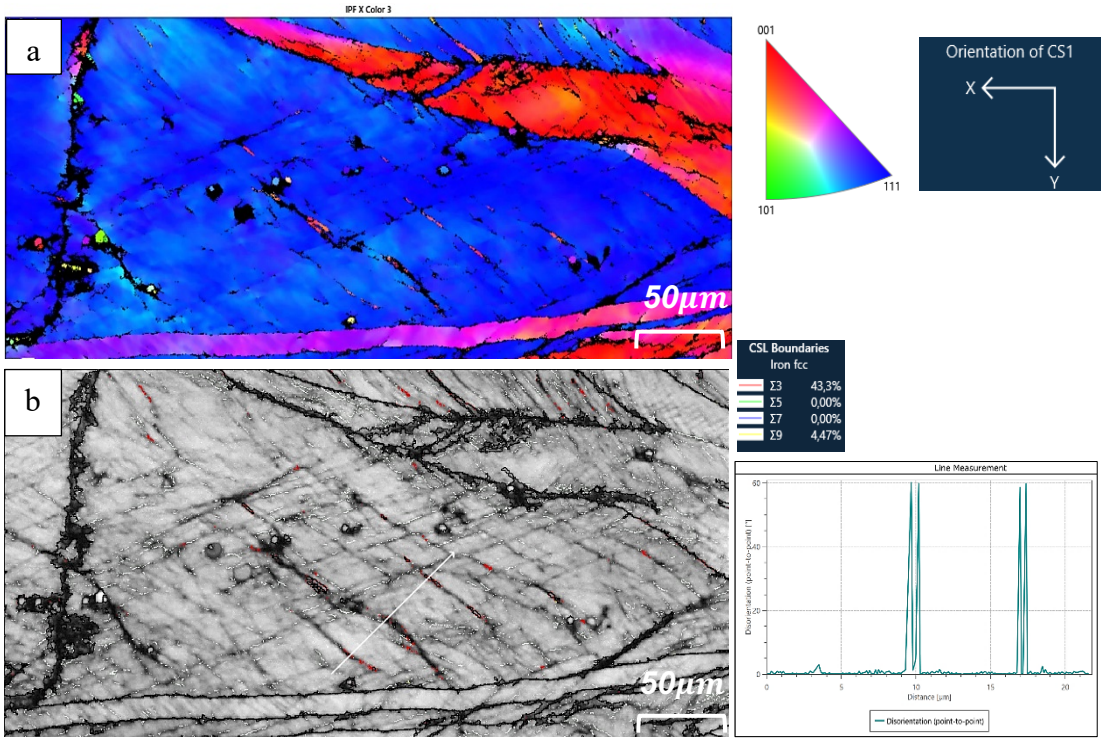

Figure 4.12 shows sample deformed at 300℃ (a) EBSD IP shows the deformation twins red colour grains and blue represents the FCC austenite matrix. (b) EBSD BC and red colour represents the CSL Misorientation variation Σ3 60° <111>.

4.5 HEA-TWP – 6

The HEA Ni-Fe-Cr-Mn-Mo-Co-Al was deformed uniaxial tension test at 196℃, RT and 300℃ with same strain rate. Both mechanical test results and microstructure analysis are discussed in this section. This alloy is a combination of 7 elements and designated as high entropy alloy because its configurational entropy is more than 1.5R.

Deformation hardening behaviour

Work-hardening effect in plastic region starts temperature range of approximately 2000-3000 MPa as shown in figure 4.13. Plastic deformation region was found to be more extensive in cryogenic temperatures compared to the other two conditions. Temperature variations are believed to be crucial in activating distinct deformation behaviours, ultimately contributing to work hardening. The behaviour of the curve alters as the temperature fluctuates. Samples deformed at cryogenic temperatures exhibit a remarkable combination of strength and ductility with the exceptional performance exhibited by the work-hardening effect in these conditions. In the high-temperature curve, elongation is greater in samples deformed at high temperatures compared to room temperature. The serrations on the curve begin from initial work hardening and continue until reaching fracture. A gradual decline in slope characterizes the work-hardening behaviour at room temperature. In contrast, both cryogenic and high temperatures exhibit an increase in the slopes of the curves with noticeable bumps. Further examination of the microstructure has indicated that twinning deformation plays a vital role in shaping these observed deformation behaviours.

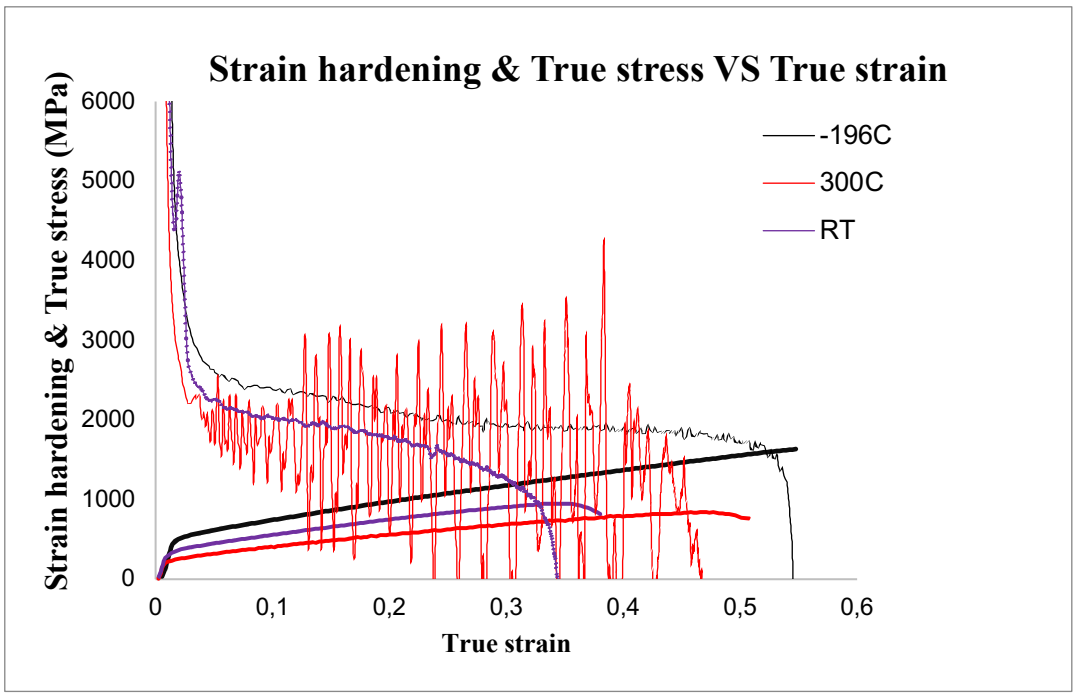

Figure 4.13 Strain hardening vs true strain samples deformed at 196℃, RT and 300℃.

Deformation Microstructure

The EBSD and ECCI images in figure at -196℃ reveal significant twin deformation, suggesting that the material has considerable twinning during deformation at cryogenic temperature. The EBSD images in figure 4.14 (a) show the presence of several multi-order twins and indicate multiple stages of twin formation in this low temperature. At room temperature, the figure 4.15(b) shows twinning continues to occur in the material however, the level of twin deformation is comparatively lower compared to that observed at -196℃. Despite this reduction in extensive twinning at room temperature, it is important not to overlook the presence of a significant number of twins. Even though there may be fewer twins formed, they still have a substantial impact on the material's deformation behavior and consequently influence its mechanical properties. At temperatures above 300℃, the figure 4.16 shows the presence of twin deformation both EBSD and ECCI analysis. EBSD observations indicate a significant reduction in the presence of twins compared to both -196℃ and RT. The decrease in twins at 300℃ indicates a decreased preference for dislocation and increased dominance of other deformation mechanisms in sample. The fraction of twins 16,2% is still good observation for providing a good support upon the deformation even at high temperature.

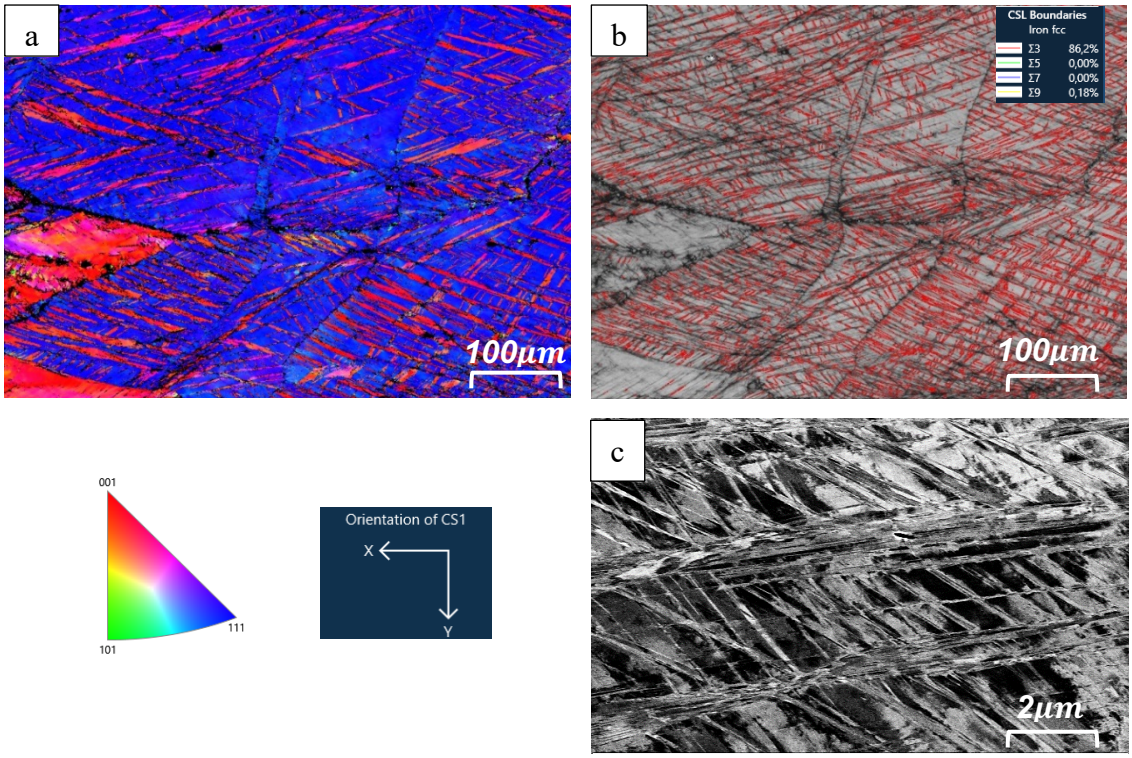

Figuree 4.14 shows sample deformed at -196℃ (a) EBSD IP shows the deformation twins red colour grains and blue represents the FCC austenite matrix. (b) EBSD BC and red colour represents the CSL Misorientation variation Σ3 60° <111>. (C) ECCI image showing deformation twins.

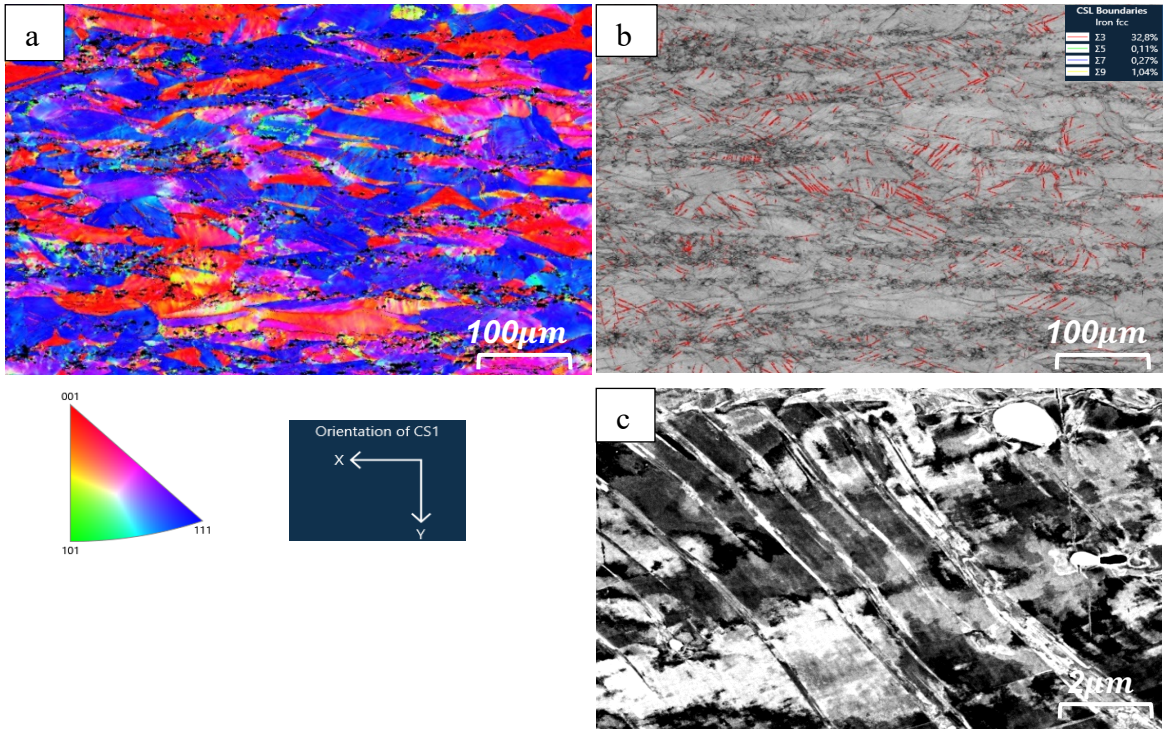

Figure 4. 15 shows sample deformed at RT (a) EBSD IP shows the deformation twins red colour grains and blue represents the FCC austenite matrix. (b) EBSD BC and red colour represents the CSL Misorientation variation Σ3 60° <111>. (C) ECCI image showing deformation twins

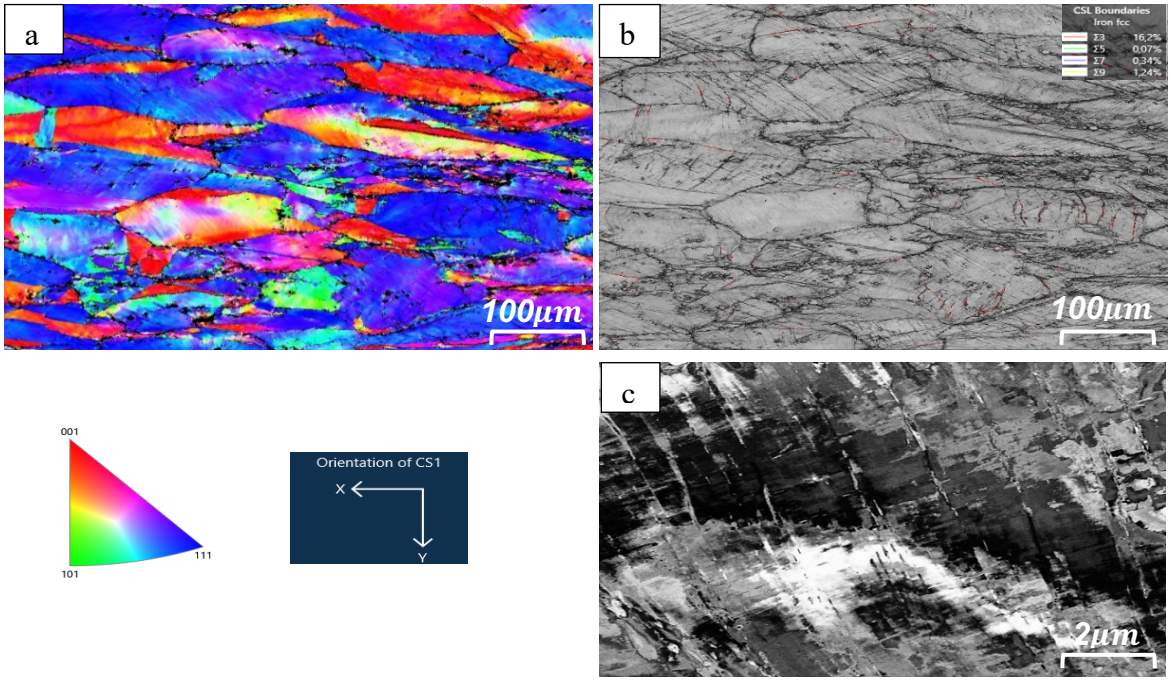

Figure 4.16 shows sample deformed at 300℃ (a) EBSD IP (b) EBSD BC and red colour represents the CSL Misorientation variation Σ3 60° <111>. (C) ECCI image showing deformation twin

4.6 HEA-TWP – 7

This HEA Ni-Fe-Cr-Mn-Mo-Co-Al-Cu has conducted uniaxial tension test at 196℃, RT and 300℃ with same strain rate. Both mechanical test results and microstructure analysis are discussed in this section. This alloy is a combination of 8 elements and designated as high entropy alloy because its configurational entropy is more than 1.5R.

Deformation hardening behaviour

when materials are deformed at cryogenic temperatures, they display greater strength and initiate the work-hardening effect below a range of 3000 MPa and very small area inside the curve until fracture as shown in figure 4.17. At room temperature and high-temperature deformations, there is a diminishing range of work hardening. Additionally, it is worth noting that plastic deformation appears to be more extensive for cryogenic temperatures compared to room temperature and high temperatures. The variation in temperature leads to the activation of different deformation behaviours that contribute to work hardening. The presence of serrations may indicate possibility of dynamic strain aging during deformation at high temperature. This phenomenon occurs from the onset of plastic deformation until fracture. However, further analysis is necessary to confirm whether dynamic strain aging takes place. The strain hardening effect is not showing any bump at plastic region in all cases and not surprisingly less elongation is recorded in tension tests.

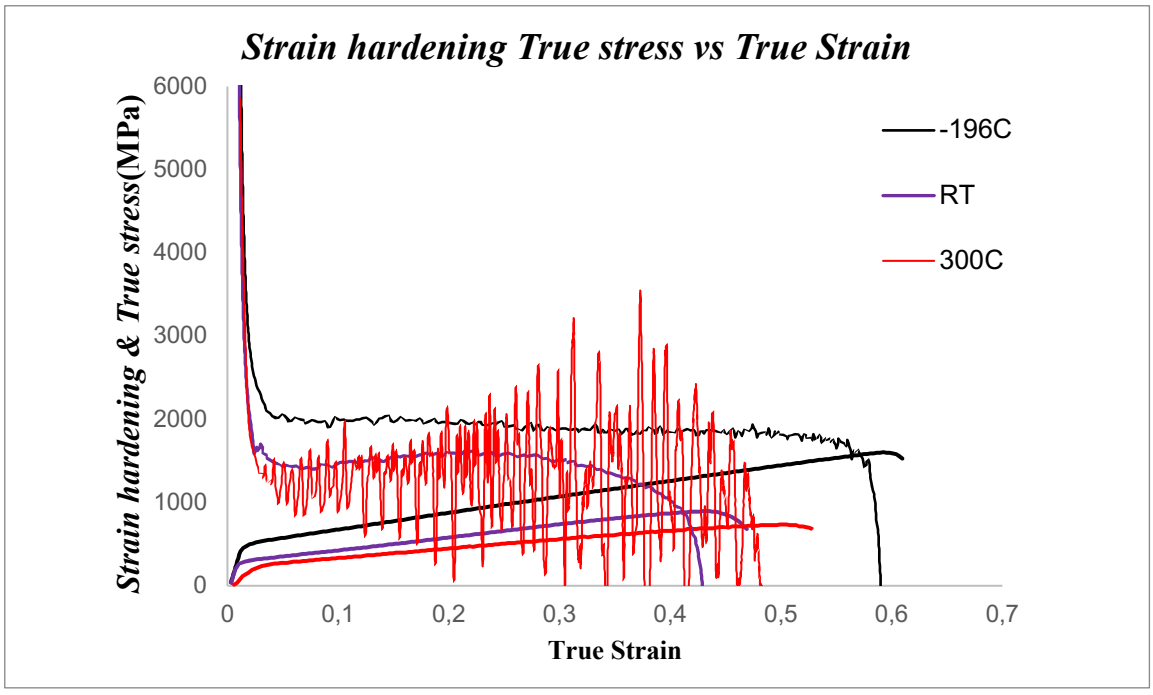

Figure 4. 17 Strain hardening vs true strain and temperature vs elongation curve at 196℃, RT and 300℃.

Deformation Microstructure

In Figure 4.18, the sample deformed at a temperature of -196°C. The EBSD and ECCI images provide evidence of the existence of a deformation twin that is larger in size when compared to other cases. These distinct twin exhibits increased length and thickness may impact the mechanical properties. However, it is noted that some grains do not display any twins and oriented in (001) and other types of strengthening deformation slip dislocation may happened. The observed presence of large twins in the deformation process also has a significant impact on elongation, resulting in an increased elongation compared to other alloys except TWP-1. Material deformed at room temperature is mentioned in figure 4.19 and twin deformation can still be observed. The volume of twin deformation is lower compared to -196°C and the size of each twin is larger. Despite this reduction in extent, it is important to note that a considerable number of twins are still present within the material. These twinning events play a crucial role in determining the overall deformation behavior and have an impact on the mechanical properties of the material under these conditions. As the temperature of deformation is raised to 300°C, there is minimal evidence of twinning observed both large twins and nano twins in figure 4.20, indicating a low density compared to deformations conducted at both -196°C and room temperature. Furthermore, mechanical testing results indicate that the elongation percentage closely aligns with the samples deformed at room temperature. However, it should be noted that in addition to twin deformation, dislocation slip can also serve as a mechanism contributing to these favorable mechanical properties. Fine/nano twins formed as shown in figure 4.20c will also contribute to the elongation. These fine/nano twins cannot be identified with EBSD analysis.

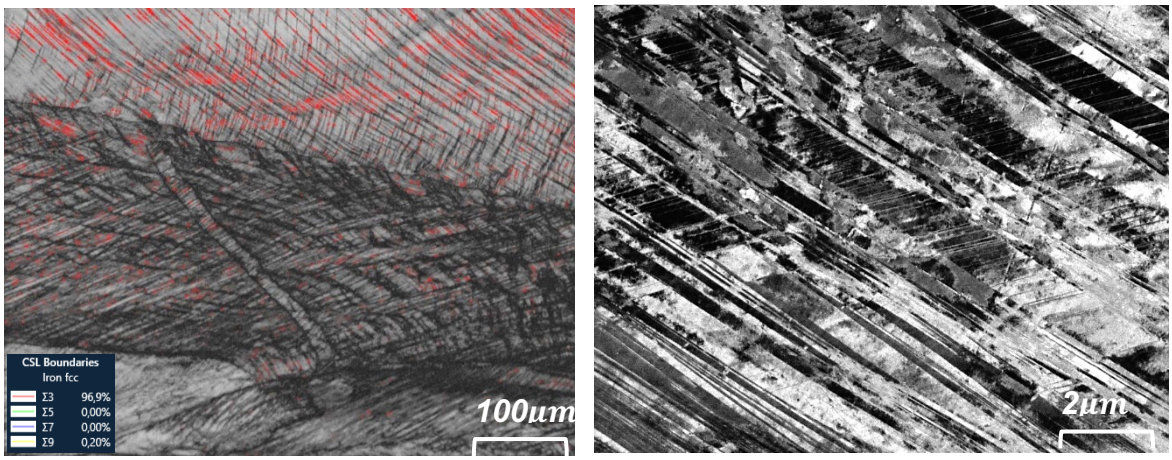

Figure 4.18 shows sample deformed at -196℃ (a) EBSD BC and red colour represents the CSL Misorientation variation Σ3 60° <111>**.** (b) ECCI image showing deformation twins.

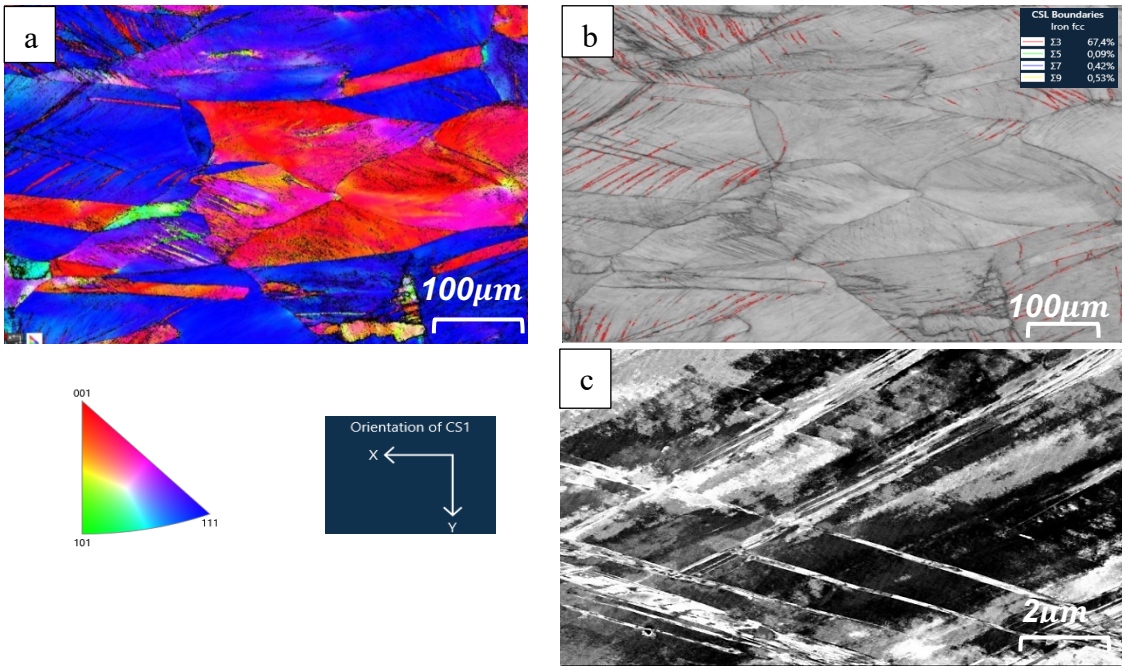

Figure 4.19 shows sample deformed at RT (a) EBSD IP shows the deformation twins red colour grains and blue represents the FCC austenite matrix. (b) EBSD BC and red colour represents the CSL Misorientation variation Σ3 60° <111>. (C) ECCI image shows deformation twins

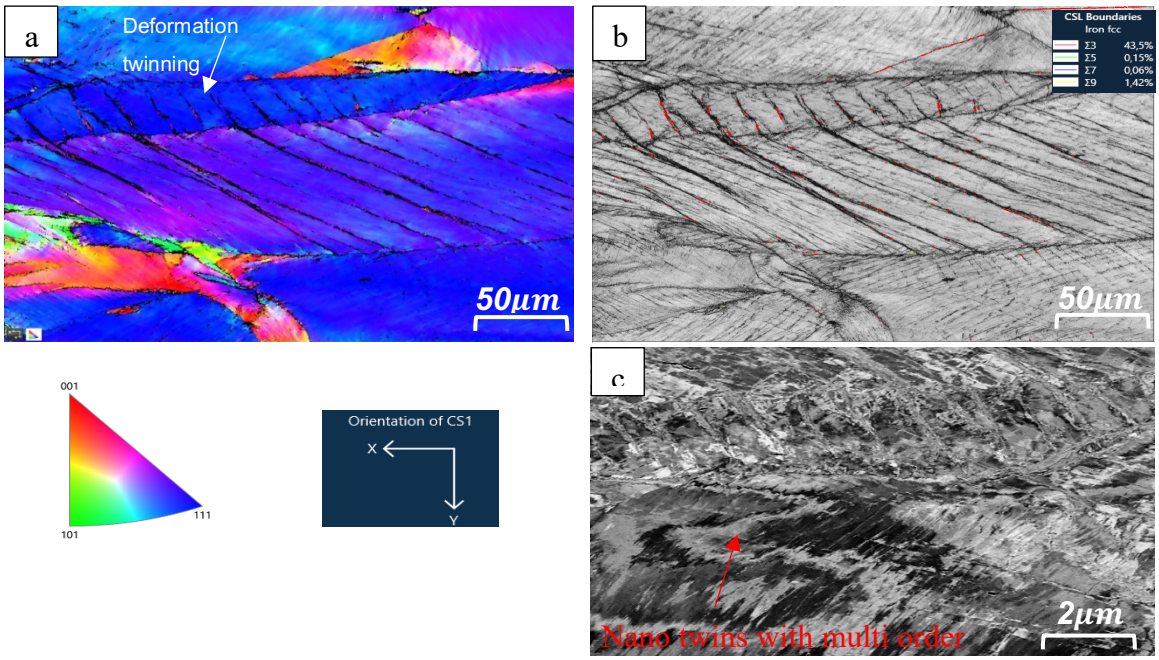

Figure 4.20 shows sample deformed at 300℃ (a) EBSD IP shows the deformation twins red colour grains and blue represents the FCC austenite matrix. (b) EBSD BC and red colour represents the CSL Misorientation variation Σ3 60° <111>. (C) ECCI image shows deformation twins

4.7 MEA-TWP – 10

This MEA Ni-Fe-Cr-Mn-Mo-N has conducted uniaxial tension test at 196℃, RT and 300℃ with same strain rate. Both mechanical test results and microstructure analysis are discussed in this section. The addition of Nitrogen can make impact in mechanical deformation behaviours of this alloy.

Deformation hardening behaviour

Both samples deformed at RT and -196℃ are showing same upward trend in plastic regime, that is indicating samples are showing good work hardening effect that reflects on mechanical properties. In the case of material deformed at 300℃, a quite same trend has followed but serration is appeared after yielding indicating that a possible dynamic strain aging may occur. The most interesting observation is all samples deformed with different temperatures exhibit same elongation as like the same deformation trend in figure 4.21. Twin deformation mechanism is common for all conditions as observed in both EBSD and ECCI analysis. As all curves are showing upward trend but it has less yielded that around 2000MPa and very small area from yielding to fracture. The mechanisms need to be further investigated.

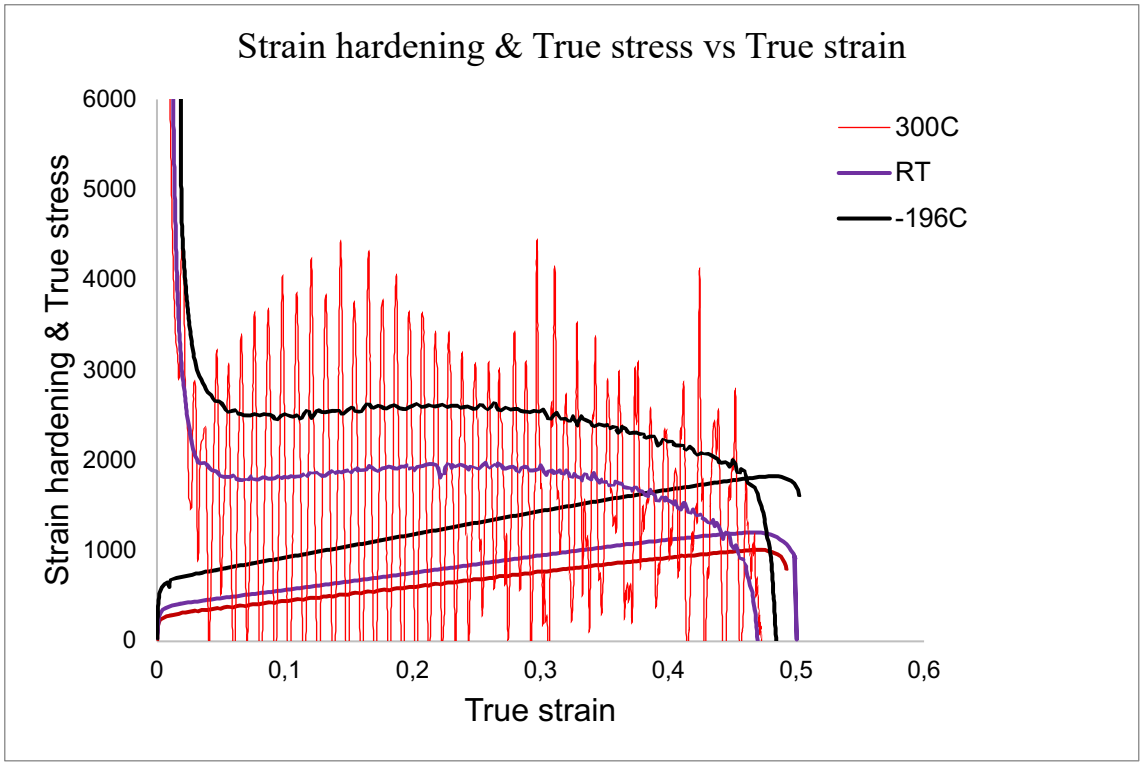

Figure 4.21 shows strain hardening vs true strain sample deformed at 196℃, RT and 300℃

Deformation Microstructure

At a temperature of -196℃, the EBSD and ECCI images in Figure 4.22 reveal the existence of a deformation twin with twin fraction of 76,1%. It is relatively limited as compared to previous instances. The substantial presence of multiple twins signifies that extensive formation of twinning has taken place during deformation at this specific temperature. Moving to room temperature, the presence of twins in elongated grains in Figure 4.23 is still observed, but the volume of twin deformation may be relatively lower compared to -196℃. However, despite the reduced extent of twin deformation, it is worth noting that there are still a considerable number of twins present in the material at RT. These twinning events significantly contribute to the overall deformation behavior and have an impact on the mechanical properties of the material at room temperature. Figure 4.23 (c) ECCI analysis clearly shows the twin bundles. As the temperature increases to 300℃, from EBSD and ECCI analysis Figure 4.24 there is very little deformation twin compared to both -196℃ and room temperature. This implies that at elevated temperatures, the material does not exhibit any micro twin formations. However, it is interesting to see the nano multi order twins in ECCI analysis, but it is not indexed by EBSD analysis.

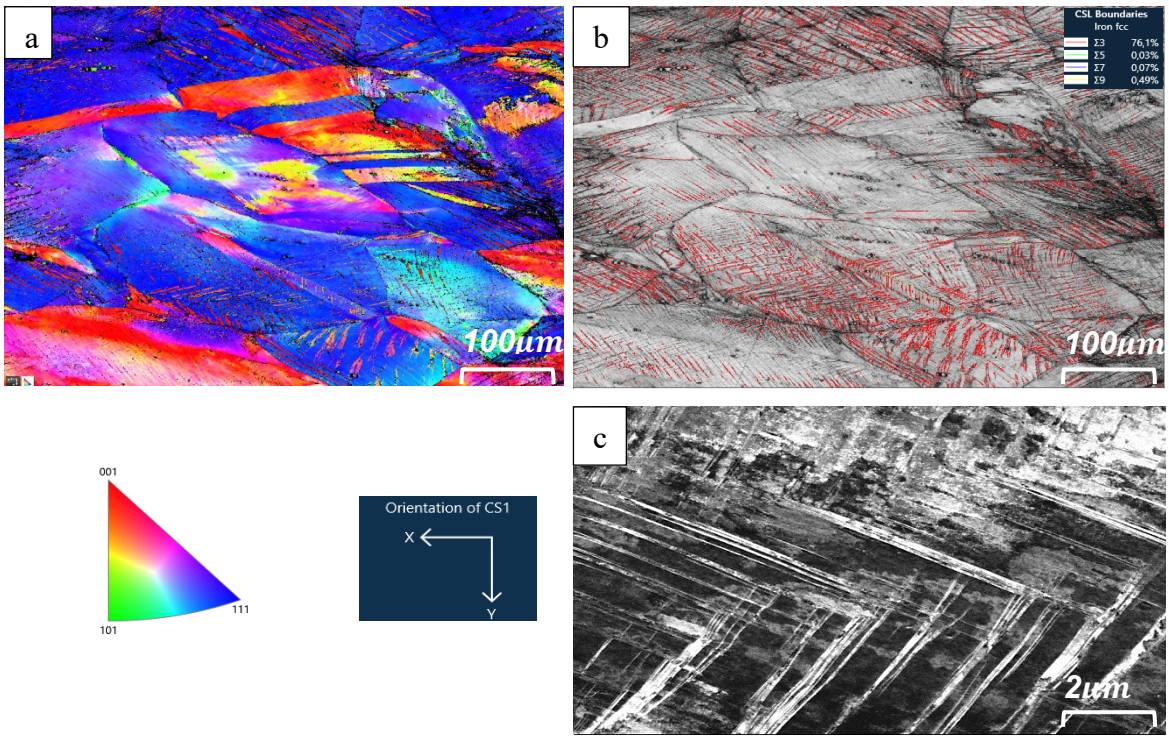

Figure 4. 22 shows sample deformed at -196℃ (a) EBSD IP shows the deformation twins red colour grains and blue represents the FCC austenite matrix. (b) EBSD BC and red colour represents the CSL Misorientation variation Σ3 60° <111>. (C) ECCI image showing deformation twins.

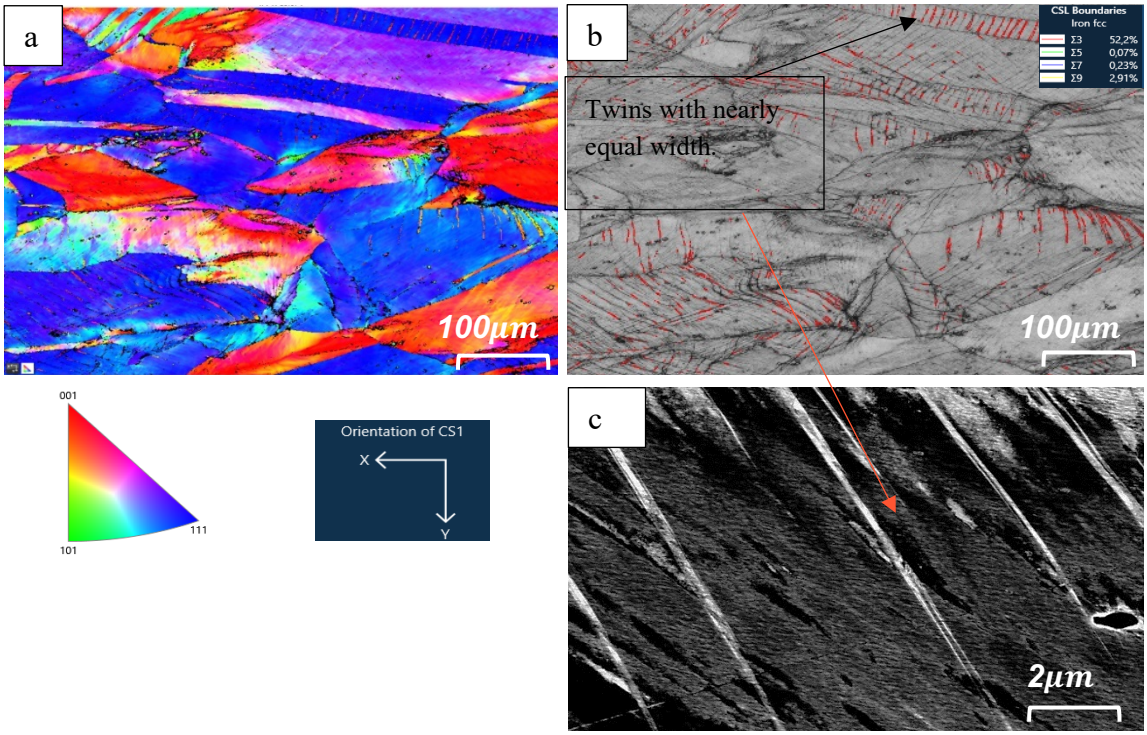

Figure 4. 23 shows sample deformed at RT (a) EBSD IP (b) EBSD BC and red colour represents the CSL Misorientation variation Σ3 60° <111>. (C) ECCI image is showing deformation twins.

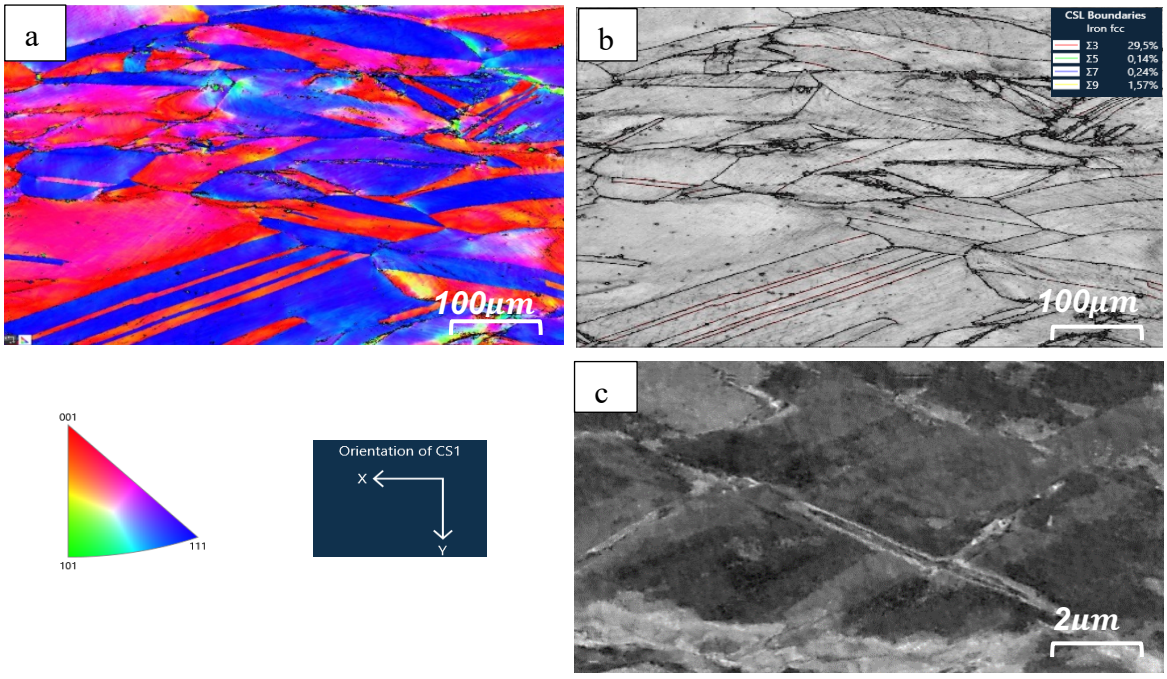

Figure 4. 24 shows sample deformed at 300℃ (a) EBSD IP (b) EBSD BC and red colour represents the CSL Misorientation variation Σ3 60° <111>. (C) ECCI image showing deformation twins.

4.8 MEA-TWP - 17

This MEA Ni-Fe-Cr-Mn-Mo-N alloy deformed uniaxial tension test at 196°C, RT and 300°C with same strain rate. Both mechanical test results and microstructure analysis are discussed in this section. The addition of Nitrogen can make impact in mechanical deformation properties.

Deformation hardening behaviour

All samples deformed at RT, 300°C and -196°C are showing same upward trend in plastic regime, that is indicating that the samples are showing good work hardening effect that reflects on the mechanical properties. In the case of material deformed at 300°C, quite same trend has followed but serration appears after the yielding and the end after strain of 12 %, indicating possibility of dynamic strain aging may occur. The most interesting observation is that all samples deformed with different temperatures exhibit bump in the range of true strain 20-25% as shown in figure 4.25. Twin deformation mechanism is common for all condition, that is observed in both EBSD and ECCI analysis. As all curves are showing upward trend but sample deformed at 196°C has more yielding and large area under the curve from yield to fracture part compared to other two cases.

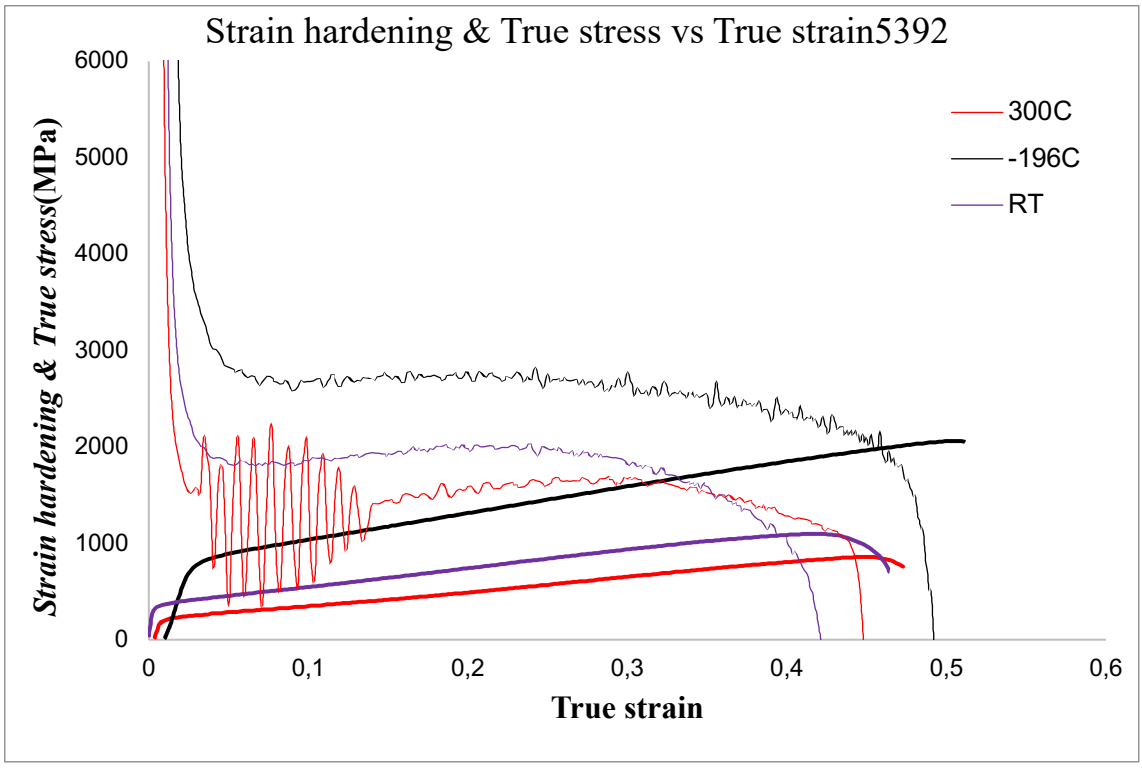

Figure 4. 25 Strain hardening vs true strain of samples deformed at 196°C, RT and 300°C

Deformation Microstructure

Figure 4.26 shows at -196°C, the presence of a large deformation twins and high density 82.3% are detected by EBSD and ECCI techniques and compare to all other deformation cases. At room temperature, Figure 4.27 depicts that some twin deformation is still observable, although in a smaller volume compared to -196°C. Nonetheless, the size of each twin is larger compared to other cases with the samples deformed at room temperature. Despite the reduced extent, a significant number of twins are present, playing a crucial role in deformation behaviour and influencing the material's mechanical properties. Twin formation and dislocation slip mechanisms both contribute to plastic deformation. At 300°C, minimal evidence of twinning is observed through EBSD and ECCI as mentioned in figure 4.28, indicating a low density compared to deformations at -196°C and room temperature. Mechanical testing reveals a similar elongation percentage to samples deformed at room temperature and cryogenic temperature. However, it is very surprising stable mechanical test results at samples deformed at all temperature.

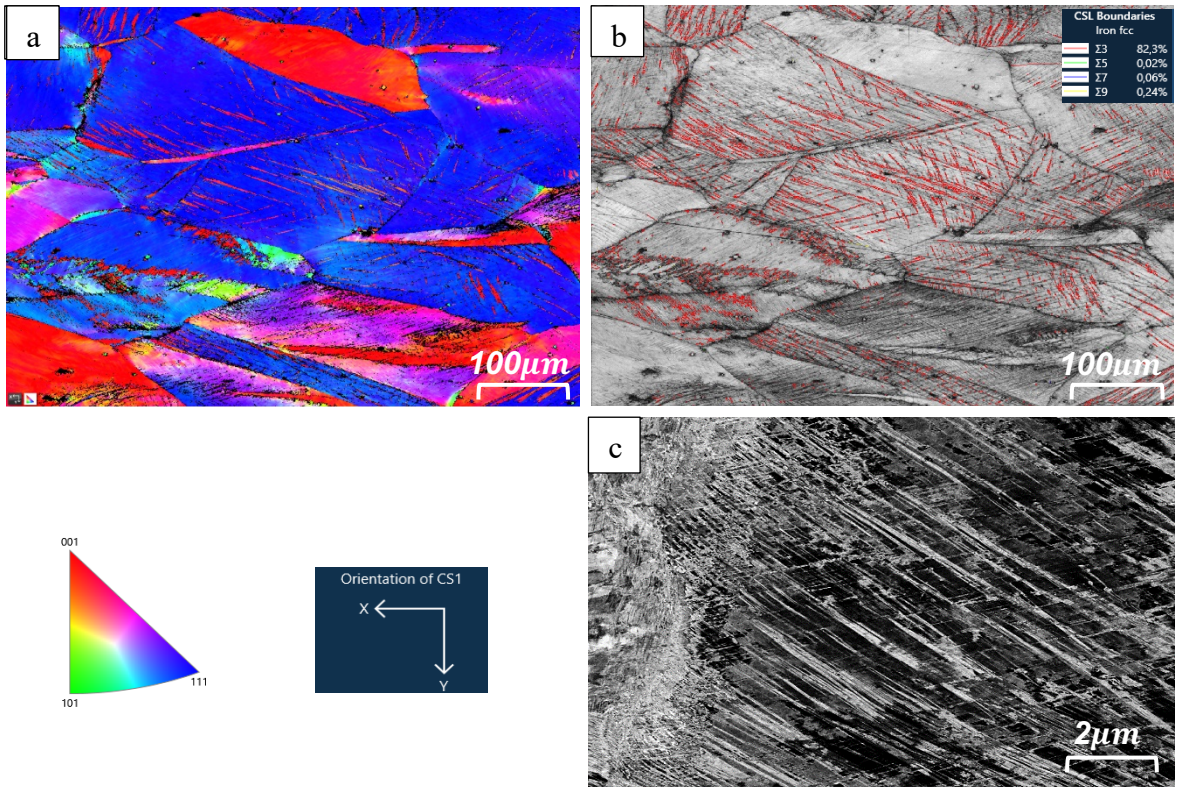

Figure 4. 26 shows sample deformed at -196°C (a) EBSD IP shows the deformation twins red colour grains and blue represents the FCC austenite matrix. (b) EBSD BC and red colour represents the CSL Misorientation variation Σ3 60° <111>. (c) ECCI image showing deformation twins.

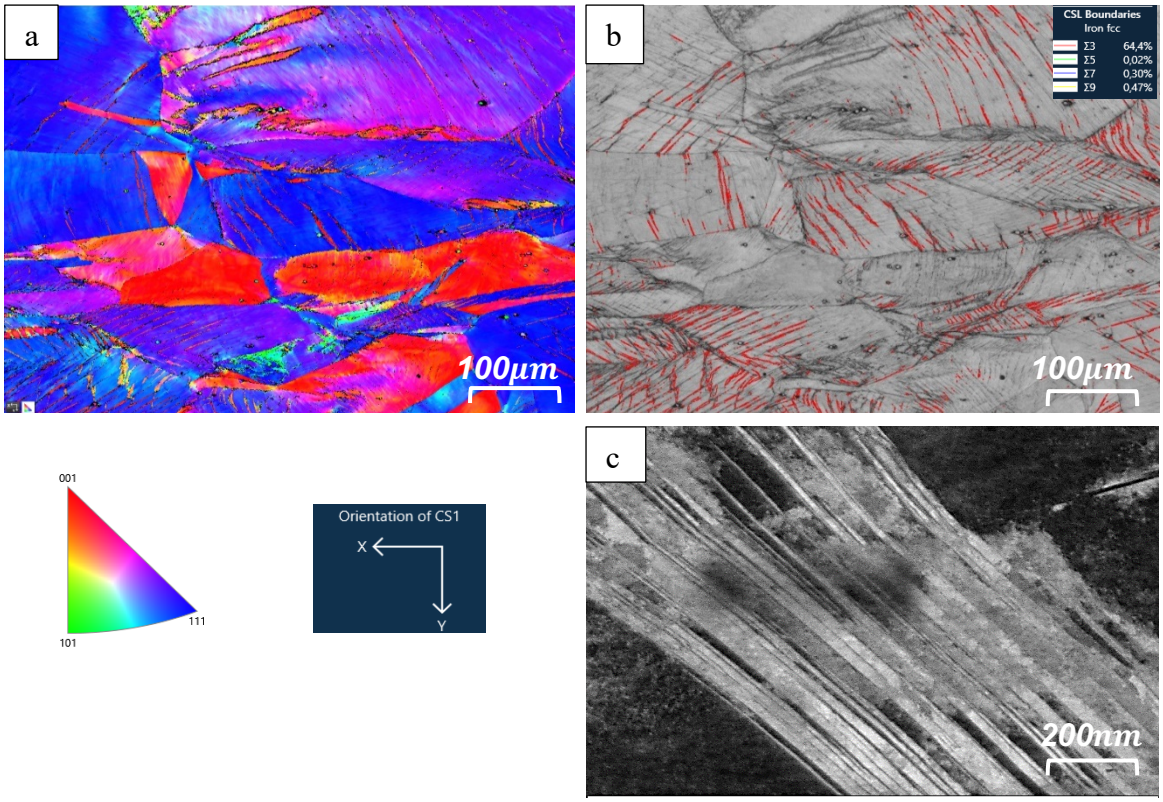

Figure 4.27 shows sample deformed at RT (a) EBSD IP (b) EBSD BC and red colour represents the CSL Misorientation variation Σ3 60° <111>. (C) ECCI image showing deformation twins.

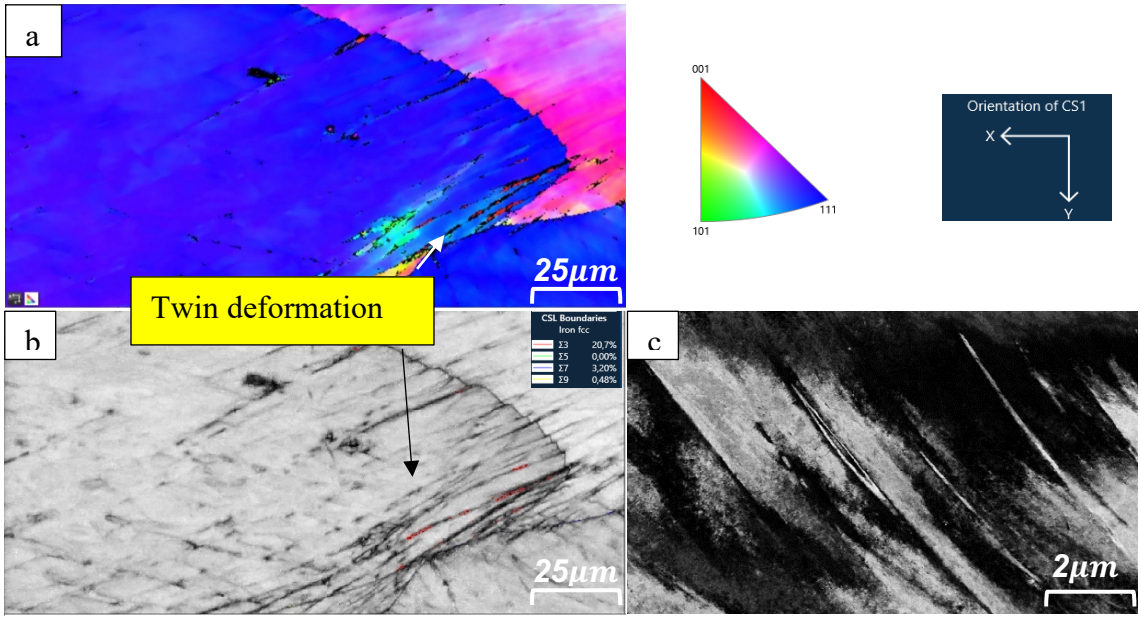

Figure 4. 28 shows sample deformed at 300℃ (a) EBSD IP (b) EBSD BC and red colour represents the CSL Misorientation variation Σ3 60° <111>. (C) ECCI image showing deformation twins.

5 General discussion

This chapter will specifically go through the composition, entropy, and temperature effect on the alloys upon deformation. The comparison will discuss for each case and go through the more detailed discussion coupled with literature study.

5.1 Temperature effect

The temperature has a considerable effect on the elongation behaviour of TWP-1 alloy. At -196℃, a significant increase in elongation approximately 89% is observed compared to deformation at room temperature and high temperature conditions. This suggests that the material exhibits improved ductility and strain hardening at cryogenic temperatures. At room temperature, the elongation TWP-1 declines, indicating reduced plastic deformation capability. However, at 300℃, there is a slight initial increase in elongation during the early stages of plastic deformation. Regarding the volume of twin deformation, more twins and multi-order twinning are observed at -196℃, indicating a higher density of twins 79.4% and at RT it is only 57,5% as mentioned in Table 5.1. However, as the temperature decreases, the density of twins and multi-twin deformations also increases. Interestingly, the multi order twin in Figure 5.1 for TWP-1 at -196℃ dominates the more strength and elongation properties. At 300℃, no micro twins are identified by the EBSD technique, and only a few twins are recorded using ECCI. This suggests that slip deformation may play a significant role in the plastic deformation of the material at higher temperatures.

Table 5.2 Shows the fraction of twins detected by EBSD analysis.

MEA	Deformation temperature	Distance from fracture(mm)	Twin fraction (%)
TWP-1	(- 196℃)	1	79,4
	RT	1	57,5
TWP-10	(- 196℃)	1	76,1
	RT	1	52,2

The Aztec crystal software is used to identify the percentage of fraction mentioned in table 5.1. The extent of twin deformation is influenced by the stacking fault energy. Materials with a lower SFE exhibit greater levels of twin deformation compared to those at different temperatures. It is widely acknowledged that the presence of martensite transformation occurs when the stacking fault energy falls below 20 mJ/m2 in FCC alloys. In the medium range of SFE, typically between 20 to 40 mJ/m^2, formation of deformation twin can be observed. On the other hand, plastic deformation predominantly takes place through dislocation slip when the SFE exceeds 40 mJ/m^2 [18]. This study aligns with existing research by confirming that the deformation twin volume fraction decreases as temperature increases. The microstructural analysis also confirmed that the alteration of the deformation mechanism transitions from twin deformation to slip deformation.

5.2 Composition effect on mechanical properties-Effect of Nitrogen

The addition of nitrogen has a significant effect on the mechanical properties that observed in TWP-17 alloys at room temperature and high temperature. Main difference between the two materials is the addition of 0.93% nitrogen in TWP-17 as mentioned in table 3.4. Addition of nitrogen transformed the TRIP effect of alloy into a TWIP effect alloy, leading to improved strength and elongation. In the nitrogen-doped HEA, the high yield strength is primarily derived from friction stress through interstitial strengthening effects, while the enhanced ductility results from its ability to retain a high strain-hardening capacity due to successive onset of dislocation accumulation and deformation twinning as the studies proved [19]. According to Yu Han's study, it is also consistent with our statement that the addition of nitrogen can enhance the strain hardening effect in both room temperature and high-temperature nitrogen-doped alloys [19]. These alloys exhibit superior strength and elongation compared to low-temperature conditions without nitrogen doping.

The microstructure investigations using EBSD and ECCI were conducted. At -196℃, TWP-1 demonstrated superior elongation of 89.4% with a higher twin density and activated multi-order twin deformation mechanism. In contrast, TWP-17 exhibited an elongation of 67% with lower twin volume fraction and fewer multi-twin systems activated. However, at RT and 300℃, TWP-17 showed higher elongation 59% and 56.4% respectively, compared to TWP-1 MEA with 51% and 46.1%. Interestingly, microstructure analysis revealed that TWP-17 exhibited large and thick twins, while TWP-1 had higher twin densities. The addition of nitrogen increased planar dislocation and suppressed cross slip in TWP-17. At high temperatures, TWP-17 exhibited EBSD-indexed twin deformation, while TWP-1 did not exhibit any twins indexed with EBSD. In summary, adding nitrogen increased the elongation at both room and high temperatures but did not show any effect at cryogenic temperatures. Microstructure analysis indicated that nitrogen could enhance twin deformation and improve the mechanical properties of the alloys [17].

5.3 Entropy Effect –No of elements and composition effect

The primary focus in high-medium entropy alloys lies in maximizing the entropy effect. When entropy increases, a disorder solid solution is formed, which prevents the formation of intermetallic compounds and promotes the formation of only FCC solid solutions. The number of elements and composition play a significant role in increasing the entropy effect.

In the case of TWP-6 and TWP-7 alloys, they exhibit a high entropy of mixing compared to other alloys. These alloys consist of a larger number of alloying elements. Additionally, TWP-7 includes the addition of Cu. Figure 5.1(a) illustrates the configurational entropy increases with the number of elements. This phenomenon guarantees the desired entropy effect, leading to the formation of a disorder solid solution. Figure 5.1(b) displays the elongation versus temperature plot for TWP-6 and TWP-7 alloys. By introducing Cu into TWP-7, the plot demonstrates an improvement in the material's elongation property at all deformation temperature. From Figure 5.1(b) no significant improvement in the elongation TWP-6 has 50.1% & TWP-7 52.6% at high temperature and deformation twins also contribute for plastic deformation detected by ECCI and EBSD with same position as shown in figure 5.2(c) & (f). The results showed that TWP-7 had a higher elongation rate of 84% compared to TWP-6, which only reached an elongation rate of 72.9%. This difference can be attributed to the presence of a greater twin density and activation of multiple twin deformation mechanisms in TWP-7. Interestingly, similar trends were observed at room temperature for both samples during deformation. Upon microstructural analysis, it was observed in figure 5.2 (e) that the TWP-7 sample exhibits a complex system of multiple order twins with bundles located within the spaces between them.

Previous research has demonstrated that increasing the quantity of elements has a significant impact on reducing stacking fault energy, consequently leading to the formation of twin induced plasticity [20,21,22].

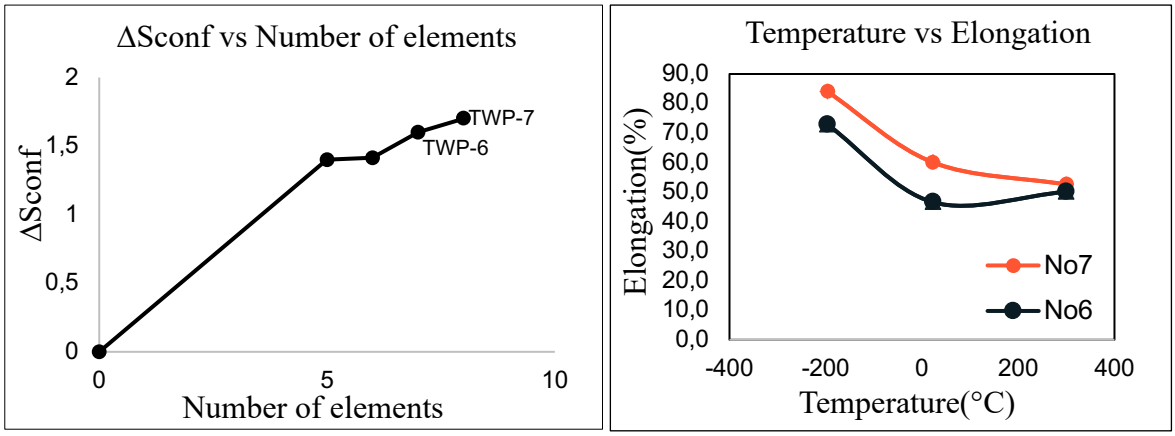

Figure 5.1 Graphical representation of ΔSconf vs Number of elements & Temperature vs Elongation Of TWP-6 and TWP-7.

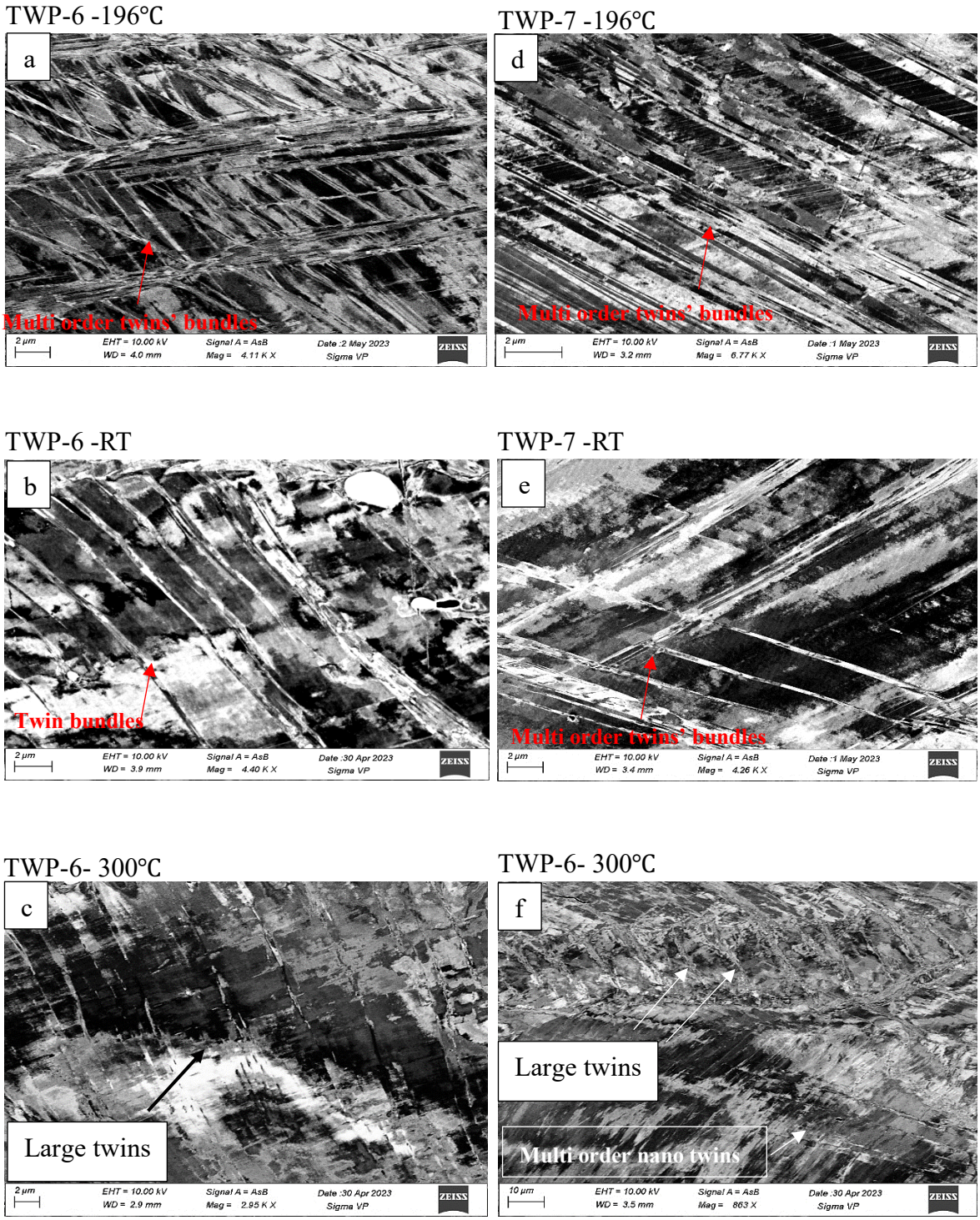

Figure 5.2 ECCI microstructure analysis of TWP-6 & TWP-7 sample deformed at -196°C, RT and 300°C.

6 Conclusion

The Ni-Fe-Cr-Mn-Mo high-entropy alloys demonstrate outstanding mechanical properties characterized by a unique combination of high strength and elongation. This remarkable behaviour can be attributed to the twin-induced plasticity (TWIP) mechanism, which plays a crucial role in promoting strength and ductility.

- The testing temperature significantly influences the deformation twinning process, with cryogenic temperatures leading to a higher density of large and nano twin deformation with multi-order due to the material with low stacking fault energy.

- Chemical composition and the number of elements present in the alloy also play a vital role in determining the entropy effect, which subsequently affects the mechanical properties.
- The addition of Cu and N can reduce the SFE and promote the twin deformation that can improve the strength and elongation especially materials deformed in RT and high temperature.

The study of Ni-Fe-Cr-Mn-Mo high-entropy alloys offers valuable insights into the design and development of advanced materials with exceptional mechanical performance. Further research and exploration in this field hold promising prospects for tailoring high-entropy alloys with tailored properties for a wide range of applications, including structural and functional materials in various industries.

7 Reference

1) Gao, M.C., Yeh, J.-W., Liaw, P.K., Zhang, Y. (Eds.) (2016). High-Entropy Alloys Fundamentals and Applications. Springer International Publishing. ISBN 978-3-319-27011-1 (Print), ISBN 978-3-319-27013-5 (eBook). DOI: 10.1007/978-3-319-27013-5.
2) Lyu, Z., Fan, X., Lee, C., Wang, S.-Y., Feng, R., & Liaw, P.K. (Year). Fundamental understanding of mechanical behavior of high-entropy alloys at low temperatures: A review. Journal Name, Volume (Issue), Page range. DOI: 10.1557/jmr.2018.273.
3) Zhang Y, Zhou YJ, Lin JP, Chen GL, Liaw PK (2008) Solid-solution phase formation rules for multi-component alloys. Adv Eng Mater 10(6):534–538. doi:10.1002/adem.200700240
4) ang X, Zhang Y (2012) Prediction of high-entropy stabilized solid-solution in multicomponent alloys. Mater Chem Phys 132(2–3):233–238. doi: 10.1016/j.matchemphys.2011.11.021
5) Guo S, Ng C, Lu J, Liu CT (2011) Effect of valence electron concentration on stability of fcc or bcc phase in high entropy alloys. J Appl Phys 109(10):103505. doi:10.1063/1.3587228
6) Reed-Hill RE, Abbaschian R (1994) Physical Metallurgy Principles, 3rd edn. PWS Publishing Company, Boston, pp xiii–xv 2.
7) Cahn RW, Haasen P (eds) (1983) Physical metallurgy, 3rd revised and enlarged ed. Elsevier Science publishers BV, Amsterdam, pp 1–35.
8) Feng J, Tang Y, Liu J, Zhang P, Liu C and Wang L (2022), Bio-high entropy alloys: Progress, challenges, and opportunities. Front. Bioeng. Biotechnol. 10:977282. doi: 10.3389/fbioe.2022.977282.
9) Multistage work hardening assisted by multi-type twinning in ultrafine-grained heterostructural eutectic high-entropy alloys
10) Shi, P., Zhong, Y., Li, Y., Ren, W., Zheng, T., Shen, Z., Yang, B., Peng, J., Hu, P., Zhang, Y., Liaw, P. K., Zhu, Y. (2020). Multistage work hardening assisted by multi-type twinning in ultrafine-grained heterostructure eutectic high-entropy alloys. Materials Today
11) Khan, T. Z., Kirk, T., Vazquez, G., Singh, P., Smirnov, A. V., Johnson, D. D., Youssef, K., & Arróyave, R. (2022). Towards stacking fault energy engineering in FCC high entropy alloys. Acta Materialia, 224,
12) Hargather, C. Z. (2022). Efficient First-Principles Methodologies for Calculating Stacking Fault Energy in FCC and BCC High-Entropy Alloys. In: Book Title, Chapter, First Online: 03 January 2022 https://doi.org/10.1007/978-3-030-77641-1
13) Khan, T. Z., Kirk, T., Vazquez, G., Singh, P., Smirnov, A. V., Johnson, D. D., Youssef, K., & Arróyave, R. (2022). Towards stacking fault energy engineering in FCC high entropy alloys. Acta Materialia, 224, 117472.

14) K. Momma, F. Izumi, IUCr, VESTA 3 for three-dimensional visualization of crystal, volumetric and morphology data. J. Appl. Crystallogr. 44(6), 1272–1276 (Dec. 2011)
15) Rafaja, D., Ullrich, C., Motylenko, M., & Martin, S. (2020). Microstructure Aspects of the Deformation Mechanisms in Metastable Austenitic Steels. In Springer Series in Materials Science (Vol. 298)
16) Huang, H., Li, X., Dong, Z., Li, W., Huang, S., Meng, D., Lai, X., Liu, T., Zhu, S., & Vitos, L. (2018). Critical stress for twinning nucleation in CrCoNi-based medium and high entropy alloys. Acta Materialia, 149, 388-396.
17) Chung, K. S., Yiu, P. M., Hung, T. F., & Shek, C. H. (2021). Strengthening and deformation mechanism of a Fe20Co20Cr20Mn20Ni20 high entropy alloy with high nitrogen content. Journal of Alloys and Compounds, 871, 159587. https://doi.org/10.1016/j.jallcom.2021.159587
18) Zhang, X., Lu, X., Zhao, J., Kan, Q., Li, Z., & Kang, G. (2022). Temperature effect on tensile behaviour of an interstitial high entropy alloy: Crystal plasticity modelling. International Journal of Plasticity, 150, 103201.
19) Han, Y., Li, H., Feng, H., Li, K., Tian, Y., & Jiang, Z. (2021). Simultaneous enhancement in strength and ductility of Fe50Mn30Co10Cr10 high-entropy alloy via nitrogen alloying. Journal of Materials Science & Technology, 65, 210-215.
20) Lee C, Yeh JW (2013) Study on deformation behaviors of equimolar alloys from Ni to CoCrFeMnNi. Master's thesis, National Tsing Hua University
21) Porter DA (1992) Phase transformations in metals and alloys. Chapman & Hall, New York,pp 110–142
22) Zaddach AJ, Niu C, Kock CC, Irving DL (2013) Mechanical properties and stacking fault energies of NiFeCrCoMn high-entropy alloy. J Appl Meteorol 65:1780–1789

Appendix – Part-1

A.1 EDX analysis after heat treatment

A.1.1 No-3 solution treated condition.

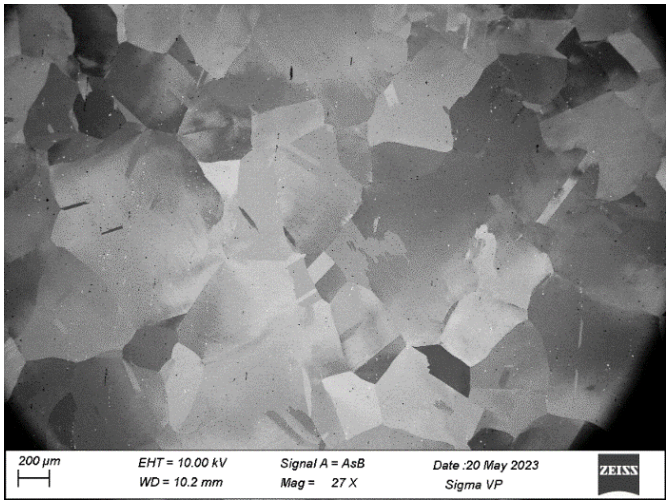

Figure A.1 1 Low magnification BSE image ST condition.

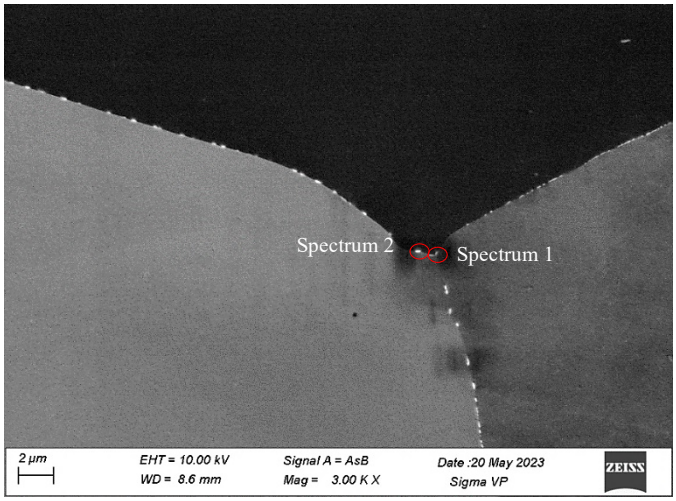

Figure A.1 2 Delta phases present at grain boundaries.

Atomic %	Si	Ti	Cr	Fe	Ni	Nb
Spectrum 1	0,75	6,92	16,32	15,49	28,95	31,58
Spectrum 2	0,49	4,9	18,96	15,74	39,33	20,58

Table A.1 1 EDS point analysis of precipitate in Figure A.1 3

A.1.2 No-3 Aged condition

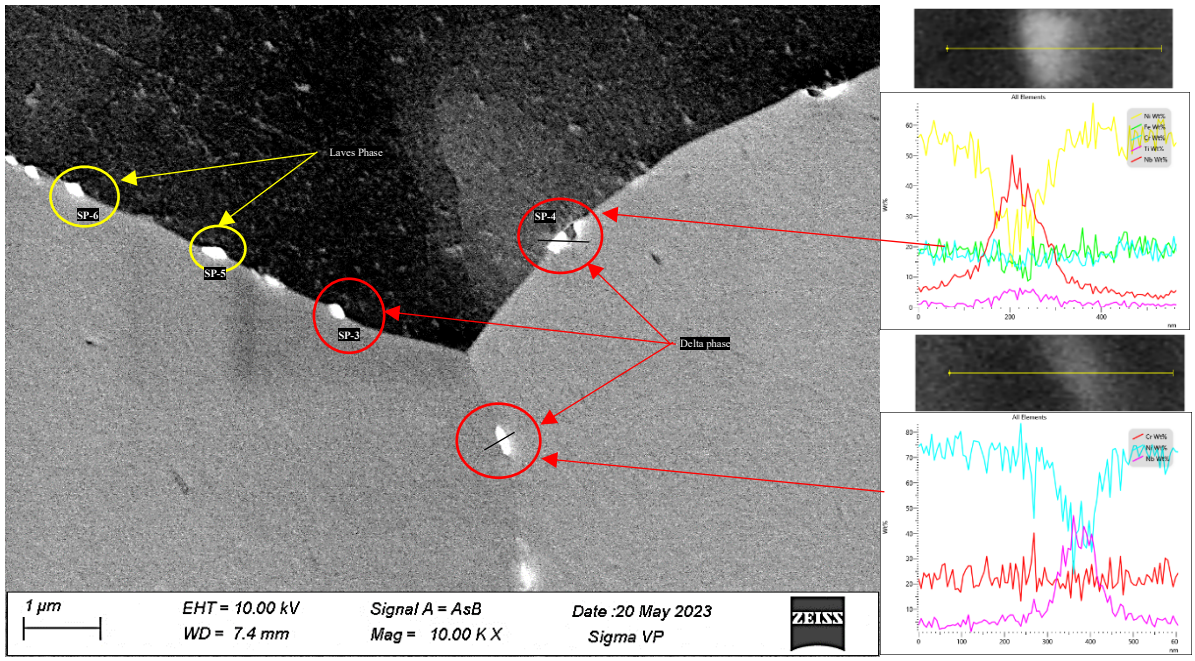

Figure A.1 4 Delta and laves phases present at grain boundaries identified by EDS line scan.

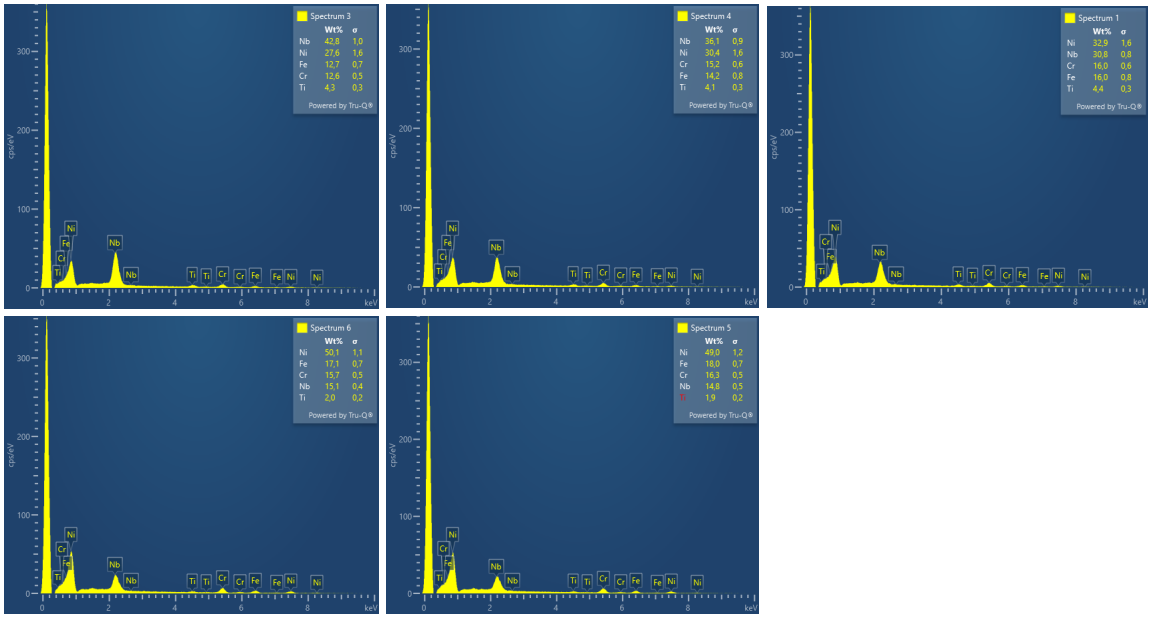

Figure A.1 5 EDS point analysis of chemical composition of each spectrum

A.1.3 No-2 Aged condition

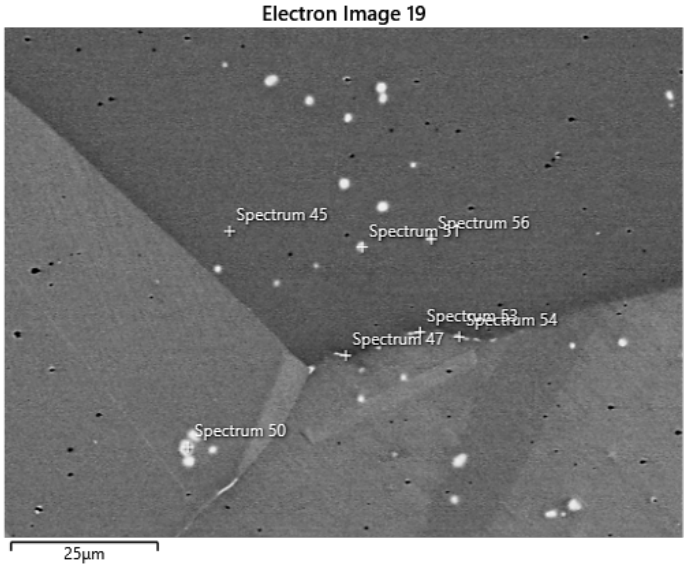

Figure A.1 6EDS point analysis composition analysis

Atomic %	Ti	Cr	Fe	Ni	Nb	Si	Al	C
Spectrum 45	1,21	22,82	20,27	52,62	2,53	0,55		
Spectrum 47	0,98	21,3	18,98	46,89	7,21	3,39	1,24	
Spectrum 50	12,74				48,98			38,28
Spectrum 51	7,91	10,22	8,1	18,34	39,21			16,22
Spectrum 53	5,33	22,05	20,03	51,62	0,98			
Spectrum 54	1,02	21,27	19,22	47,73	7,85	2,92		
Spectrum 56	1,15	22,34	19,84	51,9	2,53	1,52	0,72	

Table A.1 2 chemical composition of measured points

A.2 Fractography No-3

A.2.1 Deformed at Room temperature - 10^{-1}

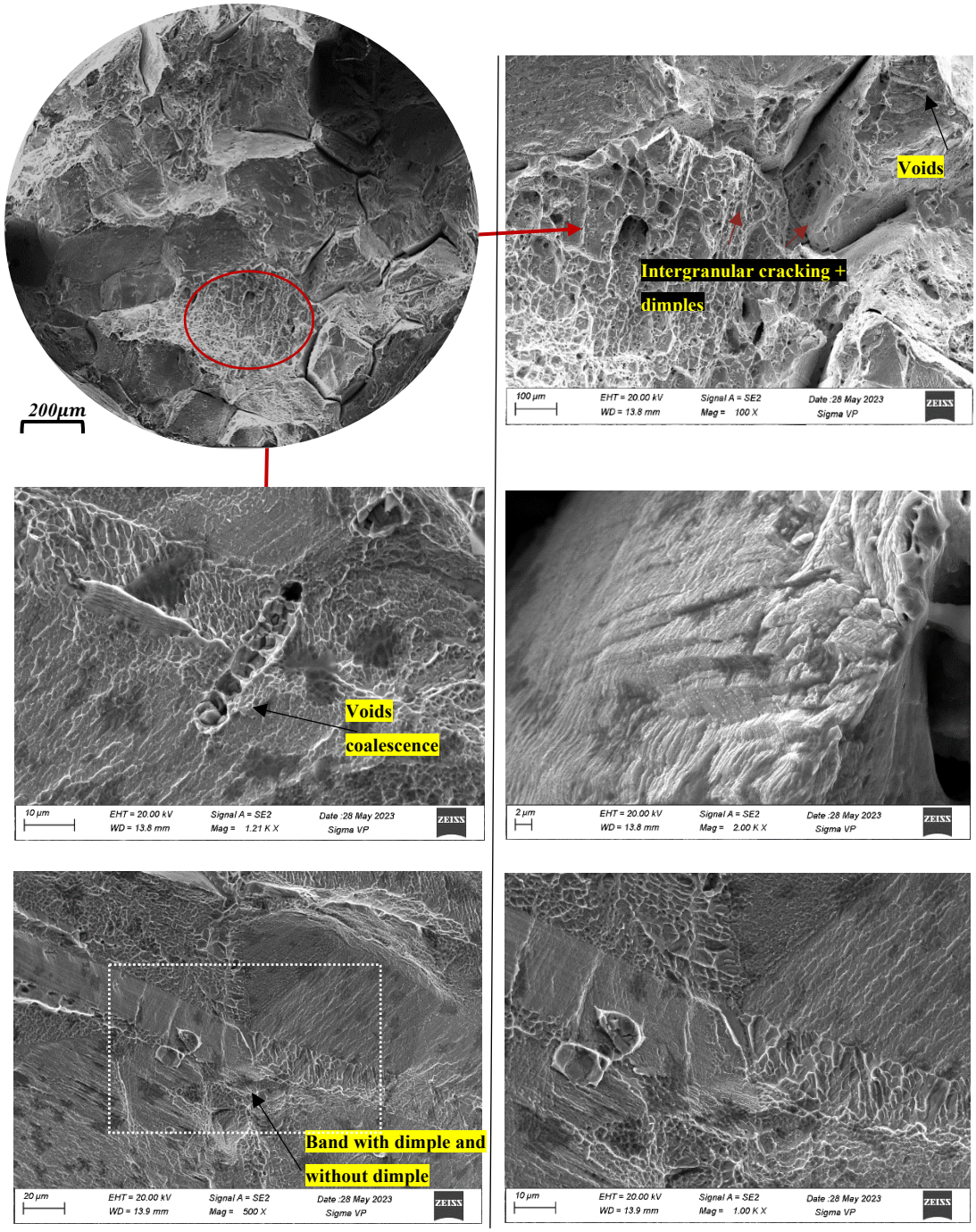

Figure A.2 1 Fractography results at center and edge.

A.2.2 Deformed at 650℃- 10^{-1}

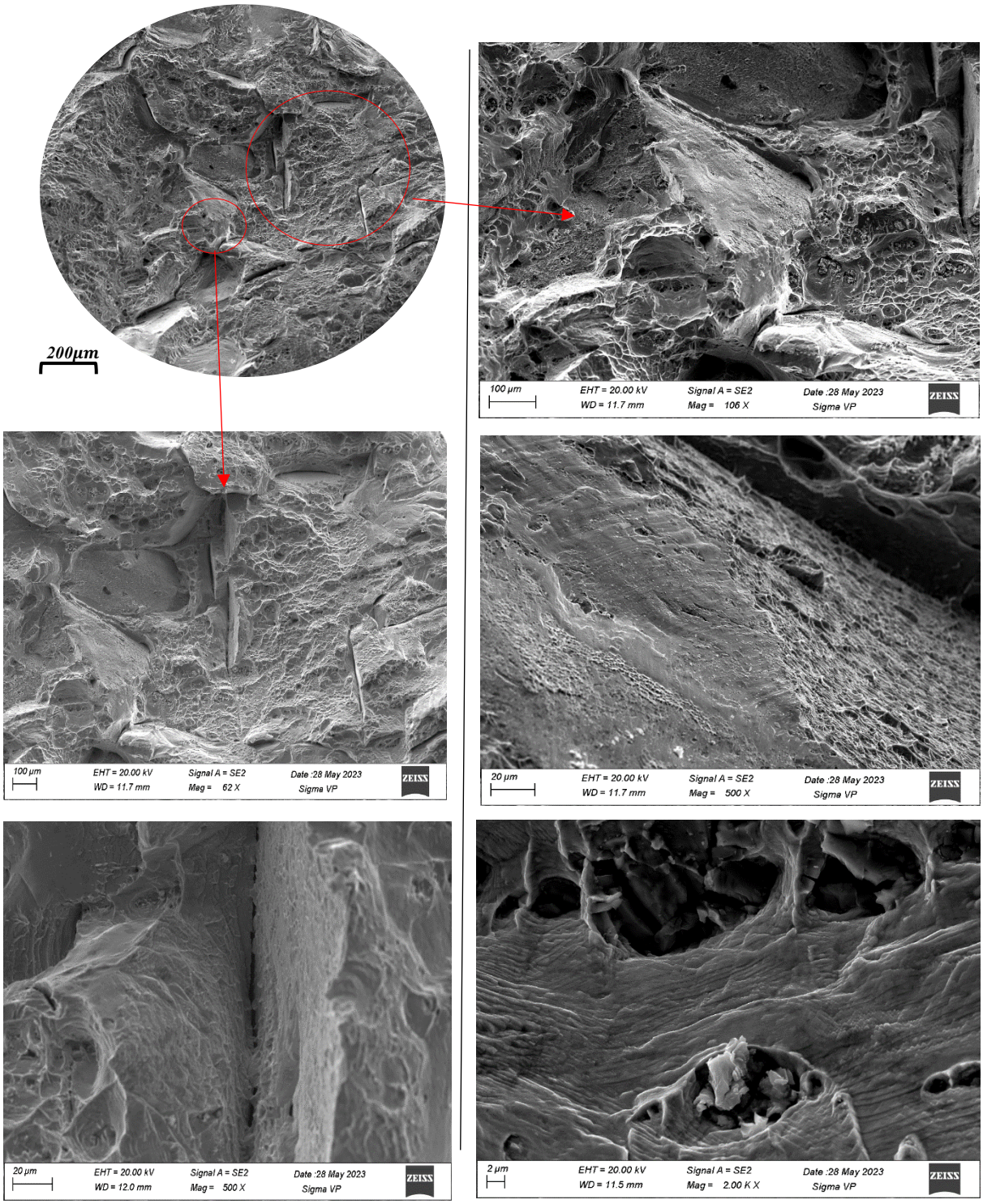

Figure A.2 2 Fractography results at center and edge.

A.2.3 Deformed at 750℃ strain rate 10^{-1}

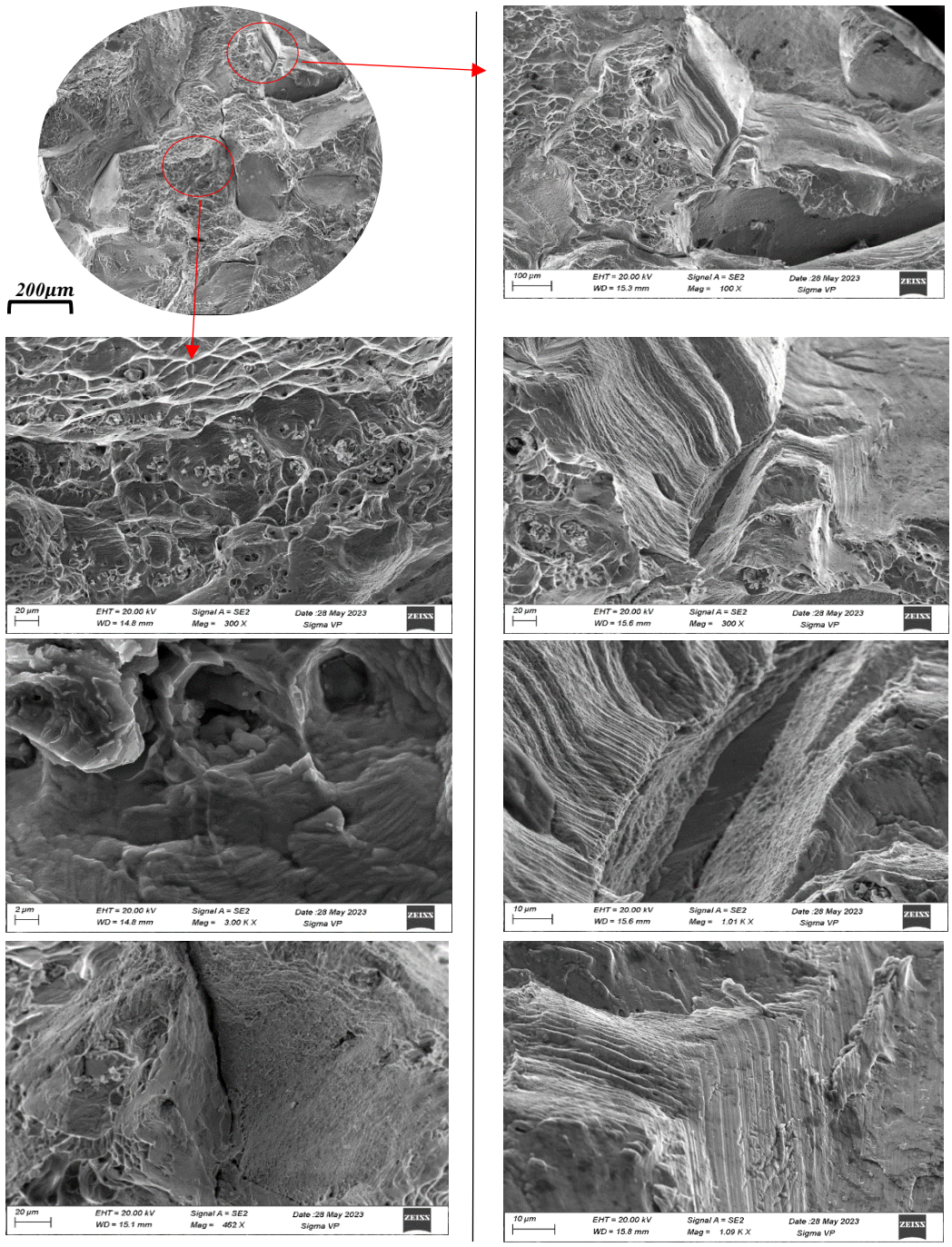

Figure A.2 3 Fractography results at center and edge.

A.2.4 Deformed at 750℃ strain rate 10^{-3}

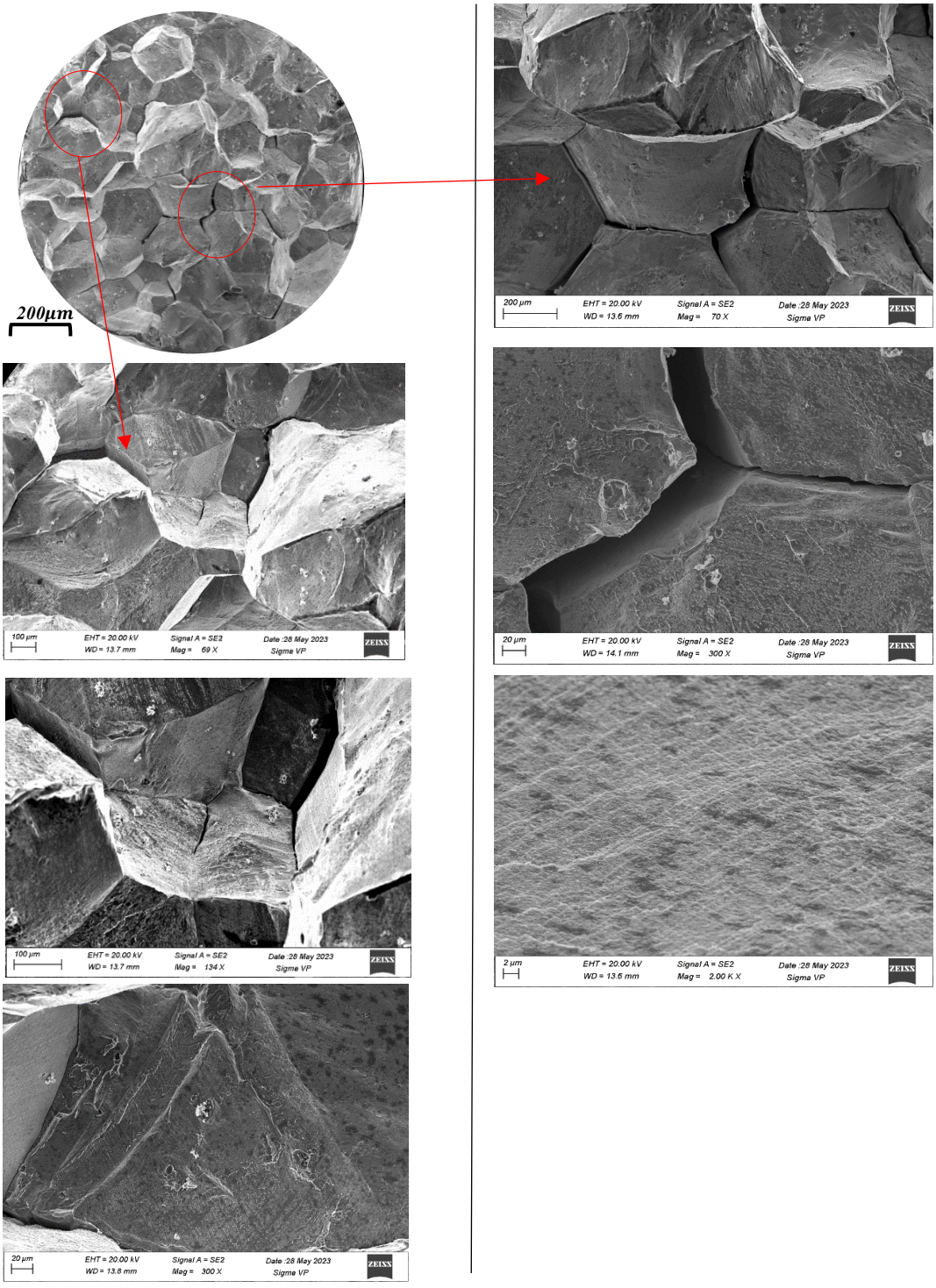

Figure A.2 4 Fractography results at center and edge.

A.2.5 Deformed at Room temperature strain rate 10^{-4}

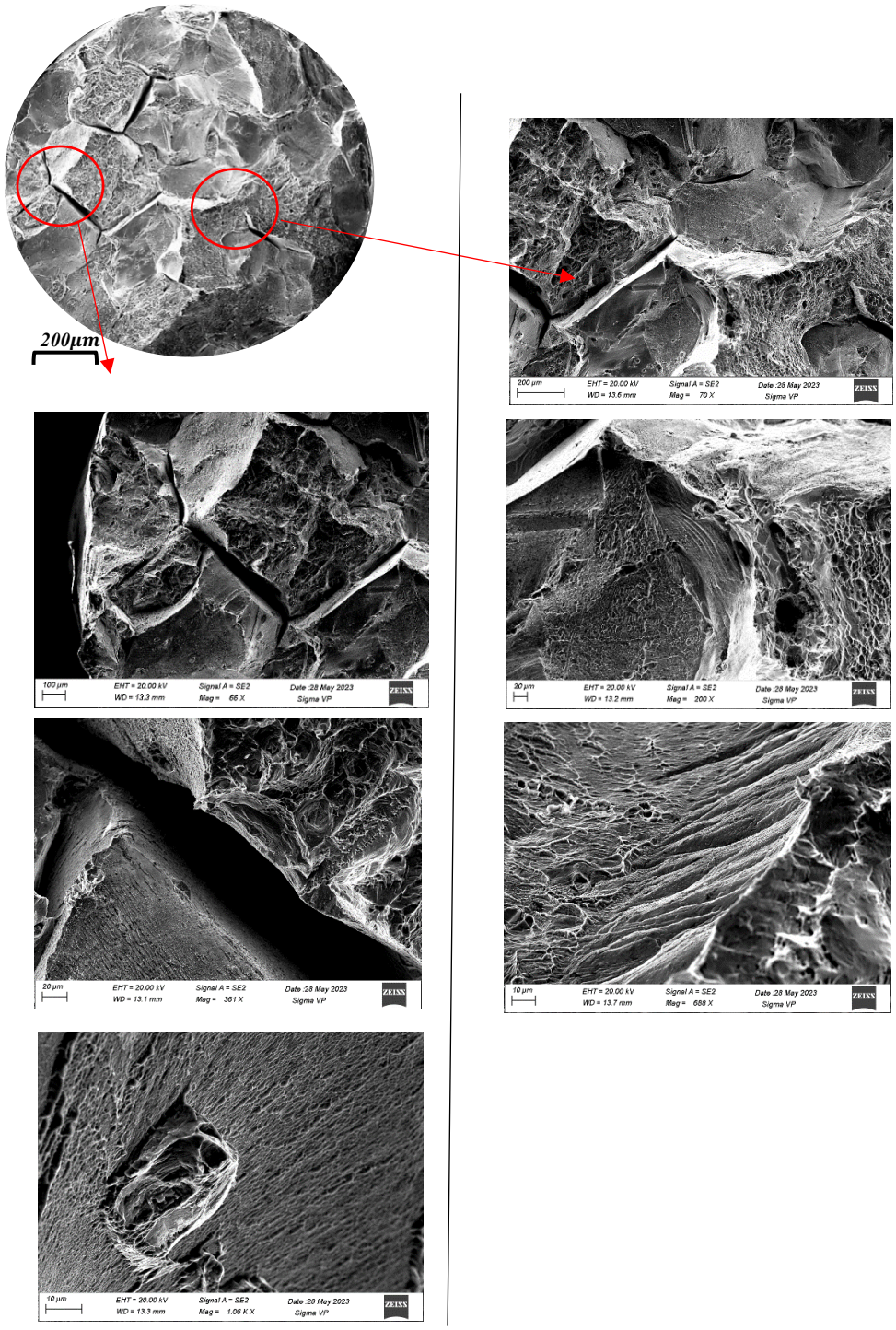

Figure A.2 5 Fractography results at center and edge.

A.2.6 Deformed at 650℃ strain rate 10^{-4}

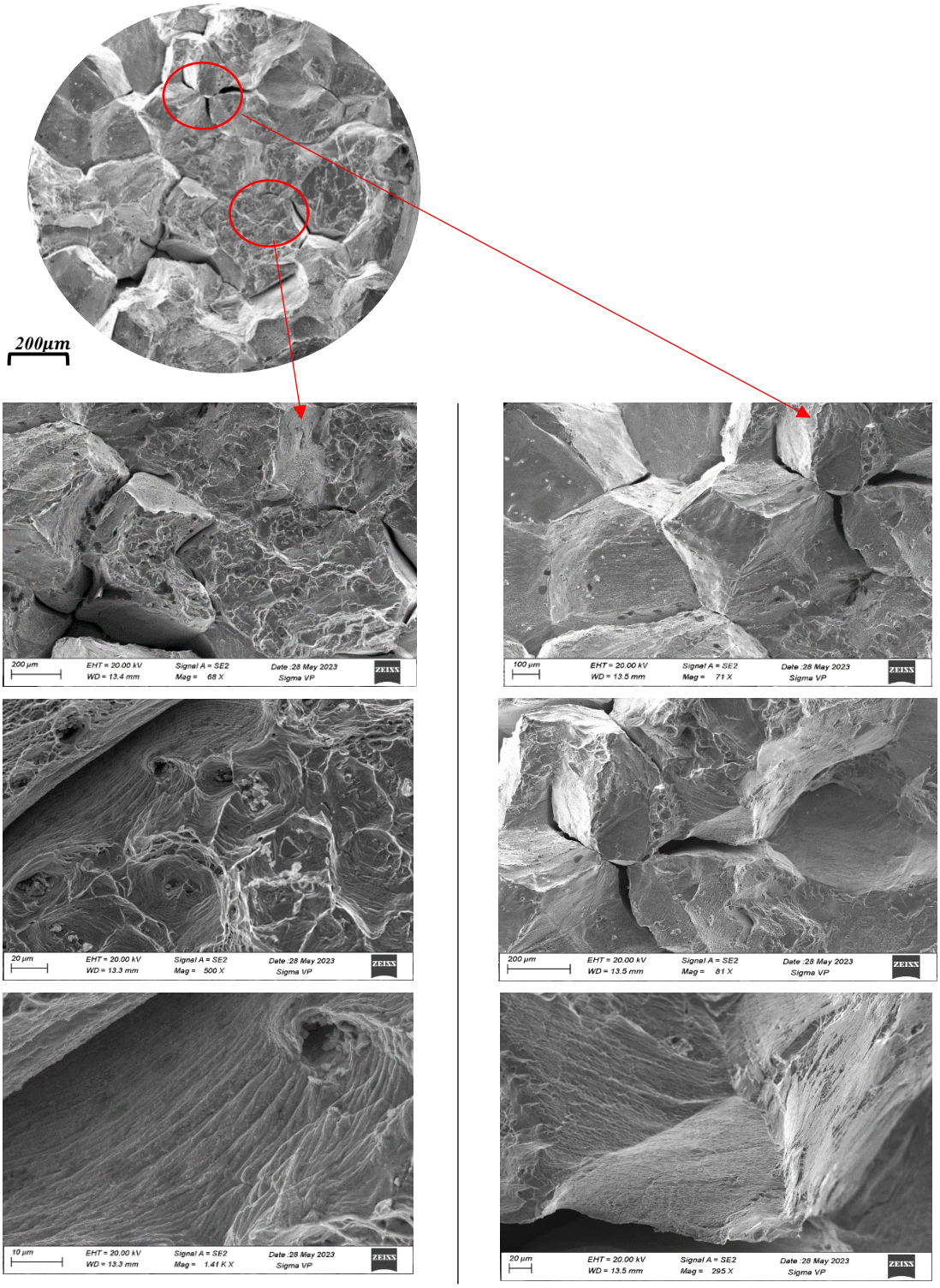

Figure A.2 6 Fractography results at center and edge.

A.2.7 Deformed at 750℃ strain rate 10^{-4}

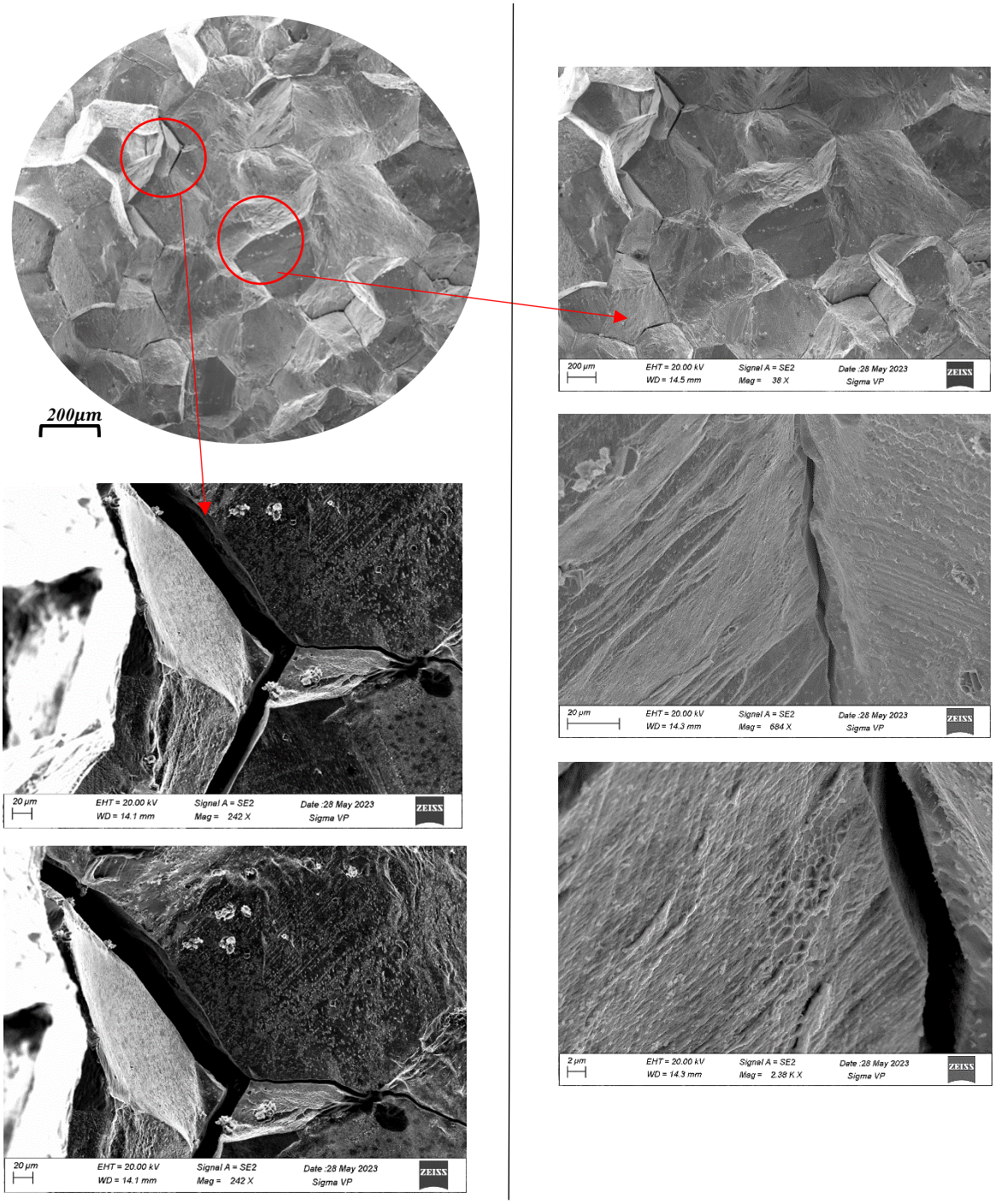

Figure A.2 7 Fractography results at center and edge.

A.3 Fractography No-3

A.3.1 Deformed at Room temperature - 10^{-2}

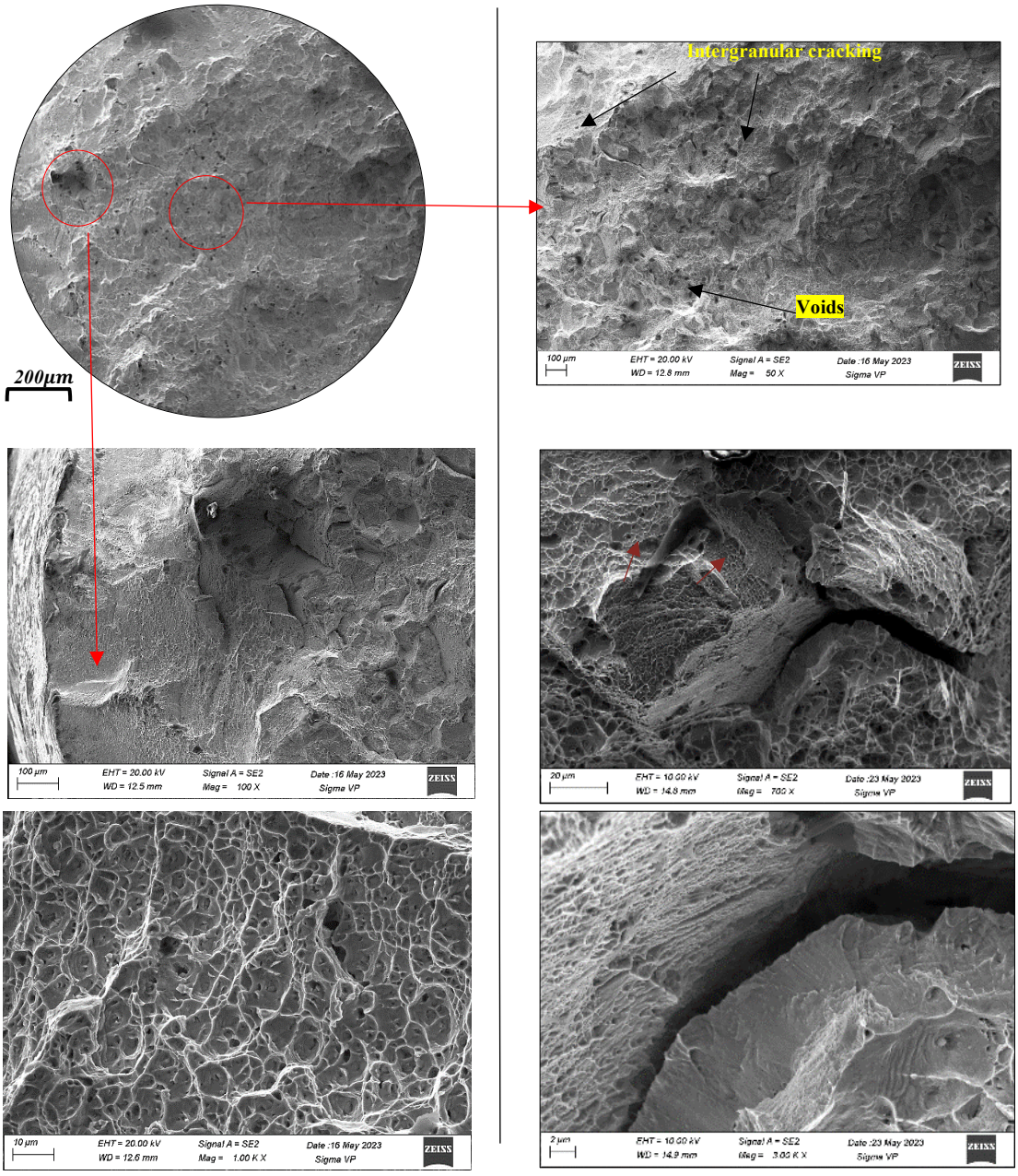

Figure A.3.1 Fractography results at center and edge.

A.3.2 Deformed at 650℃ 10^{-2}

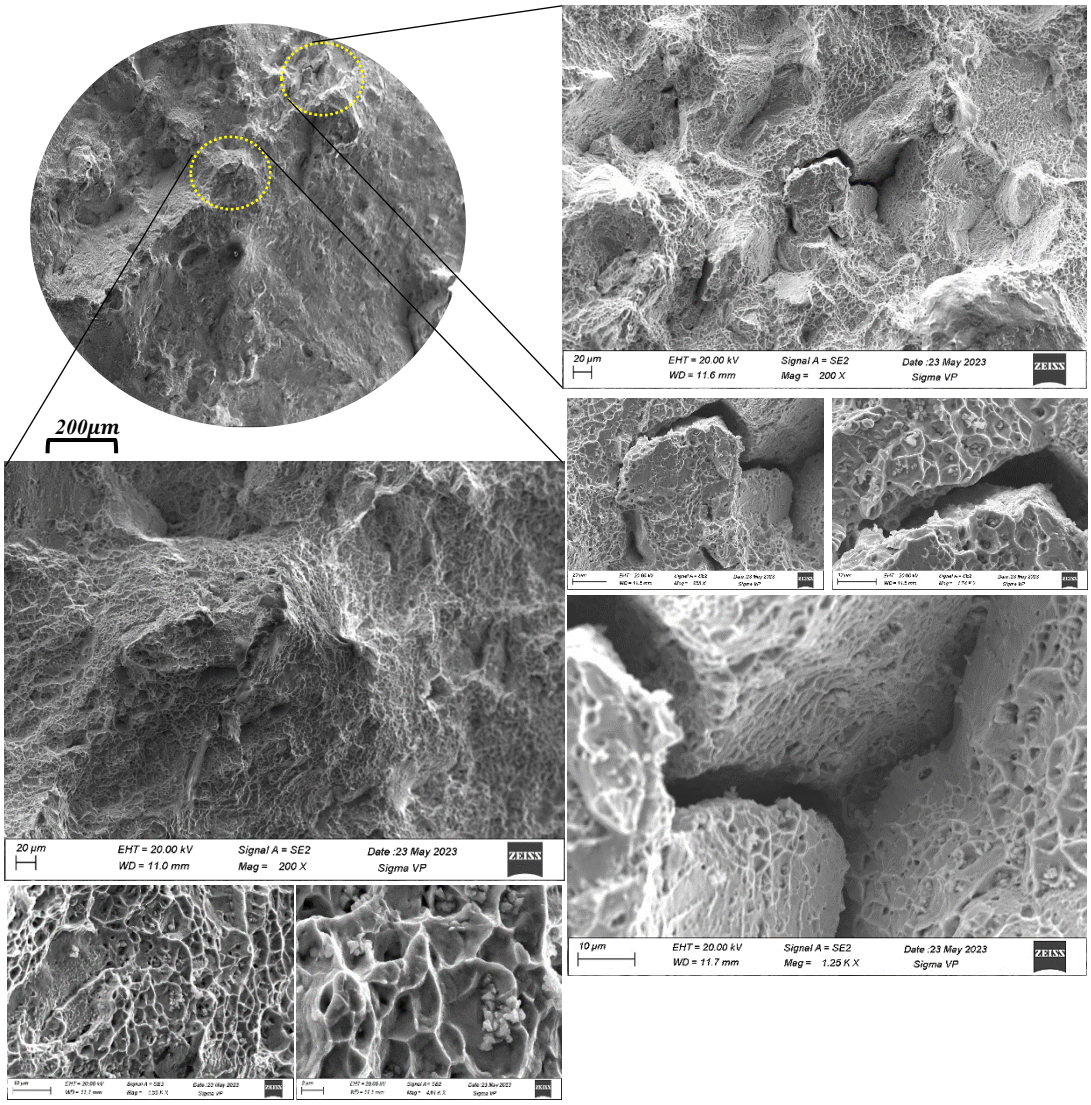

Figure A.3.2 Fractography results at center and edge.

A.3.3 Deformed at 750℃ 10^{-2}

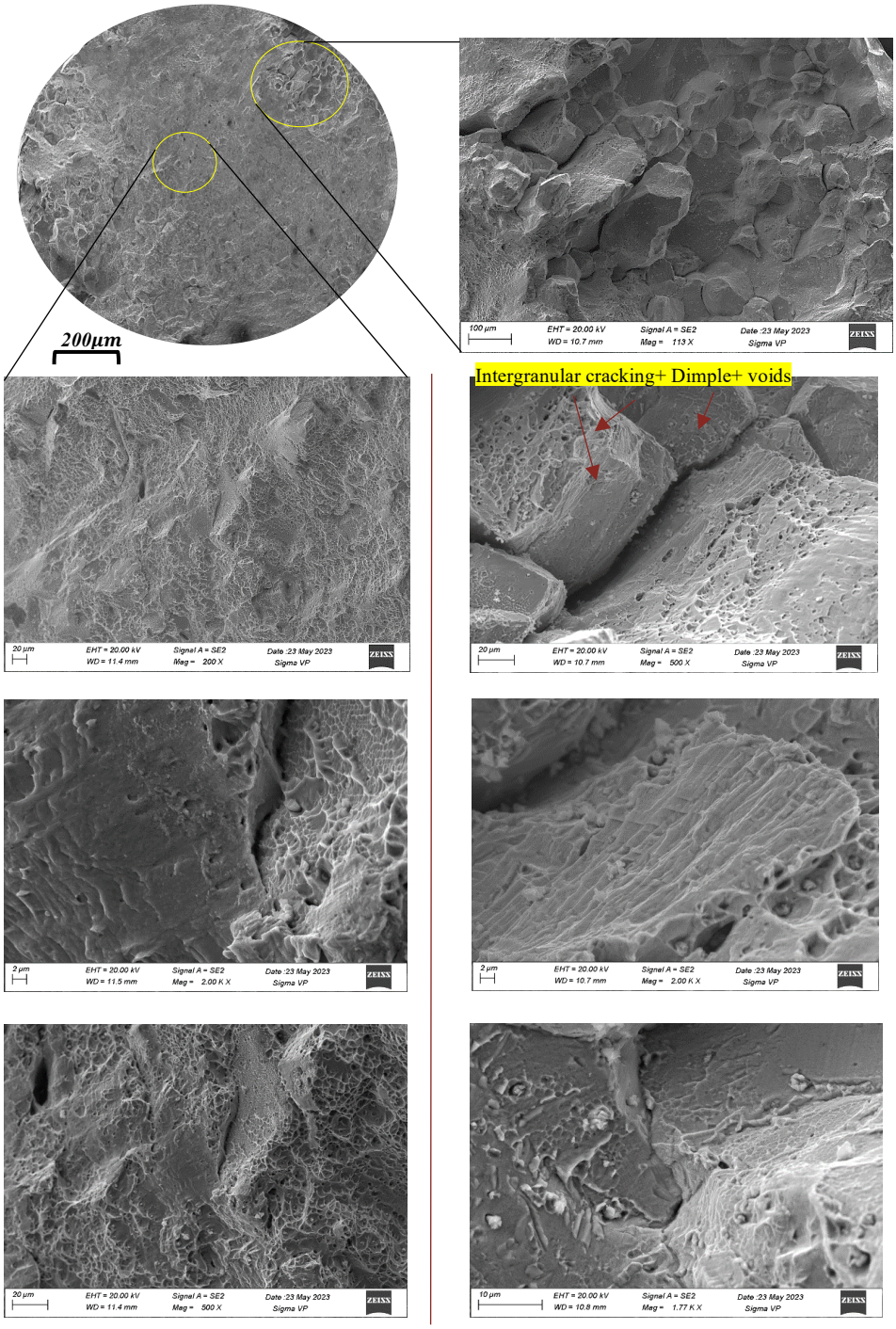

Figure A.3.3 Fractography results at center and edge.

A.3.4 Deformed at 750℃ 10^{-3}

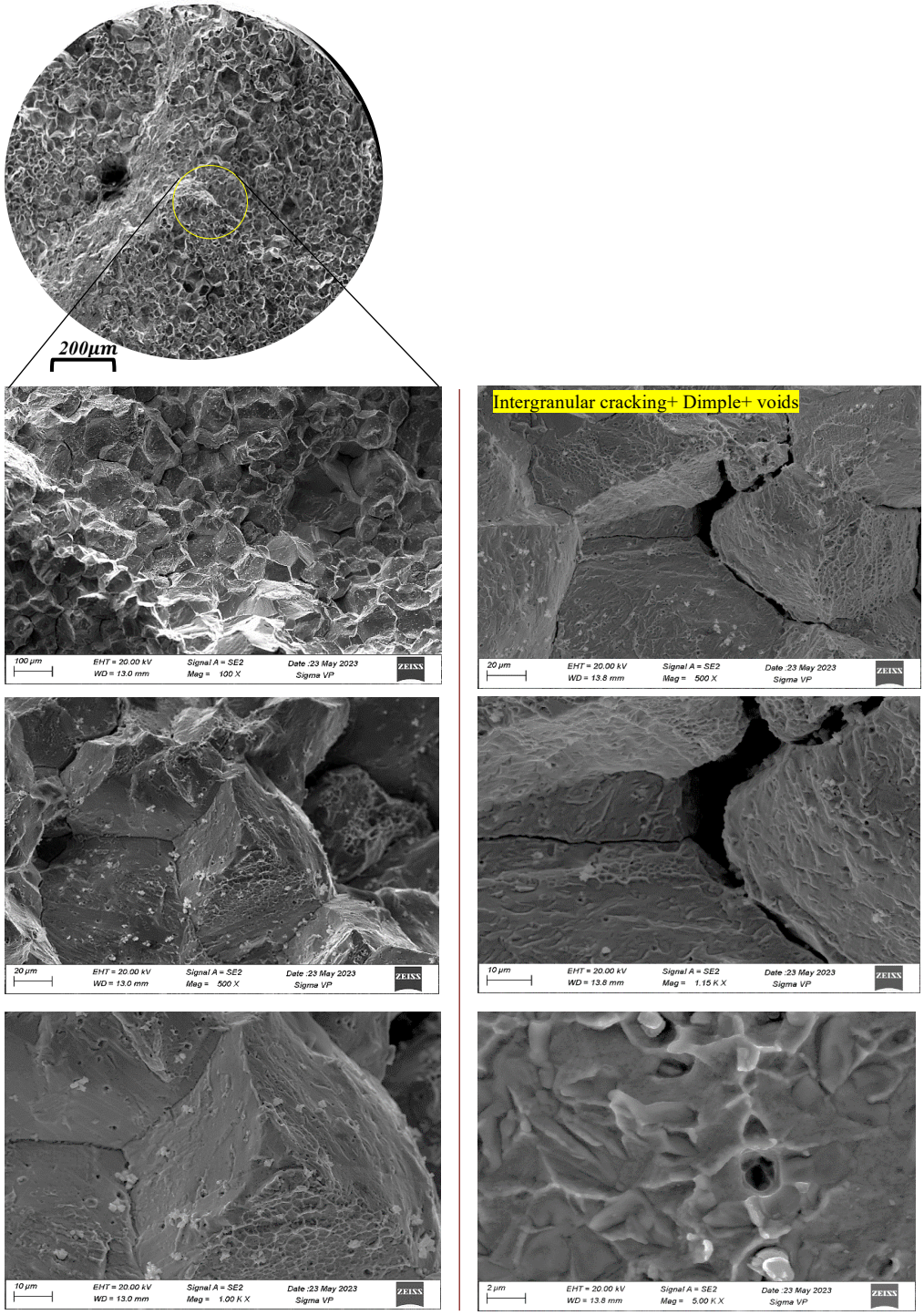

Figure A.3.4 Fractography results at center and edge.

A.3.5 Deformed at 750℃ 10^{-4}

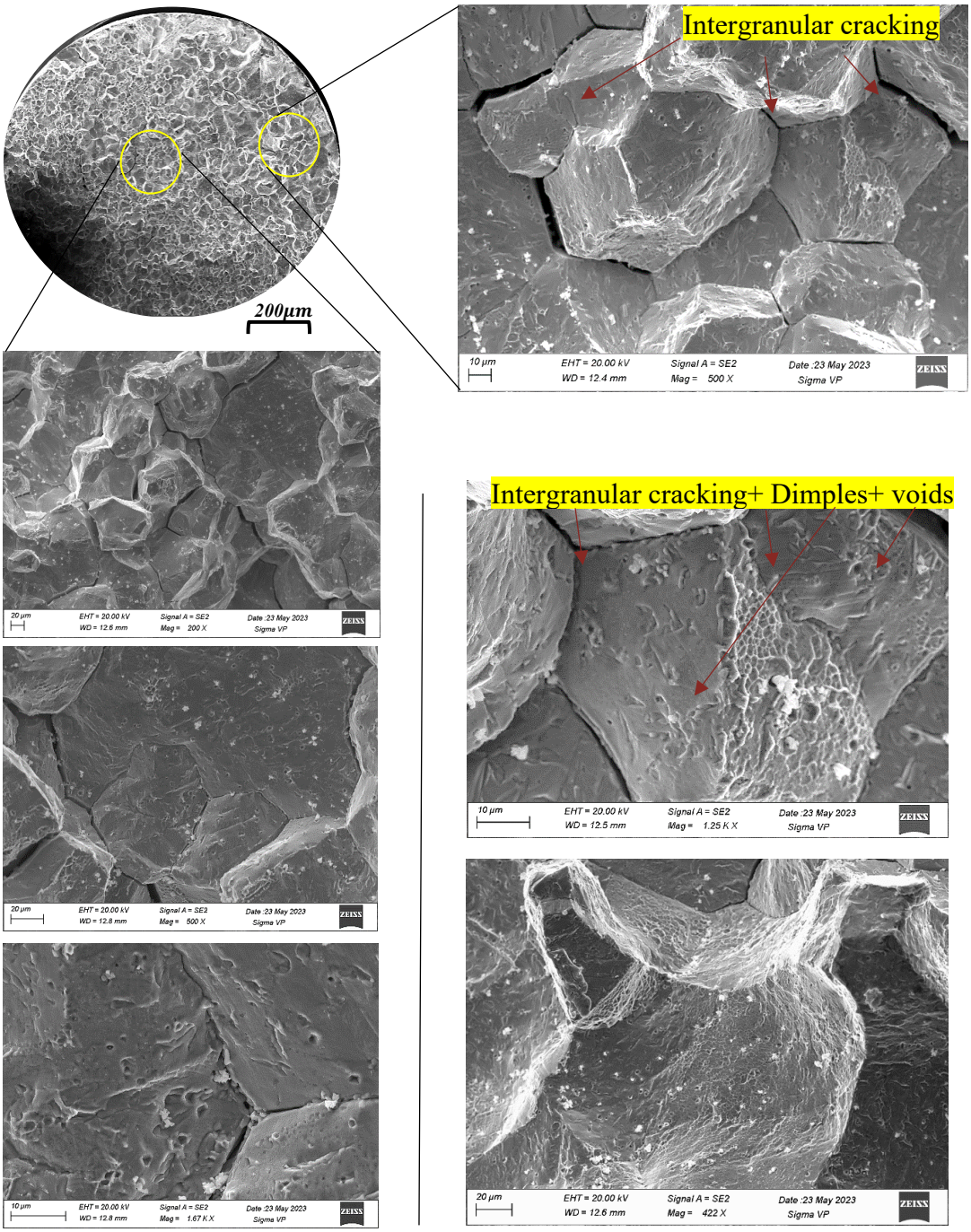

Figure A.3.5 Fractography results at center and edge.

A.4 EBSD BC with LAGB & HAGB No-3

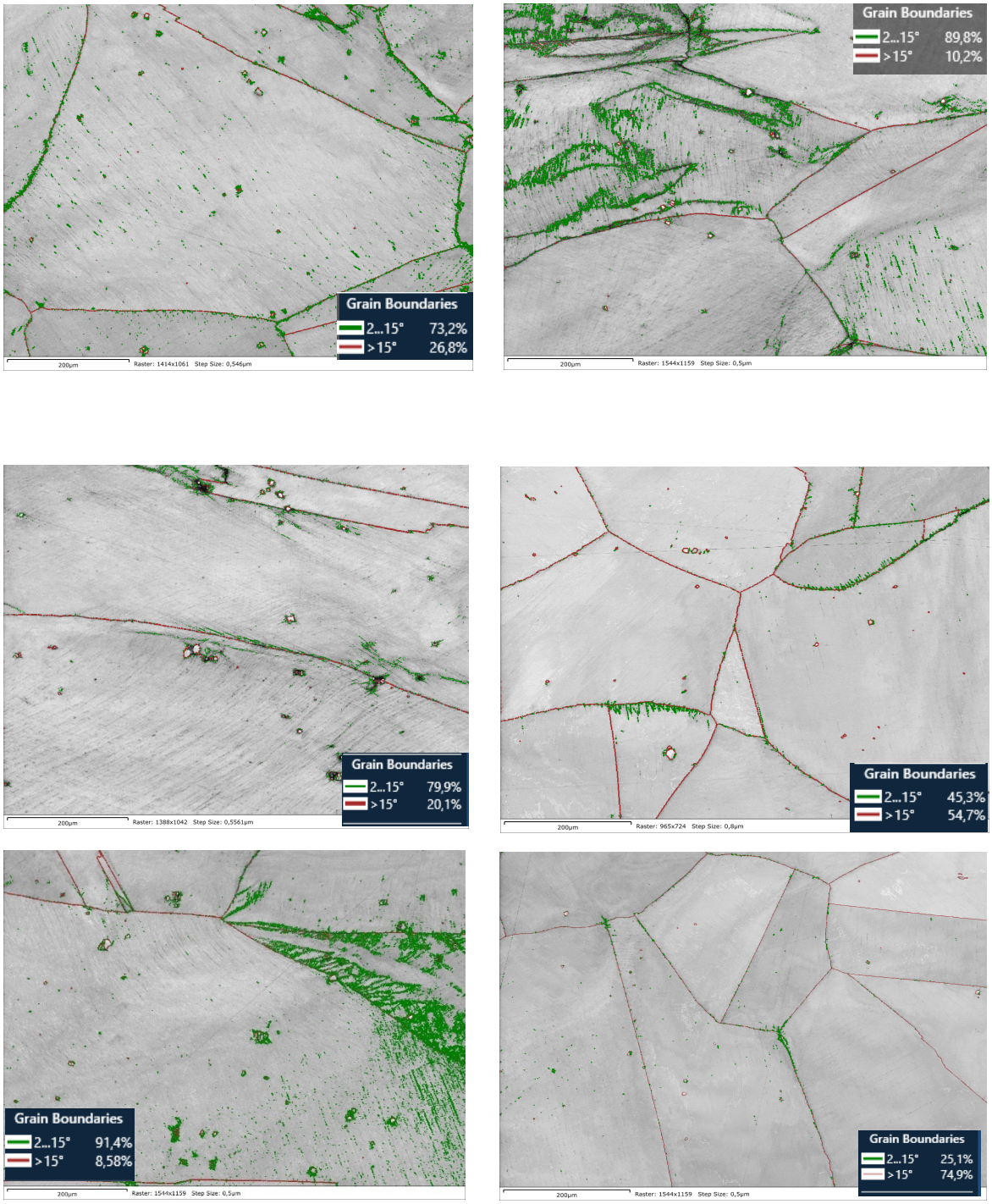

Figure A 4.1 Sample No. 3 deformed at room temperature (a)RT $10^{-1}s^{-1}$, (b) 650°C $10^{-1}s^{-1}$, and (c)750°C$10^{-1}s^{-1}$,(d)750°C 10^{-3} &(e) RT $10^{-4}s^{-1}$ (f)650°C $10^{-4}s^{-1}$,

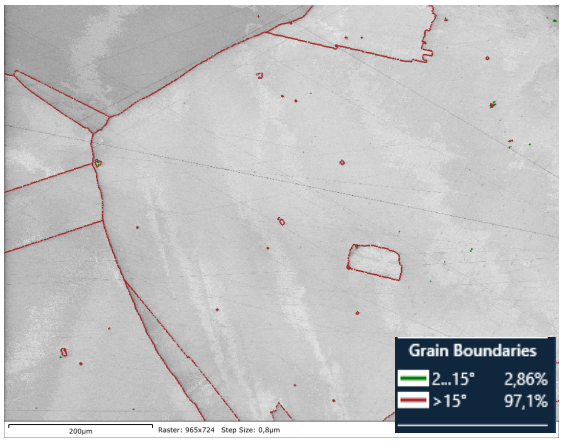

Figure A 4.2 Sample No. 3 deformed at 750°C $10^{-4}s^{-1}$